Faculty of Science and Engineering

Department of Exploration Geophysics

Methods to Analyse and Interpret Shallow Seismic Data: Onshore Central Perth Basin, Western Australia

Jamal O. Esttaifan

This thesis is presented for the Degree of
Doctor of Philosophy
of
Curtin University

April 2015

Declaration

This thesis contains no material which has been accepted for the award of any other degree or diploma in any university.

To the best of my knowledge and belief this thesis contains no material previously published by any other person except where due acknowledgment has been made.

Signature: 

Date: 17 April 2015

I dedicate this thesis

To

My three graces

Mariam, Michael and Talar

Acknowledgements

First and foremost, I would like to thank my supervisor A/Prof Milovan Urosevic for the many hours spent discussing and reviewing research ideas, stimulating my work and helping articulate my results. I also thank him for following up my work and providing constant guidance and encouragement as well as for his patience and support until the very moment of my thesis submission.

A very special thanks and deepest appreciation go to Mr Aleksandar Dzunic who provided me with his numerical modelling codes and programs for the assembly of the CAT scan images. The use of physical models for this study was encouraged by Mr Dzunic and A/Prof Urosevic and I am ever grateful for that. Mr Dzunic also provided significant help in numerical and field seismic data processing.

I thank A/Prof Roman Pevzner for suggesting research directions and supporting my work and also A/Prof Brett Harris for his guidance and supervision in the first years of my studies. He has supported me for a long time and delighted me with ideas, advice and good thoughts.

I would like to express my sincere appreciation to Professor Boris Gurevich, Head of the Department of Exploration Geophysics for his continuous support and the time spent discussing and reviewing ideas as well as for his financial support through the WASM. His advice has been invaluable and his dedication inspirational.

I would also like to thank the committee Chairman A/Prof Maxim Lebedev for his ceaseless encouragement, especially through the hard times during my studies.

As ever, I thank my family for their continuous enthusiasm, support and encouragement and pushing me forward when I stumbled during my years of work.

The support and love of my family has certainly had a great moral impact on me in helping me complete my research. They have my endless thanks and eternal love.

My special gratitude goes to the WASM and the Australian Gospel Church, Victoria Park for their financial support in the contribution of payment the fees of the last 6 months of my work.

My special thanks go to Ms Deirdre Hollingsworth, the secretary of the Department, for her administrative help and to Mr Robert Verstandig for the IT support and for my thesis revision, and also to Mr. Dominic Howman for his efforts during my work in building the physical 3D models and in the Department's workshop.

Abstract

The research presented is aimed to develop a methodology for inferring complex sub-surface shallow structures of a high relevance to hydrological studies of the Gnangara Mound locality, Perth Basin. The motivation for the research was derived from the analysis of 2D high density seismic data acquired by the Department of Exploration Geophysics, Curtin University in 2011. Six high-fold high-resolution 2D seismic lines were acquired to provide new information on the shallow sediments of the Gnangara Mound. The objective was to produce additional information that could be of high relevance to hydrogeological studies in this area.

Initial interpretation suggested the presence of a complex faulted structure that could have an impact on the fluid flow and hence the derivation of a dynamic model for the main aquifer. Proving the interpretation results turned out to be a difficult task. To help resolve interpretation ambiguities high-fidelity 2D and 3D numerical simulations were deployed.The resulting seismic responses were critically analysed as such fault structures have a potentially very significant impact on the fluid flow and the reservoir properties.

With the aid of seismic interpretation, 2D numerical modelling was conducted to simulate the seismic response of the inferred 'flower' structure. The results indicated that in very favourable conditions, such structures could be inferred from 2D seismic data. More realistic 3D simulations were conducted with the aid of physical models and CAT scanning of the models. Simple materials, such as wood and resin were used to rapidly build the model. This approach turned out to be very effective and much faster than conventional numerical model building. The scanned physical model was subsequently populated with the physical parameters acquired from nearby boreholes. Full 3D geometry was used to acquire the numerical data. Full processing, including time and depth prestack imaging, was applied to the synthetic data. The next level of sophistication involved the inclusion of noise that was modelled after the field records. The numerical noise included source-generated energy, ambient noise and attenuation. That paved the way for the analysis of a quite realistic data set, which was

not too dissimilar to the one that would have been recorded in the field. Different levels of noise were introduced to reproduce the best and the least favourable comparisons to field cases. In the best case, it was possible to interpret a ‘flower’ structure from the 3D seismic data. The worst case involved low SNR, and from this it was challenging to positively infer complex structures from the 3D seismic data.

The results of this study show that 2D seismic is less favourable for solving hydrogeological issues. The use of physical models in combination with CAT scanning to digitize the 3D models provides a very rapid means of constructing the 3D numerical models required for numerical simulations The same approach can be used to optimise future 3D seismic acquisition geometries.

Table of Contents

LIST OF FIGURES

LIST OF TABLES

CHAPTER 1

INTRODUCTION

1.1 Introduction

Groundwater resources of the onshore central Perth Basin in Western Australia have been actualised to a depth of 1100–1400 m. Fresh water is present throughout the Jurassic to Quaternary strata and supplies more than 40% of Perth's water requirements. The importance of managing fresh water for local daily use requires a hydrogeological model; hence, studies of the shallow subsurface structures have to be intensified. Reflection seismic investigations were used to gain an improved understanding of the structures and depositional history of the Perth Basin, which spans thousands of square kilometres across Western Australia. Considering the size of the area, seismic interpretation was previously concerned with a regional geological model, rather than investigating shallow structures that are of direct interest to hydrological studies. An additional problem was that the data acquired were of generally low resolution. Recently, high-resolution 2D seismic reflection survey data have been acquired by the Department of Exploration Geophysics, Curtin University. These data produced greatly improved imaging of the shallow geology and provided new insight into the shallow structures of the North Gnangara Mound in the Perth Basin. For the first time, a well constrained detailed analysis uses performance on the shallow sediments, which is important for deriving the hydrogeological model of the Perth Basin.

Previously, most of the seismic investigations in the Perth Basin were aimed at deriving the hydrocarbon potential. Hence, structural and stratigraphic analyses were limited to relatively deep sedimentary formations. Data acquisition and data processing were accordingly set to enhance deep targets, prospective for hydrocarbon exploration. Consequently, previous seismic imaging is lacking shallow details. Therefore, there is an incomplete understanding of the structural play and depositional environments for the shallow formations in the Basin. It is known that large faults oblique to the Darling fault (a mega bounding rift fault structure that runs thousands of kilometres parallel to the coast of WA) are intercepting the continuity of the deep

sediments in the basin. The complexity and hydrological transmissivity of these formations is presently unclear.

Geological formations, like the Leederville and Yarragadee, have massive areal extent and are highly significant for water supply. The hydrogeological model currently under development is, in general, highly sensitive to the structural features, their geometry, areal extent, fault tips termination points, fault properties (sealing or transmissive), and so on. Even the direction of sediment influx is not very well defined. All the elements above need to be investigated across the Basin in order to arrive at a viable model needed for dynamic hydrological studies.

In 2011, six 2D high-resolution seismic lines were collected on the Gnangara Mound (Harris, 2011). The acquired data were processed at Curtin University. Seismic line-3 was of specific interest to this study as it showed an uncommon pattern. After thorough data analysis I strongly suspected the presence of a near-surface complex structure. Further studies were required; as such structures may have a profound effect on the fluid dynamics in the Mound. Structures of this type were not visible in the old, low-resolution seismic data. Despite the fact that the old seismic works amounted to 27,300 line kilometres (Owad-Janes and Ellis, 2000), new seismic data were required to analyse shallow features in the Perth Basin. Old works also included some 200 boreholes, but again, logging and analysis focused on deeper formations and structures, and correlation with deeper seismic events that were of interest to hydrocarbon studies. Examples of such work are found in Lasky and Lockwood (2004) who focused on deeper seismic events that were based on completion of the work done by the Western Australian Bureau of Mineral resources (Owad-Janes and Ellis, 2000).

After revisiting the old works it was clear that new, high-resolution seismic works were required to facilitate derivation of more precise hydrogeological models of the Perth Basin (Urosevic et al., 2007). Indeed Martin et al. (2013) first carried out detailed seismic investigations aimed at analysing near-surface structures. They demonstrated that seismic reflection data can help define aquifers. This was the foundation work where on which I built my research.

1.2 Issues

The groundwater industry has been slow in adopting seismic reflection methods for helping resolve hydrogeological issues. One of the reasons is the generally high cost of seismic surveys due long time frame to acquire, interpret and process data. Another is that the existing seismic reflection survey data was of little use to hydrologists. This is to be expected as the acquisition parameters were adjusted for deep regional investigations. It came as no surprise that especially early seismic surveys in the period 1960–1989 were in general, of very poor quality, particularly in the northern Perth Basin (McKellar, 1971; Tarabbia, 1991; and Titan Energy Ltd., 2012). The Perth Basin could be considered as unexplored with respect to information available for the analysis of the first 1000 m of the subsurface.

The Gnangara Mound is considered to be the largest water resource in Western Australia and covers an area of approximately 2200 square kilometres. The knowledge of the aquifer mainly derives from isolated drill holes and logs. Such "point" information requires extrapolation of the stratigraphic units over many kilometres, inevitably yielding derivation of an oversimplified hydrogeological model. To study such large area and reduce the uncertainty, it is necessary to introduce reflection seismic into the study. Even with seismic, investigation of such large and (as we will later see) geologically complex area is a long term project that requires close cooperation between hydrologists, geologists and geophysicists.

The high-resolution seismic program of the Gnangara Mound started in 2011 as a joint effort between the Water Corporation and the Department of Water, Western Australia. The primary aim was to image the near-surface structures as well as aquifer geometry and extent (Martin et al., 2011). It was also important to map the boundaries between major aquifers, such as Yarragadee and Leederville. Soon after the first seismic results were produced, it became clear that near-surface fault structures appeared to be more complex than initially envisaged and that further thorough investigation were required.

1.2.1 Research objectives

High-resolution 2D seismic data offered new insights into the complexity of the near surface fault structures at the Gnangara Mound. However, there are inherent limits associated with 2D seismic that originate from directional illumination of the geology. In other words, if the seismic line is not ideally positioned in the true dip direction, then the resultant images may be misleading and interpretation prone to errors.

Analysis of the 2D seismic images, particularly seismic line-3, suggested that potentially complex fault structures, such as 'flower' or 'inverse flower structures' may exist. It was difficult to produce firm conclusions using only 2D seismic data, particularly in the absence of additional calibration points such as provided by cores and borehole wireline logs. It was therefore necessary to come up with a new approach plan and research direction that could potentially answer the question of the existence of complex near-surface structures. While the general objective was to perform detailed structural analysis of seismic data for defining an improved hydrogeological model, the more specific task was to devise a method for objectively extracting information from existing seismic data. This could help current exploration and possibly suggest new directions in the future that could lead to an improved definition of the near-surface geology and hence an improved hydrogeological model.

1.2.2 Methodology

With only 2D seismic data available for this research, there is a high potential for exercising a subjective interpretation and therefore producing conclusions prone to errors. It is necessary to introduce additional analyses that support or deny the initial seismic-only based interpretation. In the absence of ground "truth", that is boreholes, the only available resource is modelling the seismic response and comparing it to the field results. 2D synthetic modelling is a natural approach considering that field data are also 2D. However, considering that the proposed structures are inherently 3D in nature, it is necessary to transfer the problem into 3D. Oversimplification is still likely, and additional steps need to be taken to bring numeral data closer to the field data.

Constructing a 3D numerical model is a non-trivial task, and in this thesis it is investigated alternatives to this approach. Overall, the set of successive 2D and 3D "noisy" simulations are a primary tool for firming up 2D seismic interpretation and establishing the most likely geological scenario at the Gnangara Mound.

1.3 Thesis layout

This thesis is composed of seven chapters.

Chapter 1 provides the reader with the basic reasons that motivated this research. A brief background history of the exploration in the area under investigation is also presented. The objectives of the research and the methodology used are discussed.

Chapter 2 elaborates on water supplies in Western Australia as well as a global hydrological model of the Perth Basin. I also provide information on the current thinking of the Basin's evolution, dominant structures and depositional environment. The historical role of seismic data in the studied area is discussed. Essential information of the study area, the northern Gnangara Mound, is also provided.

In Chapter 3 I Present and discuss the 2D seismic interpretation of the high-resolution seismic lines acquired by the Curtin Department of Exploration Geophysics in 2011 in the northern Gnangara Mound. Geological and structural interpretation is presented.

Chapter 4 describes the methodology utilised in this research. The initial step deploys 2D modelling of the complex faults. The results are compared to actual field data. Analyses of the results pave the way for further investigations.

Chapter 5 introduces a novel way of creating 3D numerical models. The 'flower' structure is constructed using basic materials. Details for building the physical 3D model, including the CT model scanning, are provided. 3D numerical modelling, modelling and image analysis are presented.

Chapter 6 demonstrates a methodology used to bring numerical simulations closer to field data results. The introduction of realistic noise content is derived from

the analysis of actual field data. Final “noisy” images are then fully processed and analysed. Relevance to the initial objectives are analysed.

Chapter 7 summarises the methodology and the results. It also proposes a way forward that may advance the analysis of the shallow structures of direct relevance to hydrological studies in the Perth Basin.

Chapter 2: Exploration of water resources in Perth Basin

2.1 Introduction

Water is a valuable resource. Apart from drinking and household use, Australians rely on water as an input to almost every industry in the nation's economy, particularly agriculture. Western Australia is the second driest state in the world's driest continent (after Antarctica) and fresh water is one of Australia's most important natural resources.

The drinking water in Perth comes from both surface and groundwater sources. The volume of water available is determined mainly by rainfall, which affects run-off recharge and groundwater supplies. Rainfall is variable and in recent times many parts of Australia have experienced long periods of drought. One of the factors that affect the water supplies is population growth.

As a result of climate change, freshwater supply is highly subjected to droughts. Therefore attention is highly focused on the need to conserve water. Water storage in dams and underground aquifers are the important tools to secure water supplies for human use in Western Australia.

During the 1970s and 1980s, the IWSS (Integrated Water Supply Scheme) used groundwater to supplement the supply of surface water for the expansion of the northern suburbs. Nowadays, the IWSS gets more than 60% of its water from groundwater sources and pumps it to the Northern Perth suburbs (CSIRO, 2005).

2.2 Water supply

The water supply in Perth, Western Australia comes from accumulation lakes and Aquifers (Shan, 1995; Simpson, 1998) The Gnangara Mound and the underlying Perth Basin aquifers are the largest source of groundwater for south-western Australia; it covers an area of about 2200 km^2 and supplies Perth with 35–50% of its drinking water (Meredith et al., 2012).

Perth groundwater resources are obtained from three major aquifers that occur beneath the Perth metropolitan area: the Superficial Aquifer, Leederville Aquifer and Yarragadee Aquifer. The Superficial Aquifer is unconfined and composed of Quaternary-Tertiary sediments of the Swan Coastal Plain. The aquifer consists of sand, silt

and clay, usually 30 m deep, but reaching up to 70 m. The Leederville Aquifer is spatially confined, and consists of interbedded lenses of sandstone, siltstone and shale. It is directly below the superficial aquifer where the Osborne Formation is eroded. The Yarragadee Aquifer consists of interbedded sandstones, siltstones and shale beds. It is up to 2000 m thick (Salma et al., 2000). The boreholes shown in Figure 2.2.1, in the Gnangara Mound have reached only the upper part of the aquifer, that is, approximately 500 m (Thorpe and Davidson, 1991).

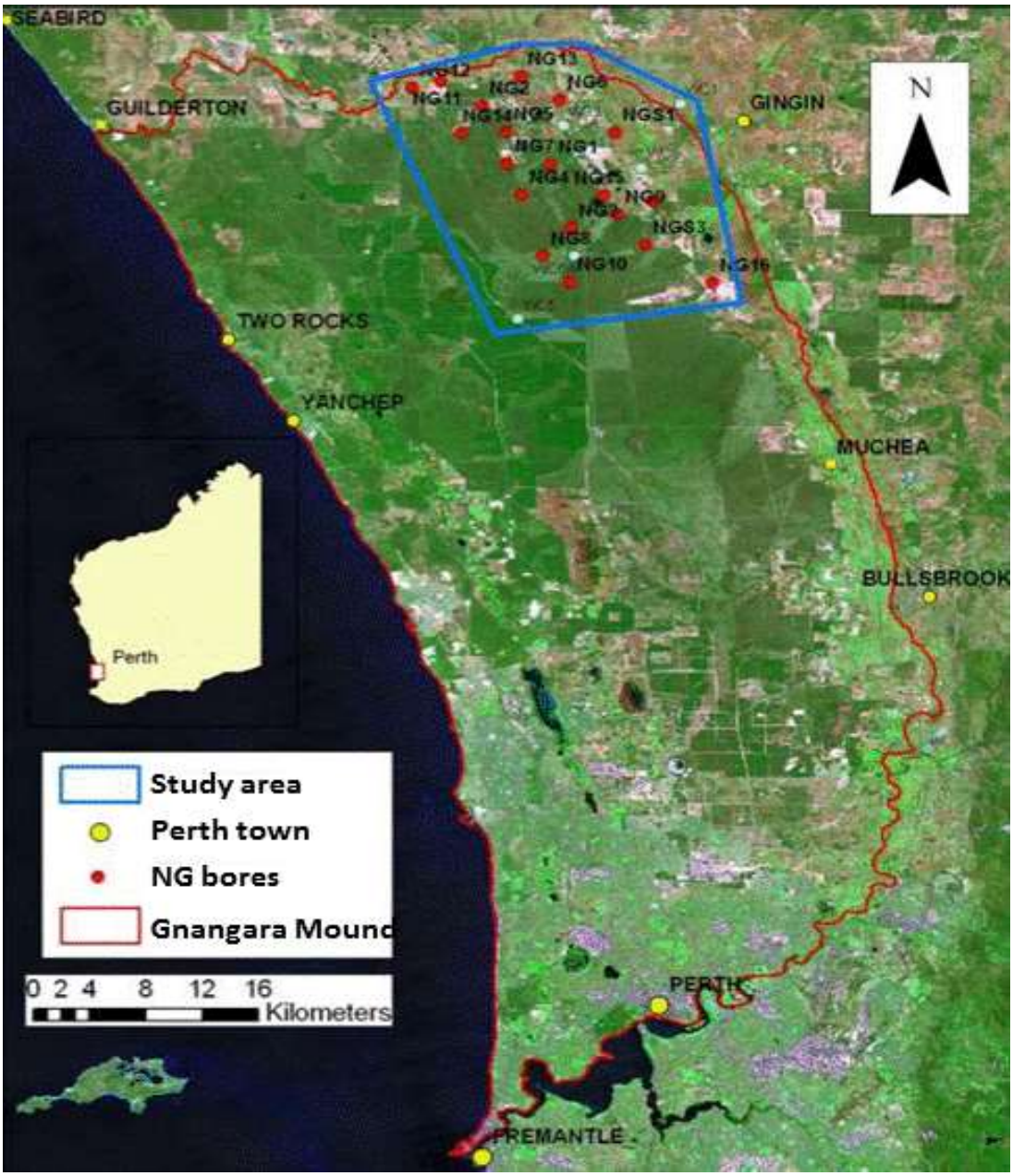

Figure 2.2.1: The north Gnangara Mound 70 km north of Perth, 20 km west of Gingin. Boreholes shown in red (from Pigois et al., 2010)

The Yarragadee aquifer is the major confined, fresh water resource aquifer underlying the Perth Region and extending to the north and south within the Perth Basin. It is a multilayered aquifer; it varies in thickness from around 100 m to 3000 m (Crostella and Backhouse, 2000). The Yarragadee aquifer consists of the Jurassic Yarragadee Formation, but also includes the Cretaceous Gage Formation, the Parmelia Formation in the north east, and the Cattamarra Coal Measures in the south east (Davidson, 1995) (Figure 2.2.2). The formation was eroded and uncomfortably overlain through much of the Perth region by the Leederville Formation, South Perth Shale and Gage Formation, resulting in the Neocomian Unconformity, which is generally taken as the upper surface of the Yarragadee Aquifer.

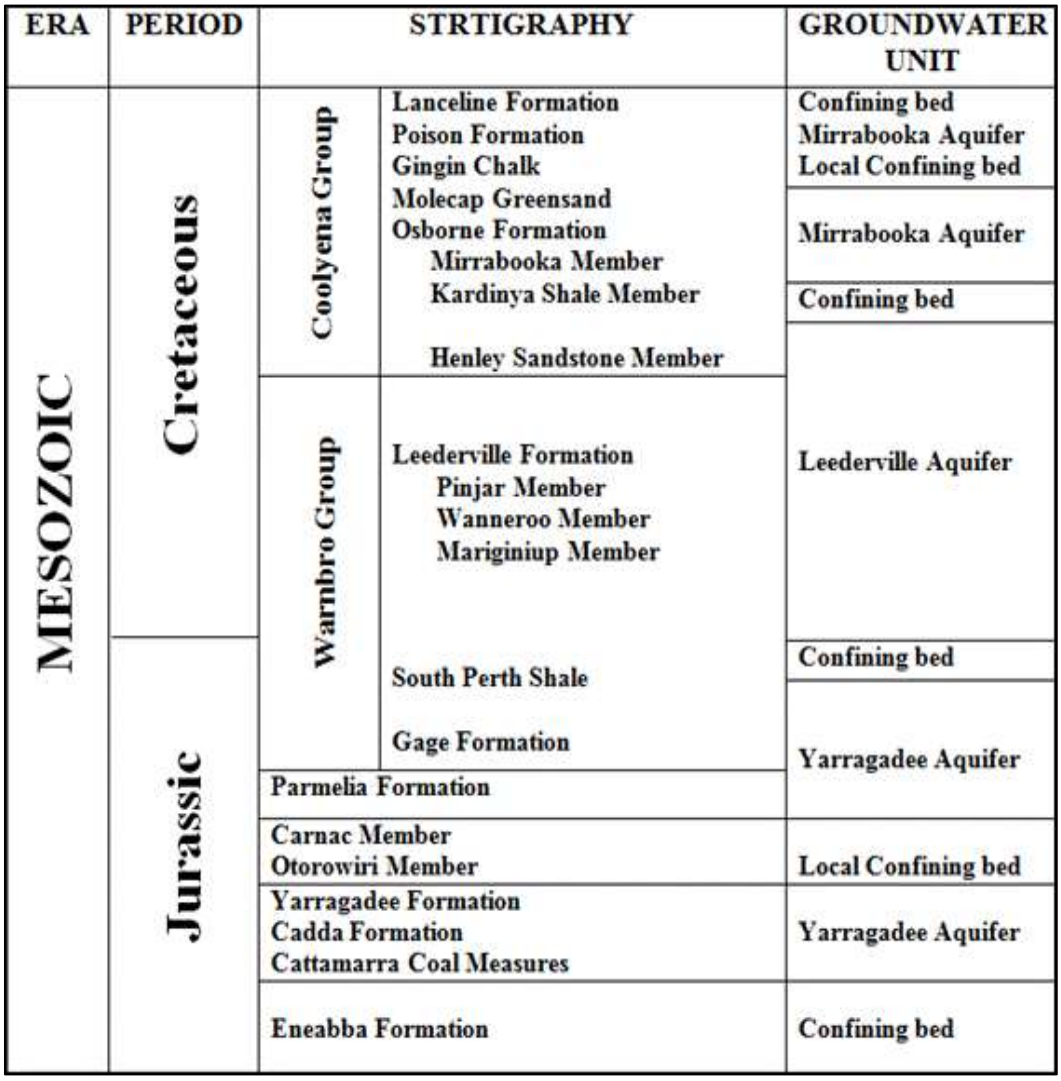

Figure 2.2.2: Stratigraphic sequence of the Perth Basin (Mesozoic Era), with the corresponding groundwater units (from Davidson, 1995).

2.3 Global hydrological model of Perth Basin

A groundwater mound refers to mounding of the water table within a superficial system. It is called a mound because the water table forms a mound shape from local recharge. The mound develops where the rainwater that infiltrates it vertically is greater than the rate at which ground water flows horizontally.

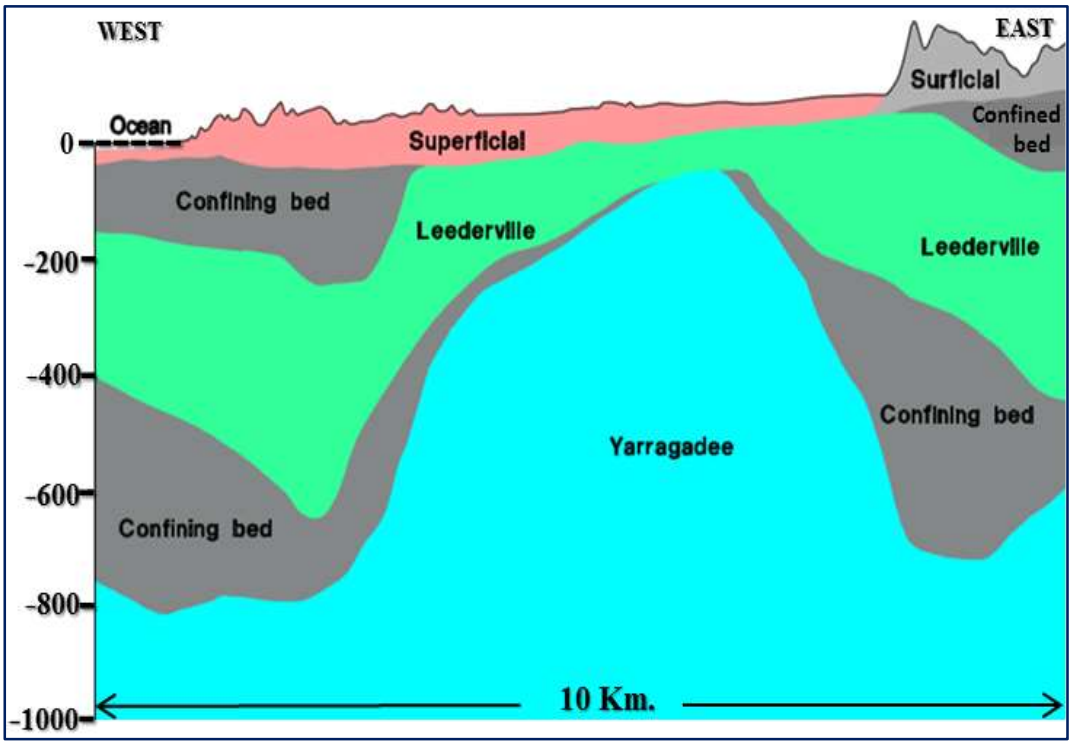

Figure 2.3.1: A simple sketch of the distribution of the three Aquifers in the Gnangara Mound (Xu, 2008).

The ground water resources in Western Australia are comprised of three main aquifers (Figures 2.3.1 and 2.3.2). The Superficial Aquifer is shallow and unconfined. It receives direct recharge from rainfall. The top of the saturated zone in an unconfined aquifer is the water table. The rainfall recharge infiltrates the Superficial Aquifer and vertically migrates to the confined aquifers through areas where no confining layer exists in between the Superficial and underlying Aquifers.

The Yarragadee Aquifer receives most of its recharge from the Leederville Aquifer to the north of Perth, where confining shale beds are absent (Glasson et al., 2011; Karina, 2011; Katsavounidis, 2006).

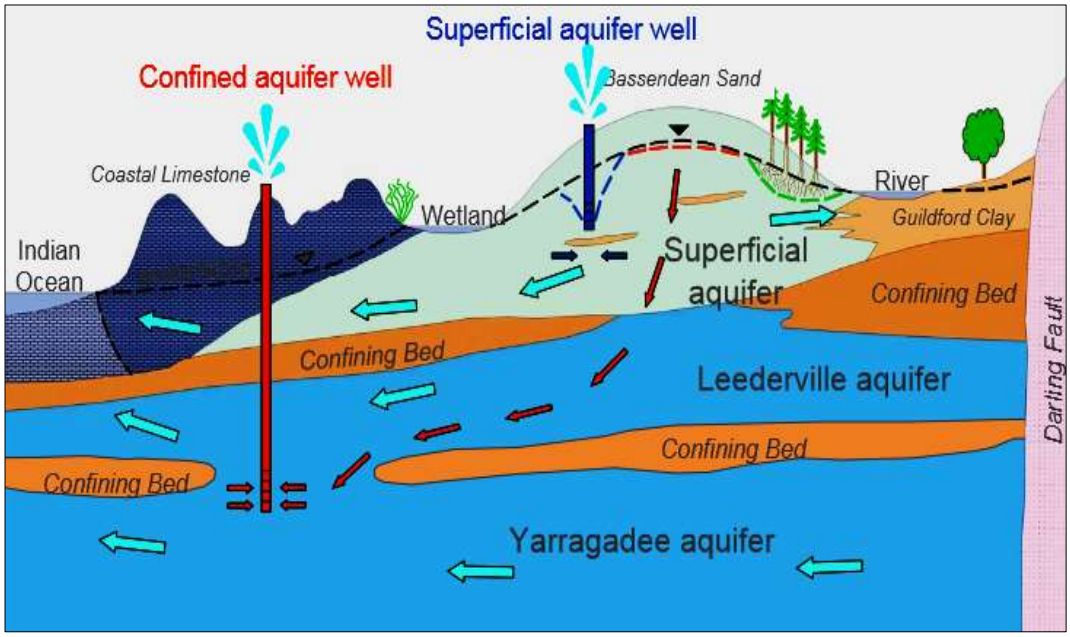

Figure 2.3.2: The three aquifers in the Gnangara Mound (Sinclair, 2011).

The two confined Leederville and Yarragadee Aquifers are deeper under the ground and mostly overlayed by material (i.e. clay). The Superficial Aquifer is hosted by the Quaternary and Pliocene sediments. The Leederville Aquifer is hosted by the Lower Cretaceous Leederville Formation, while the Yarragadee Aquifer (Davidson 2006) is hosted by the upper Jurassic Yarragadee Formation and locally by the lower Cretaceous Gage Formation (Leyland, 2011) (Figures 2.2.2 and 2.4.1).

The focus of this research is the Yarragadee Aquifer (upper Jurassic) Davidson, 2006, which is the main aquifer in the North Gnangara Mound and supplies Perth with about 45% of its water requirements (Heath, 2013). Its thickness in the north Gnangara Mound varies from 150–2000 m. The Yarragadee Aquifer receives its recharge through downward leakage from the Leederville or Superficial aquifers, where confining beds are absent and where there is a downward hydraulic gradient.

The Yarragadee Aquifer is confined by the overlying South Perth Shale, the Otorowiri, which is a member of the Parmelia Formation (north), or the shale beds of the lower part of the Leederville formation (Figure 2.2.2).

2.3.1 Aquifers recharge and discharge

The Superficial Aquifer is recharged directly from rainfall with minor upward recharge from the underlying Leederville and Yarragadee Aquifers in some areas. Groundwater discharge occurs by evaporation from wetlands, transpiration from groundwater dependent vegetation, leakage into underlying aquifers and by groundwater abstraction from wells. Groundwater is recharged to the Leederville Aquifer through the Superficial Aquifer on the crest of the Gnangara Mound, and flows westward to eventually discharge offshore. Some groundwater in the Leederville Aquifer discharges into the Superficial Aquifer where the Kardinya Shale Member is absent and where there are increasing heads with depth and upward hydraulic gradients (DOW, 2009).

The Yarragadee North Aquifer is recharged on the northern Gnangara Mound by downward leakage of groundwater where it is directly overlain by the Superficial Aquifer. It is also recharged from the Leederville Aquifer where the South Perth Shale is absent, and where a downward hydraulic head prevails. Groundwater discharges from the Yarragadee aquifer into the Leederville Aquifer in area where there are upward hydraulic head differentials and where the confining South Perth Shale is absent. Aquifer consists of interbedded sandstone, siltstone and shale. The South Perth Shale or shale beds within the Parmelia Formation confine the Aquifer above. It is in hydraulic connection with the Leederville Aquifer where the South Perth Shale or Parmelia Formation is absent (Salama, R.B., 2002). A schematic groundwater recharge mechanism is shown in Figure 2.3.3.

Water drawn for public water supply comes from all of the aquifers and is distributed between them, with more coming from the deeper aquifers and less from the superficial aquifer, to minimise the impact on groundwater dependent ecosystem (DOW, 2009). The production rate and long term modelling of water supply requires a high quality geological model. Hence knowledge of the structural features are of a key importance as it has significant impact onto the acquirer continuity, intra-aquifer connectivity and recharge mechanism. Consequently the prime objective of this work was to utilise seismic data for the structural analysis of main aquifers in Gnangara area

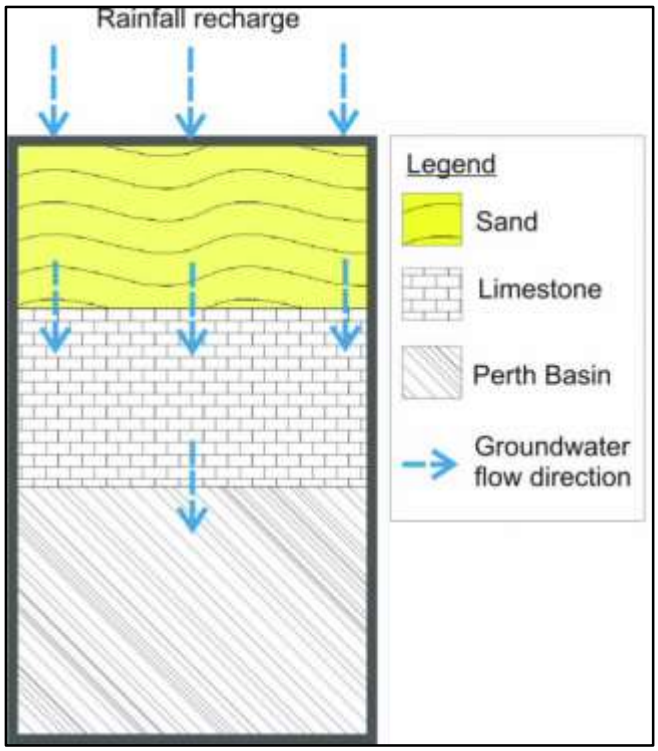

Figure 2.3.3 The pathway of groundwater recharge into Perth Basin Aquifers (from Meredith, 2012)

2.4 Geology of the Perth Basin

The Perth Basin is an elongated north–south trending sedimentary basin, which extends along the south-western margin of the Australian continent. It is a complex basin that was formed during the separation of Australia and Greater India in the Permian to Early Cretaceous (Owad, 2000). Playford et al. (1976), described the Perth Basin as an elongate, north to northwest-trending sedimentary basin that spans across approximately 1,300 km. It averages about 65 km in width and is filled with sedimentary rocks along the south-western coast of Australia, both onshore and offshore (Offshore Petroleum Exploration Acreage Release, 2013 and Empire Oil & Gas NL, 2015).

Janssen et al., (2003) described the Perth Basin as a faulted trough filled with sediments, while the main structural feature is the Darling Fault. Perth Basin is pervaded by numerous faults, with most faults having north to northwest trends while

throwing both to the east and west. There are however a number of “echelon” type of faults of small to medium size throughs, trending approximately east–west.

The technical term “sedimentary basin" means a depression in the earth's crust where sediments accumulate. It is like a huge natural wash basin—full of sand, pebbles, clay, mud, dust, old seashells and anything else that may have fallen in, been blown in by wind or washed in by flowing water. The Perth Basin contains mainly continental clastic rocks, ranging in age from Permian to Recent, and deposited in a developing rift system that culminated with the breakup of Gondwana in the Early Neocomian (Lasky et al., 1991).

The discovery of the onshore Perth Basin was through groundwater and petroleum exploration (Davidson, 1960 and 1995; Allen, 1976; Crostella, 1995; Crostella and Backhouse, 2000; Lambeck, 1987; Moray, 2005). McPherson’s study (2005) shows the stratigraphic column of the Perth Basin sediments (Figure 2.4.1) that is relied on in Davidson’s (1995) studies in expansion to the studies made by Cockbain (1990) and Playford et al. (1976). It focuses on the Late Tertiary and Quaternary units, which are outlined by Playford et al. (1976), when describing the geology of the Perth Basin as most of the regolith is within these successive units of the Basin.

In their study of the Perth Basin, Cadman et al., (1994) evaluated the sedimentation in the basin as it started in the late Ordovician to Silurian to Quaternary when in the extreme north of the basin, adjacent to uplift Precambrian basement, a structural low with the fluviatile Sandstone was laid down. No sediments of Devonian or Carboniferous age have been found in Perth Basin. Although the Permian to Cretaceous stratigraphic and structural evolution of the southern Perth Basin is similar to that of the northern Perth Basin (Crostella and Backhouse, 2000), marine intervals that break the continuity of the prevailing coarse-grained terrigenous deposits in the northern region are not present in the south, where the environment of deposition was entirely continental up until the late Neocomian. Most of the Phanerozoic sediments deposited in shallow water, fluvial or continental environments are believed to have originated from the Yilgarn Block (Playford et al., 1976). Exploration in the central Perth Basin has focused on the offshore Vlaming Sub-basin. In particular, it has concentrated on

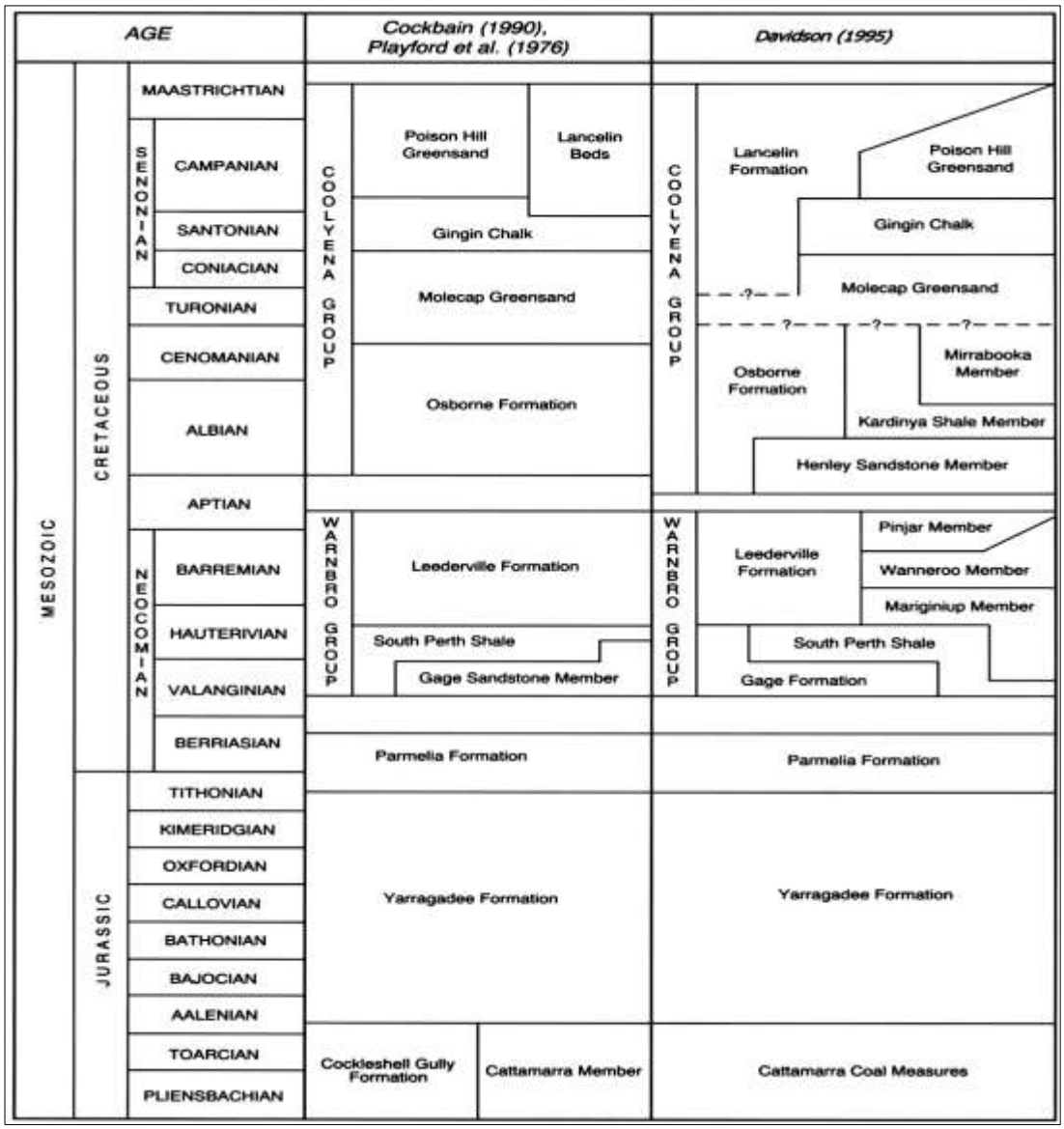

Figure 2.4.1: Stratigraphic column of the Perth Basin (from McPherson, 2006).

the Parmelia Group, which is over 3000 m thick, and on the overlying Gage Sandstone.

Wilde, 1987 studied the Phanerozoic sediments in Perth Basin in reliance to Playford et al. 1976 had estimated maximum thickness of the main stratigraphic units (Table 2.4.1), where numbers in the sedimentation column refer to duration (in Ma) these intervals.

Period	Sediment Thick-ness (m)	Sedimentation (m Ma^{-1})
(Ordovician) Silurian (40)	3000	–
Devonian (50)	–	–
Carboniferous (65)	–	–
Permian (50)	2600	50
Triassic (35)	2500	70
Jurassic (55)	4200	75
Cretaceous (75)	6000	80
Tertiary	Very little	–

Table 2.4.1 indicates the minimum estimation of the maximum thickness of Phanerozoic sediments in the Perth Basin (Playford et al. 1976)

Crostella and Backhouse (2000) carried out a geological correlation between available deep wells across the Perth Basin. A cross section from "Woodada 3" (north of Perth) to "Sue1" (south of Perth) shows the distribution of the formations along Perth Basin with their thicknesses and extensions. (Figure 2.4.2)

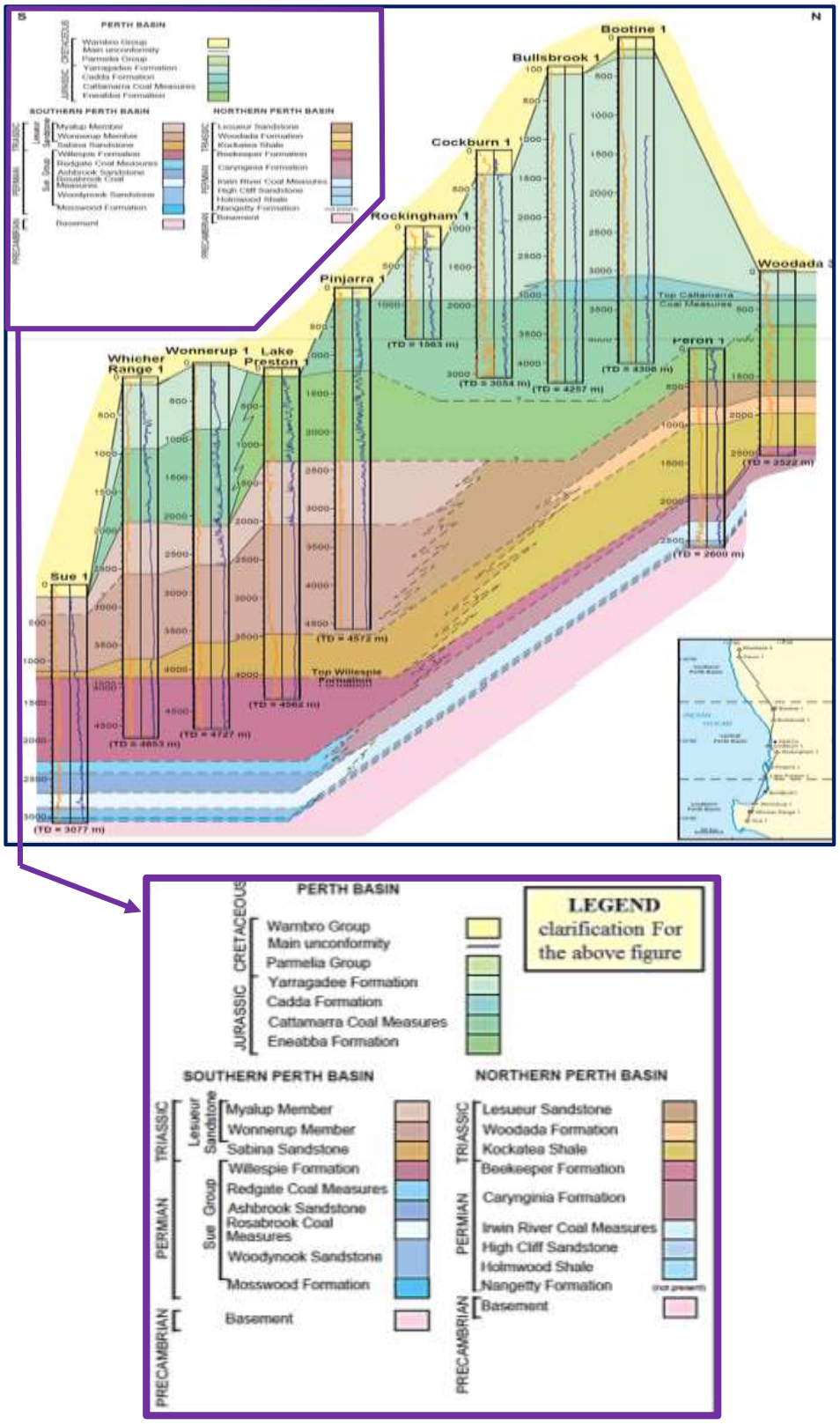

Figure 2.4.2: The stratigraphy grounded on the correlation of exploration wells of the central, northern and southern Perth Basin (Crostella and Backhouse, 2000)

2.4.1 Structural and tectonic framework

Perth Basin evolved during the separation of Australia and Greater India in the Permian to Early Cretaceous periods. The tectonic history exhibits a significant variation from north to south in the basin (Lasky, 1993; Song, 2000; Pigram, 2007; Department of Resources, Energy and Tourism-HG 20, 2011). Three rifting phases took place in the region (Figure 2.4.1 and 2.4.1.2). The initial rifting established a series of depocentres in the Permian to Early Triassic, with fluvial and marine siliciclastics, coals and minor fluvial dominating in the north, while fluvial siliciclastics and coal dominate in the south. The second phase of rifting took place in the Late Triassic and Early Jurassic, and is associated with fluvial and deltaic deposits. It is also associated with the Cattamarra Coal Measures (a thick succession of siliciclastics and coals), and in the north Perth Basin is overlain by Cadda Formation (middle Jurassic shale). The third and final rift and breakup phase occurred from the Middle Jurassic to Early Cretaceous, which was associated with the deposition of fluvial and marine siliciclastics (Yarragadee Formation, Parmelia Group and Warnbro Group). Extension and transtension occurred during the Jurassic to Early Cretaceous, and is associated with the continental break-up (Plumb, 1979; Cadman et al., 1994; Harris, 1994; Mory and Lasky, 1996; the Department of Resources/Energy and Tourism, 2011).

In their study, Playford et al. (1976) made the following observations with respect to the tectonic events in the Perth Basin:

1. The breakup during the Early Cretaceous (Valanginian), the Neocomian Unconformity, was interfaced with strike-slip tectonics and volcanism, which influenced the build-up of the tectonic system in the Perth Basin structure.
2. The initial phases of rifting (Early Permian) had established a north–south trending trough at the down end of the axis of the Basin, while in the north this trough was initially filled by coarse-consolidated masses of unweathered conglomerate sedimentary boulders.

In a different description of the Perth Basin structure of Australia, Song (1999) (after Lasky et al., 1991) reported that two major tectonic phases were recognised: The Permian extension in a south-westerly direction and the early Cretaceous transtension (extension) to the northwest during the breakup. Two movements were inferred, sinistral and dextral, respectively, along the major north-striking faults during these phases, and were rejuvenated by breakup tectonism, which caused horizontal displacements. Theses faults gave an evidence of the generation of strike-slip movement and normal dip-slip. On seismic sections, the appearances of such structures are important as they indicate the strike-slip movements and therefore the development of pull-apart basins.

Many near-surface or shallow strike-slip faults are associated with normal faults. The overall fault geometry is transtensional and lead to the formation of negative structures known as 'negative flowers', with dominant normal faults (Figure 2.4.1.1). The identification of such structures in the Perth Basin is regarded as a reliable indication of strike-slip features.

Davidson and Yu (2006), in their wide-range study on the Perth Metropolitan Area showed that there are only seven faults defined, one of which includes the Darling fault. Continental break-up is marked by a regional Neocomian unconformity, the

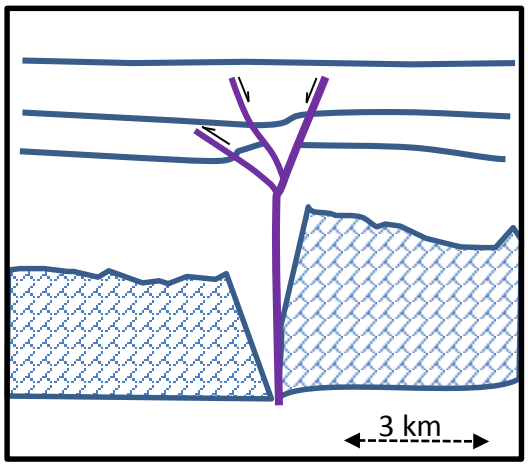

Figure 2.4.1.1: Sketch of a 'negative flower' structure, a termination of strike-slip fault (modified from Zeng, 2005).

Pre-Neocomian sedimentary. In addition of recognising the faults, rocks are covered by younger and generally unlithified sediments, which seem to be relatively un-distorted. Variability in the distribution and thickness of post-Neocomian sediments has been interpreted to be the result of the overlaying of pre-existing fault blocks with differential compaction.

The fluvial-dominated Yarragadee Formation was deposited across the entire onshore Perth Basin during a middle Jurassic syn-rift phase (Rift II-2 of Song and Cawood, 2000), that resulted in east-west extension (Fairbridge, 1953; Playford et al., 1976; Harris, 1994). The architecture of the Perth Basin structure is the result of oblique rifting during the Permian, Late Triassic to Early Jurassic and Middle Jurassic to Early Cretaceous. Stratigraphic chart of the Perth Basin is shown in Figure 2.4.1.2.

An important study of the Perth Basin was carried out by Collins (2003). In it he observes that the extension during the Permian produced round terrain rifts of deep (up to 15 km) north-south trending basins. Collins (2003) added that the total thickness of the Phanerozoic succession could be more than 15 km. Playford et al. (1976), observed that the basin's eastern margin is defined throughout most of its length by the Darling Fault (Figure 2.4.1.3), which is nearly 1,000 km long and its maximum throw may reach up to 15 km. McPherson and Jones (2005), suggested that the Perth Basin sediments are intensely faulted. The fault direction is north to northwest however east-west fault direction is also present throughout the basin (Davidson, 1995). This is shown in Figure 2.4.1.3

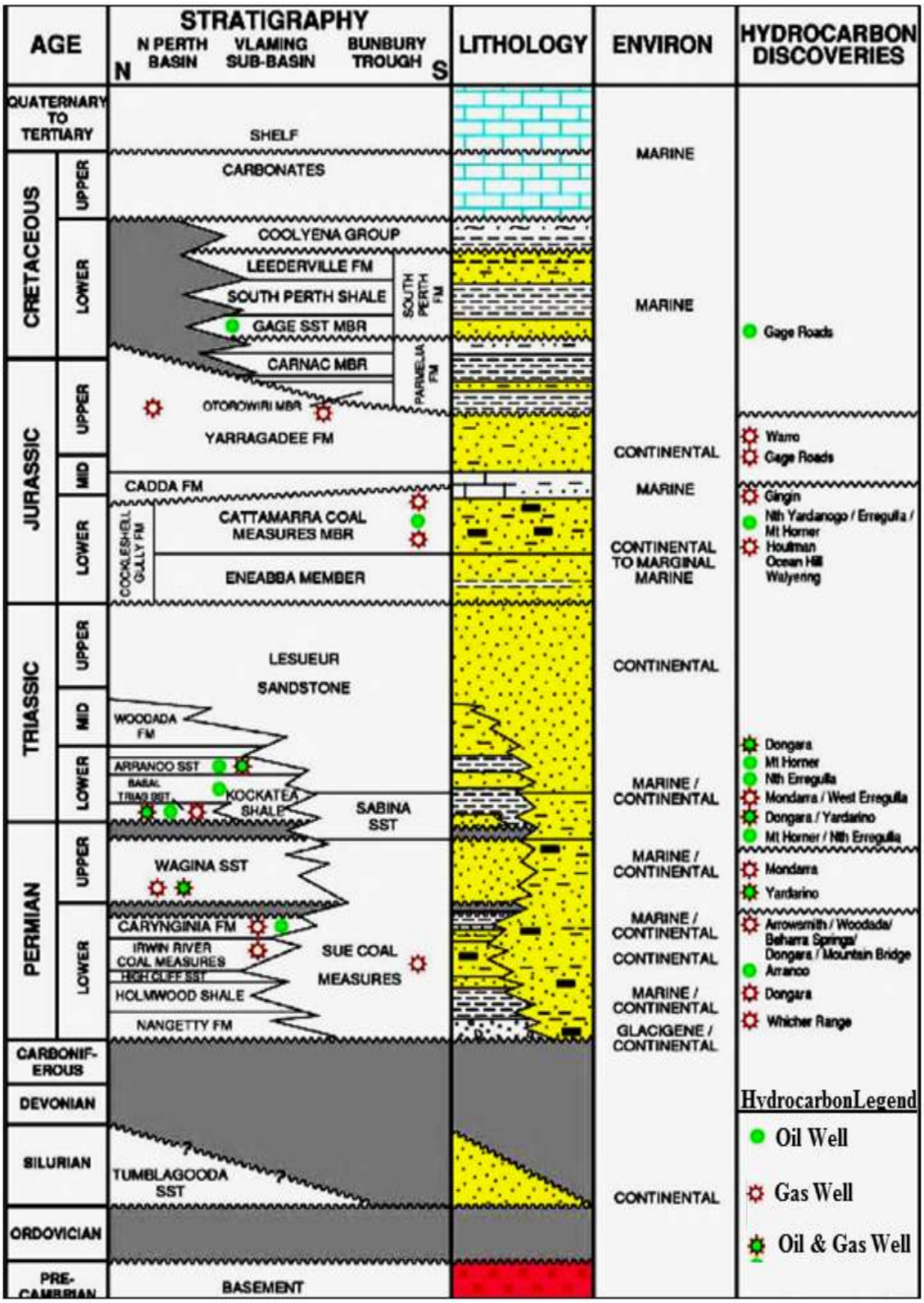

Figure 2.4.1.2: Stratigraphic evolution of the Perth Basin with rifting stages during the separation of Australia and Greater India (after Cadman et al., 1994), (from Bradshaw, et al., 2000).

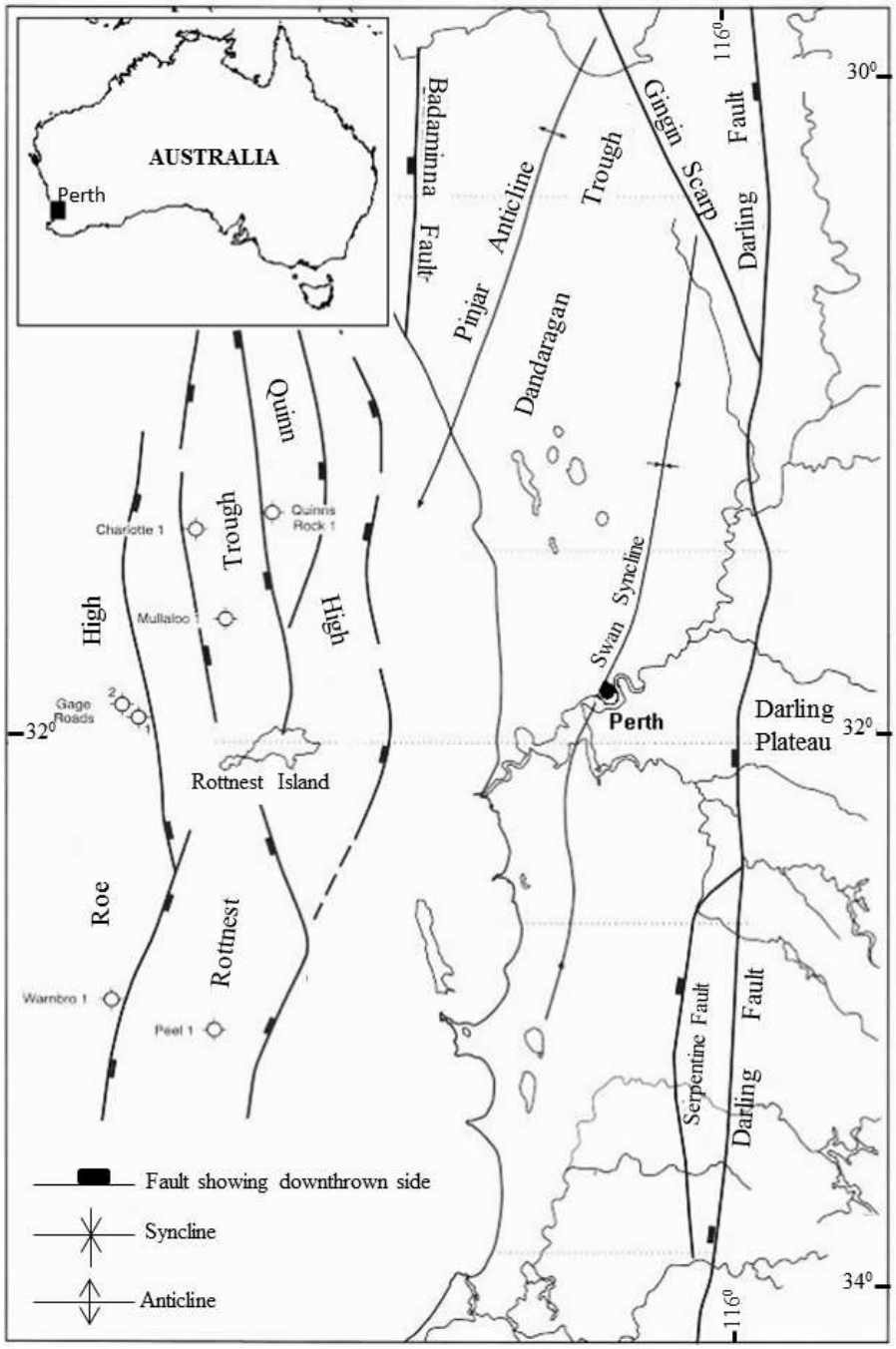

Figure 2.4.1.3: Distribution of tectonic elements throughout the Perth Basin (after Davidson, 1995).

2.4.2 Hydrocarbon importance in Perth Basin

The available petroleum structure studies show that mature source rocks are widespread and the structures are well established for hydrocarbon entrapment throughout the Perth Basin and so the reservoirs are abundant (Owad-Jones and Ellis, 2000). The oil and gas fields are concentrated in the onshore north Perth Basin where thick regional seals are present. They are well developed, particularly in the Lower Triassic Kockatea Shale (Crostella and Backhouse, 2000). Gas and oil shows and their distribution throughout stratigraphic units of the Perth Basin are shown in Figure 2.4.1.2. In onshore north Perth Basin, six commercial petroleum fields have been discovered, which include gas fields at Mondarra, Beharra Springs and Woodada, oil and gas fields at Dongara and Yardarino, and the Mount Horner oil field (Bradshaw et.al., 2003)

2.5. The potential role of seismic recorded in the north Gnangara Mound

West Australian Petroleum Pty Ltd (WAPET) was the first company to explore the Perth Basin for hydrocarbons using gravity and seismic in the 1950s and many stratigraphic wells were drilled accordingly. The company used seismic reflection method extensively to study geology and evolution of the onshore Perth Basin (Owad-Janes and Ellis, 2000; Martin, 2008). The regional 2D seismic lines used in this survey totalled 27300 line kms (Figure 2.5.1).

Around 200 wells were drilled at the majority of known hydrocarbon accumulations; the responsibility of the discovery of most of the fields was by WAPET. Lasky and Lockwood (2004) focused on provided interpretation of seismic and gravity data. Their study focused on deeper seismic events and was based on work completed by the Western Australian Bureau of Mineral Resources (Owad-Jones and Ellis, 2000)

In previous studies of the area, 2D shallow seismic interpretation has not been given much attention. There is a general lack of high-quality shallow seismic imaging in the Perth Basin. Recently, high resolution 2D seismic reflection data has been collected across the Gnangara Mound in the Perth Basin, Western Australia. The surveys were collected to better understand the relationship of Perth's major aquifers in this

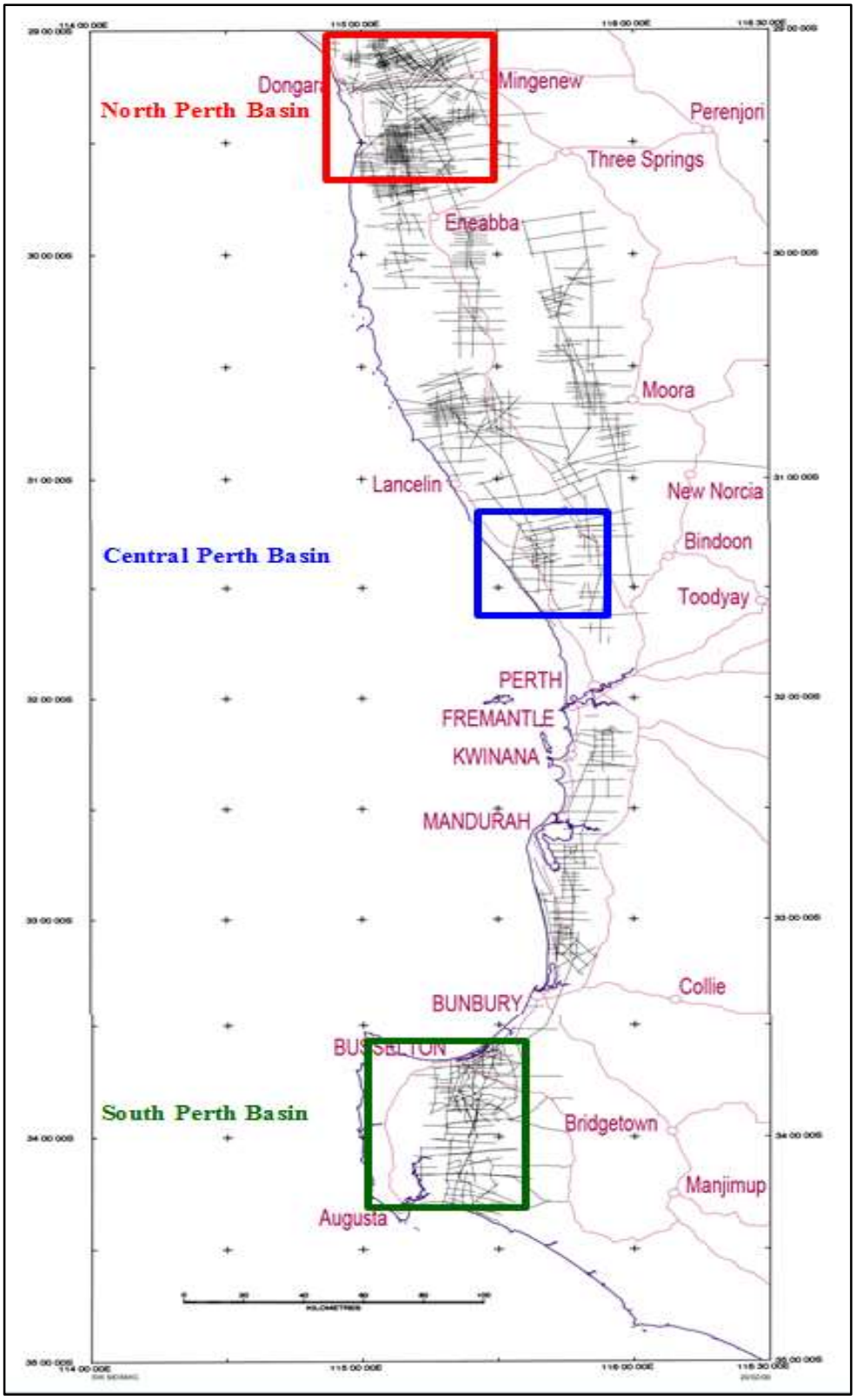

Figure 2.5.1: 2D onshore seismic surveys across the Perth Basin, Western Australia (after Owad-Janes and Ellis, 2000).

hydro - geologically complex area. Formations like the Leederville and Yarragadee have massive areal extent and are highly significant for water supply. Sedimentological detail, such as the orientation of deposition, is often unclear and detailed seismic interpretation may help refine the current understanding of these important formations. Variations in petrophysical properties, particularly porosity and permeability across the formations are only modelled rather than physically investigated or measured on a large scale.

Many researchers have completed seismic reflection interpretation; Valenta, et al. (2008), used forward modelling of various sedimentary structures to aid in the interpretation of 3D seismic reflection data. Exploration of the Perth Basin has led to the discovery of nine new hydrocarbon fields.

2.5.2 Recent seismic survey of the north Gnangara Mound

The Gnangara Mound is the most significant source of groundwater that supplies the Perth metropolitan area. The seismic surveyed area is located 70 km north of Perth on the Swan Coastal Plain and spans more than 200 km^2. It is bounded by the coast line to the west, Gingin Brook to the north, Gingin Scarp and Darling Scarp to the east and the Swan River to the south. The Mound has an area of 2150 km^2 (De Silva, 2009) (Figure 2.5.2.1).

More than 50 km of seismic reflection survey lines were collected by the Curtin University Department of Exploration Geophysics and processed to a high quality. Six available seismic lines (Figure 2.5.2.2 and 2.5.2.3), the Tuart Road and Clover Road were the main dip lines where seismic interpretation was carried out.

The 2D data acquisition at Tuart Road and Clover Road (Figure 2.5.2.2-3) consisted of the following (Harris et al., 2011):

Tuart Road Transect ... seismic Reflection with number of shot Records =1424

Cover Road Transect … seismic Reflection with number of shot Records =1843

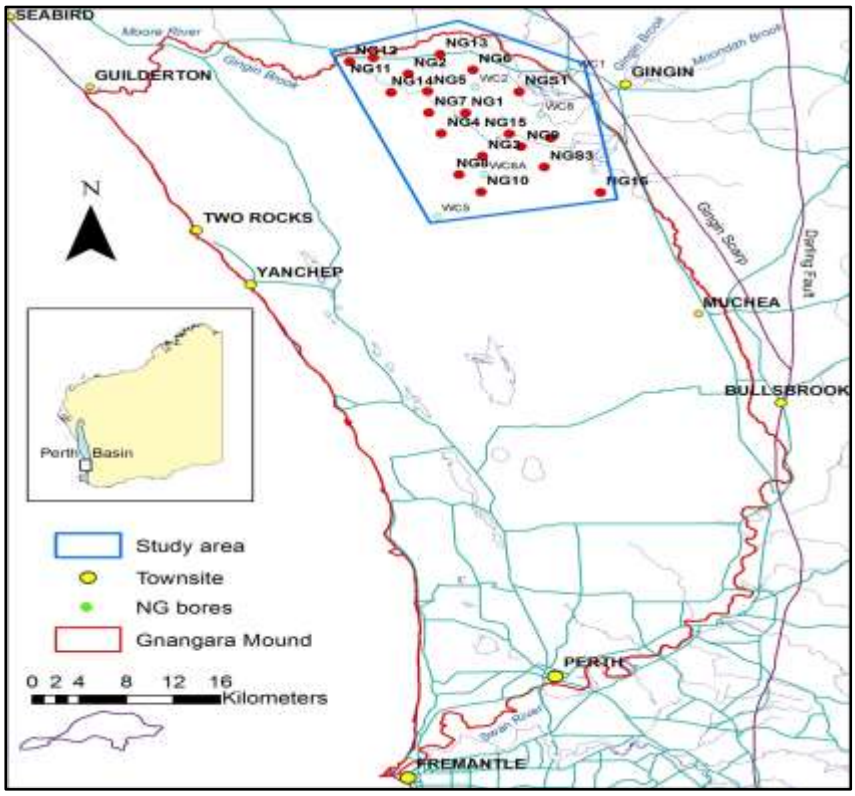

Figure 2.5.2.1: The north Gnangara Mound (from Pigois, et al., 2010)

Acquisition parameters were as follows:

- 300 channel distributed array seismic acquisition system
- Split-spread configuration
- Geophone spacing = 5 m
- Source point spacing = 10 m.
- Free fall weight drop (WD) source, six impacts per shot station
- WD was mounted on a tracked skid steer. The acoustic wave is generated by a 1400 kg steel block being drop from 1.2 m height.

Recording parameters were:

Sample rate = 1 msec,

Trace length = 2.5 sec

A basic processing flow consisted of: amplitude recovery, deconvolution, single and multi-channel filtering to remove source generated noise, static and dynamic corrections, followed by stacking and post-stack migration. 2D seismic interpretation utilised mainly migrated seismic lines. Three strong reflectors namely, the Neocomian Uncon-

formity, the base of Yarragadee formation and the base of Cadda Formation were readily observable and traceable on all seismic lines. Seismic interpretation confirmed several known main structures and proposes the existence of new and more complex structures.

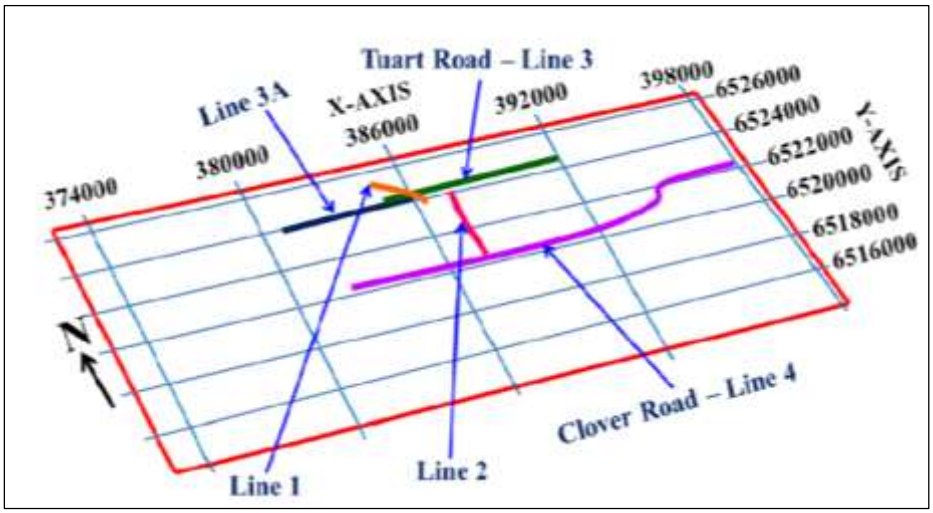

Figure 2.5.2.2: Seismic lines in the north Gnangara Mound (Harris, et al. 2011)

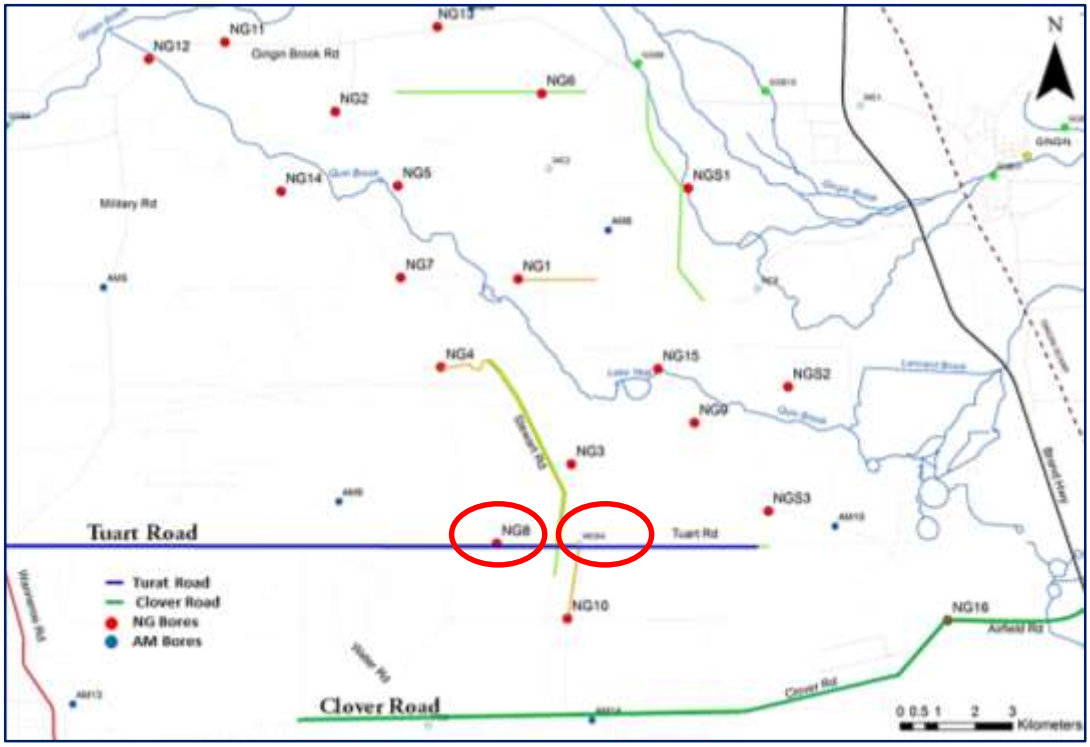

Figure 2.5.2.3: The main study area is in the vicinity of Tuart and Clover roads. Two boreholes of a particular interest are circled in red.

Chapter 3: Seismic response over the north Gnangara Mound

3.1 Introduction

The Gnangara Mound is a very significant area due to the amount of rainfall which is recharged to Perth's aquifers through this area. The research is located in the Yeal area, in the north Gnangara Mound in the Perth Basin (Figure 2.5.2.3).

Previous works in this area include the drilling of 54 boreholes to estimate the location of the water tables and to determine the hydraulic connectivity (Figure 3.1.1). The seismic application objective was to confirm the continuity of the main units and their structural integrity, particularly in the near surface, 0–500 m depth. Consequently establishing correlation between seismic and log data was essential for advancing the interpretation. Two boreholes, NG8 and WC6a, labelled with red circles in Figure 2.5.2.3, along Tuart Road in the north Gnangara Mound were used to correlate seismic data shown in 3.1.1. Only a gamma ray log was available for this task, and therefore only indirect correlation was established.

NG8 is one of the two boreholes that passed through the study area, 50 m to the north of Tuart Road. The gamma ray was interpreted in NG8 through which the Neocomian unconformity was identified (Figure 3.1.1). The gamma logs (Kayal, 1979; Norris, 1972) verified hydraulic continuity along three interfaces: at the water table (30–50 m depth), between the Superficial and Leederville aquifers, and between the Leederville and Yarragadee aquifers. The high resolution seismic identified the interface between the Superficial and Leederville aquifers and the interface between Leederville and Yarragadee formations or aquifers as the angular Neocomian unconformity (Figure 3.1.1 and 3.1.2). The reflection signal is weak at depths of less than 30 meters, primarily due to a reduced fold caused by the application of stretch mute.

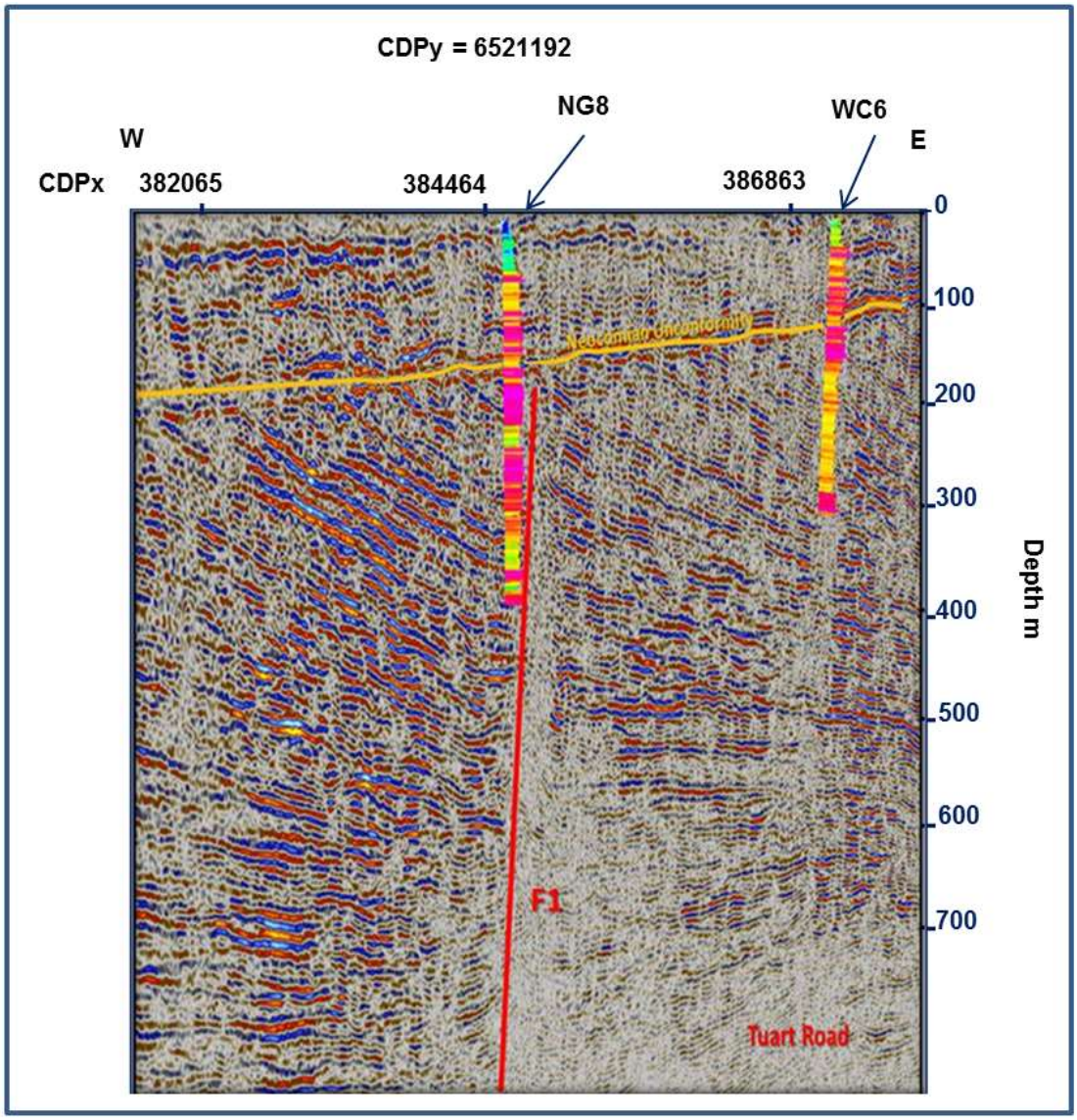

Figure 3.1.1: Seismic Line-3 along Tuart Road 50 metres north of the well bore NG8 and 300 meters east of WC6. Gamma ray log clearly viewed at the Neocomian unconformity.

The gamma ray log (Howell, 1939) measures the gamma radiation to characterise the rock type or sediment in a borehole and is normally recorded in API units of radioactivity (American Petroleum Institute), which is defined as the measurement of the natural radioactivity of the formation. This is because radioactive elements tend to be concentrated in shales, and therefore the gamma ray normally reflects the shale content in the formation. While the resistivity log can be defined as the degree to which a substance resists the flow of the electrical current, measured in Ohms.

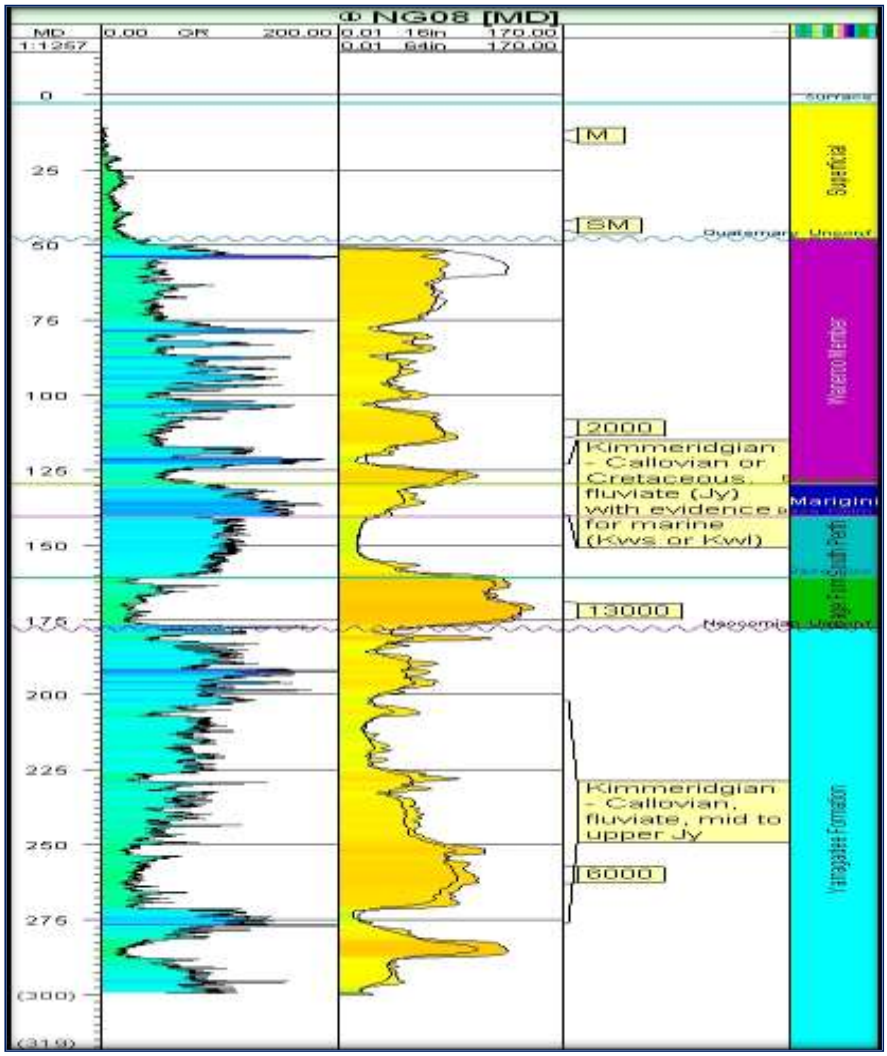

Figure 3.1.2: Geophysical gamma ray log of borehole NG8, which identifies different formations in depth (Pigois et al, 2010).

The gamma ray log of borehole NG8 shows the sedimentation break (unconformity) at a depth around 50 m and below it, the Yarragadee formation at depth 54–130 m (around 80 m thick) characterised mainly by sandstone and mixed with clay, shale and silt (Figure 3.1.2).

Different types of rock emit different quantities and different bands of normal gamma radiation. A high radioactivity causes the deflection of the curve to the right and low radioactivity to the left. Thus high radioactivity readings indicate shale, while low readings indicate clean, non-shale formations such as sandstone, limestone and dolomite (Thomas, 1983).

Shales usually emit more gamma rays than other sedimentary rocks because radioactive potassium is a common component in their clay content (uranium, potassium and thorium are other key radioactive elements found in shale). This difference in radioactivity distinguishes shales from sandstones. The value of gamma-ray (GR) is high in shale.

Depth in meters from surface	Gamma ray log (GR)	Resistivity log (MD)-Ohm
80	Shale is high , API = 190	Sandstone is low = 30 Ohms
124	Shale is high , API = 190	Sandstone is low = 25 Ohms
126	Shale is low , API = 50	Sandstone is high = 90 Ohms

Table 3.1.1: A comparison between the gamma ray log and resistivity log, as shown in Figure 3.1.3

GR is the best log for correlation (Asquith, 1982). The API calibration is between 0.00 and 200.0 as shown in the NG8 gamma ray log (Figure 3.1.2). Shale reaches an API of 200. Gamma ray logs are useful in determining grain size. Sandstone and pebble conglomerates correlate with low gamma radiation readings (high resistivity response; compact sandstone and more consolidated) and shale correlates with high gamma radiation readings (Low resistivity response; loose sandstone and less consolidated (Krassay, 1998). Figure 3.1.2 shows the gamma ray log of borehole NG8, one of the 54 shallow bores in the Gnangara Mound, most of which reached the Yarragadee formation.

A correlation is made between gamma ray and resistivity logs, as shown above in Table 3.1.1 The gamma log shows a high value of API (190 at a depth of 80 m), which means the rock is rich in shale. This difference in radioactivity between shales and sandstones allows the gamma tool to distinguish between shales and non-shales, while the corresponding resistivity response at the same depth (80 m) is low,

at about 30 Ohms. This corresponds to sandstone of low resistivity (soft or lose sandstone or sedimentary rocks).

3.2 Geological and structural interpretation

The Perth Basin is intensely faulted with most faults having north to northwest trends. The dominant structural feature in the region is the Darling Fault, which bounds the Perth Basin to the west from the Precambrian rocks to the east. There was active normal displacement during deposition, which lead to the Permian to Neocomian sediments being thickest just west of the fault. Locally, the Badaminna Fault in the west and Gingin Fault to the east are the local expressions of the last stages of Australia's separation from India (Figure 2.4.1.3) (Janssen et al., 2003).

The Yarragadee aquifer is the main source of water in Gnangara Mound and the focus of this study. It is mainly comprised of sands interbedded with silts and clays. Sand units can be up to 40 m thick, while the silt and clay horizons are generally less than 15 m thick. The age of Yarragadee Formation ranges from Tithonian to Callovian, and paleological evidence suggests it was likely deposited in a predominantly fluvial environment with minor marine influence (Piogois et al., 2010).

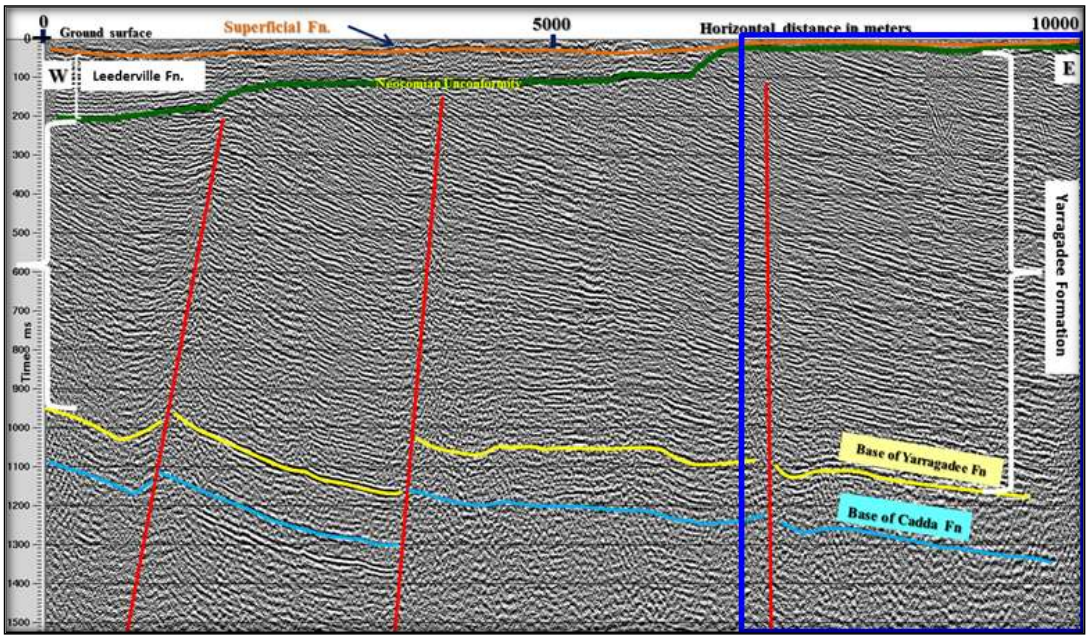

Figure 3.2.1: Migrated seismic section at the Tuart road line. The 10 km length shows the picked strong reflectors and the major interpreted faults in red.

Five reflectors with a good continuity were picked, namely, the shallow Superficial aquifer (Quaternary), Leederville aquifer (Lower Cretaceous), Neocomian Unconformity (Upper or early Cretaceous), the base of Yarragadee aquifer (Middle and Upper Jurassic), and the base of Cadda Formation (Middle Jurassic) (Figure 3.2.1). The Cretaceous and younger sediments dry deposits that move up the Leederville and Superficial aquifers are clearly flat sediments overlying the Neocomian Unconformity, which appears as a strong reflector of angular type with a sharp boundary that terminates the underlain dipping Jurassic formation.

Three major normal faults with west blocks down movement and strike northwest with the throw between 100–200 m are shown in Figure 3.2.1. It is postulated that they were formed as a result of the upward extension of the deep-seated faults formed during the separation of Australia and Greater India in the Permian to Early Cretaceous (Janssen et al., 2003), but do not penetrate the Neocomian Unconformity. The fault planes are close to vertical and the relative slip is interpreted to be predominantly lateral along the plane. As a result of the strike-slip movements, the 'flower' structures are likely to be formed and may be widespread in the Perth Basin.

Figures 3.2.2 and 3.2.3 illustrate the potential 'negative flower' structures within the Yarragadee formation. They are likely to be generated during the third-final rift and breakup phase, which occurred from the Middle Jurassic to Early Cretaceous, and was associated with uplift and erosion, with deep-seated strike-slip faulting. Fluvial sedimentation in the Yarragadee Formation was accompanied by the onset of major extensional faulting (Bradshaw et al., 2003).

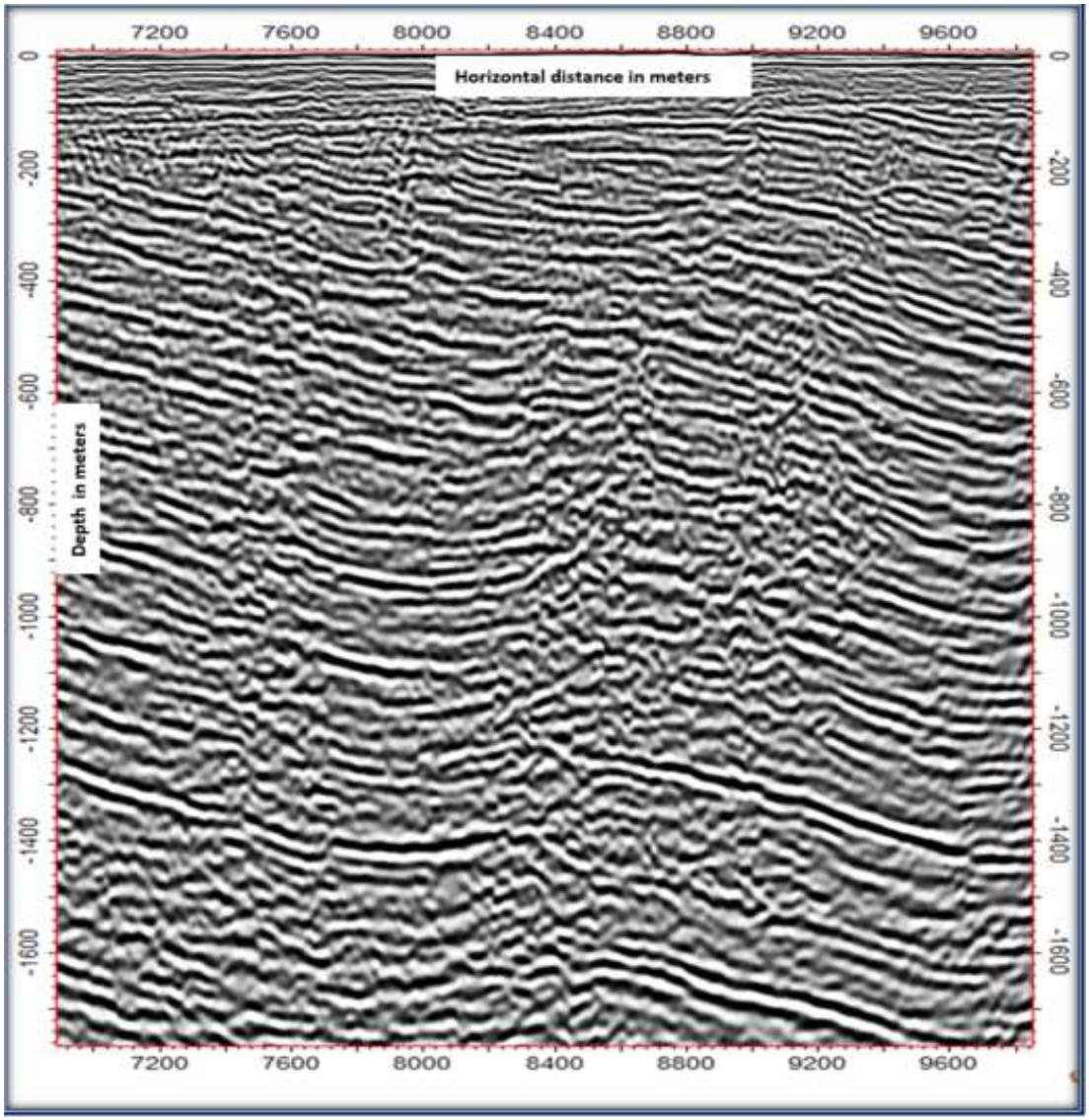

Figure 3.2.2: Tuart Road depth migrated seismic profile before interpretation.

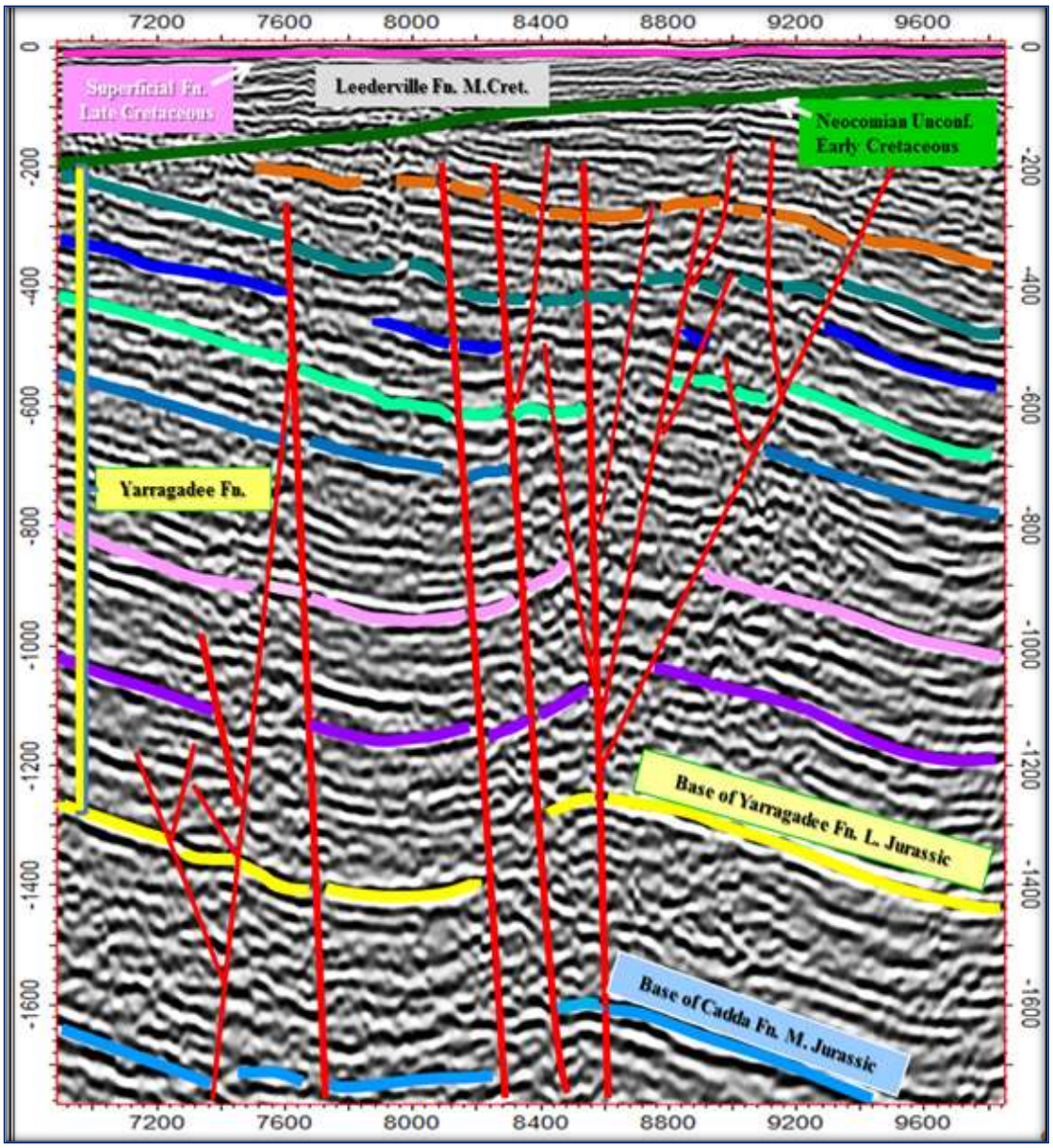

Figure 3.2.3: Tuart Road depth migrated seismic profile after interpretation.

Woodcock and Schubert (1994), described the formation of the ‘flower’ structure as strike-slip fault systems which are characterised by faults that converge downward in two ways: (a) compressional (positive) described as ‘palm tree flower’ structure and (b) extensional (negative) described as ‘tulip flower’ structure (Figure 3.2.4).

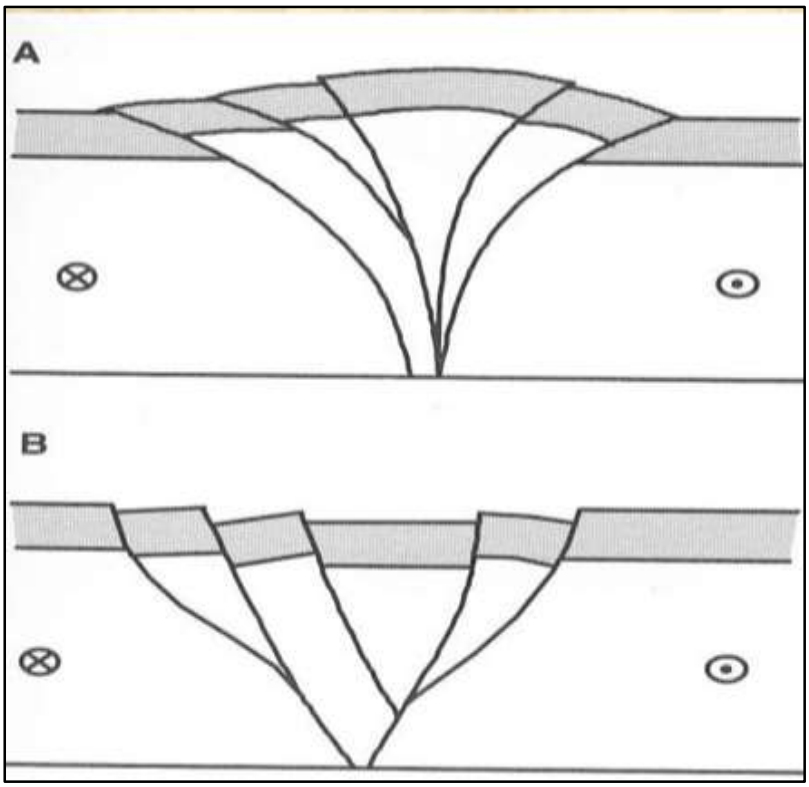

Figure 3.2.4: Two types of 'flower' structure, (a) compressional or positive and (b) extensional or negative, proposed by Woodcock and Schubert (1994).

3.3 2D seismic interpretation summaries

2D high resolution seismic surveying and data processing have enabled detailed interpretation and identification of three major faults offsetting the Yarragadee Formation (Figure 3.2.1). The maximum throw of these faults is estimated to be from 200 to 300 meters. Most of these faults were probably formed as a result of the formation and development of the Perth Basin during the Permian to Early Cretaceous. The big faults extend upward to the Neocomian unconformity, but in general do not penetrate it. The younger sediments are mainly unaffected by late structural activities or they have possibly absorbed minor deformations and undergone subsequent differential compaction. Lasky et al. (1998) suggested that during the continental break-up, sediment accumulation took place which was widespread in the Perth Basin. This provided basic insights into the deformation of the western Australian continental margin prior to, and during, the break-up.

Termination of faults at the unconformity surface could be interpreted as an evidence of erosion during the uplift in the early Cretaceous. Precise timing at which normal faulting terminated at the break-up remains unclear. However, the faults are hard to define by drilling, particularly sparse drilling, and seismic reflection survey remains a principal tool for detecting faults, inferring their geometry and hence deformation history of the basin.

A distinctive ‘flower’ structure faulting system of a ‘negative type’ is proposed within the Yarragadee Formation based on interpretation of the seismic section, as shown in Figure 3.2.3. This is an indication of the strike-slip fault due to the effect of the sinistral and dextral movements that occurred along the major north-south striking faults. These were rejuvenated by “break tectonism”, which caused horizontal displacements, as suggested by Lasky et al. (1991). Proving such structure is difficult and requires additional investigations, which will be shown in later chapters.

Chapter 4: 2D Modelling of complex structures

4.1 Introduction

Initial seismic interpretation of the Tuart Road seismic line proposed the existence of a complex fault system ('negative flower' structure), but could not resolve it well enough to allow for the proper modelling of fluid flow through the Yarragadee formation. To advance this work further, I used forward modelling was used to understand the seismic response over the complicated geological structures of the north Gnangara Mound. However, such study requires a realistic model that is comprised of geological features likely to be found in the basin.

The model requires the "best estimate" of the fault system so that it can generate relevant seismic responses (Barbour, 2004). For that purpose velocity profile is constructed based on logs from the surrounding shallow wells and subsequently extended in depth with root mean square (RMS) velocities computed during field data processing. These velocities and extrapolated density (inverse Gardner's equation) (Crain, 1974) are then used to populate the geological model. The seismic wavelet is extracted from the field data to produce pre-stack full elastic shot records that utilise the geometry, which mimics the one used in field data acquisition. The synthetic data are fully processed. The objective of the synthetic data analysis is to verify if the presence of such complex fault system can be observed and possibly interpreted in 2D seismic data.

4.2 Objectives

2D Modelling is used extensively in scientific studies, but also for exploration objectives. In this research, 2D numerical modelling is deployed for the following reasons:

1. To generate seismic expression of complex flower structure faulting.
2. To establish if such fault structures can be observed and interpreted in 2D data under ideal condition and weather the conventional data processing might create artefacts that could be misunderstood as fault.
3. To determine the methodology required for imaging complex structures.

4.3 Forward modelling

The propagation of seismic waves through the real earth is often numerically simulated in order to analyse and understand the seismic response over different underground layers and structures (Ballesteros, M. W., 1991; Zahradnik, 1995). It is also used to test processing routines, algorithms and flows as well as to help understand the origin of the events (Urosevic and Juhlin, 2007, Anderson, 2000).The choice of the dimensions for modelling is driven by the complexity of the model and the study objectives. 3D modelling is time consuming and can be challenging when it comes to the model construction and subsequent data processing. 2D modelling is the method of choice in many cases, as long as the target complexity is such that its response can be approximated using this method. The most frequently used numerical schemes deploy acoustic wave equations. Post-stack modelling, in the form of exploding reflector approach (Loewenthal et al., 1976), is the most frequently used scheme for producing nearly instant synthetic seismograms. However, this is limited to only simple investigations. Pre-stack acoustic schemes are more meaningful when it comes to studying more complex models, such as investigated in this study. This approach propagates acoustic waves (compressional only) through a "liquid Earth" which in effect means that only compressional waves are considered to propagate through layers of different acoustic impedance or just different velocity if the density is constant.

This type of modelling utilises the simplest form of wave equations, which are derived using two important laws of physics:

1. Newton's second law of motion, which states that the acceleration of a body equals the force acting on the body divided by the mass of the body, and
2. Hook's law of elasticity, which states that the restoring force on a body is proportional to its displacement from equilibrium (Krebes, 2004; Margrave and Manning, 2004; Chopra, 2005, Alaei, 2012).

Conjoining these two laws give the following wave equation (a second-order partial differential equation for the vector displacement u):

$$\nabla^2 u = \frac{1}{v^2} \frac{\partial^2 u}{\partial t^2}, \text{ where} \qquad (4.3.1)$$

∇^2 = is the Laplacian and represents the sum of the second order derivatives of the

wavefield spatially,

u = is the wavefield,

v = is the wave velocity in the medium; also given as the square root of the bulk Modulus to density,

t = time variable, and

$\frac{\partial^2 u}{\partial t^2}$ = is the second order derivative of the wavefield with respect to time.

This equation is commonly solved with the finite difference scheme (Zahradnik and Priolo, 1995).

Because of its capability to produce a good solution in laterally heterogeneous media (Virieux, 1984; Zahradnik, 1995), the next level of sophistication in numerical representation of wave propagation is utilisation of the elastic wave equation, which deals with all types of wave (direct waves, primary reflected waves, and multiply reflected waves). The isotropic elastic wave equation has a form:

$$\rho \frac{\partial^2 u}{\partial t^2} = (\lambda + 2\mu)\left(\frac{\partial^2 u}{\partial x^2} + \frac{\partial^2 w}{\partial x\,\partial z}\right) + \mu\left(\frac{\partial^2 u}{\partial z^2} - \frac{\partial^2 w}{\partial x\,\partial z}\right), \text{ and} \quad (4.3.2)$$

$$\rho \frac{\partial^2 w}{\partial t^2} = (\lambda + 2\mu)\left(\frac{\partial^2 u}{\partial x\,\partial z} + \frac{\partial^2 w}{\partial z^2}\right) + \mu\left(\frac{\partial^2 w}{\partial x^2} - \frac{\partial^2 u}{\partial x\,\partial z}\right), \quad (4.3.3)$$

where ρ = density, λ = wavelength, and μ = shear modulus

The elastic wave equation is considered to be the most accurate method in terms of its ability to simulater wave propagation through real earth materials. However the resultant solution can be overwhelming. This equation can be conveniently solved with finite differences albeit requiring higher order spatial derivatives (Kelly et al., 1976). A more stable and significantly more effective method was proposed by Virieux (1986), when utilises these Elastodynamic equations:

$$\frac{\partial^2 u_x}{\partial t^2} = \frac{\partial \tau_{xx}}{\partial x} + \frac{\partial \tau_{xz}}{\partial z}, \text{ and} \quad (4.3.4)$$

$$\frac{\partial^2 u_z}{\partial t^2} = \frac{\partial \tau_{xz}}{\partial x} + \frac{\partial \tau_{zz}}{\partial z}, \text{ where} \quad (4.3.5)$$

$$\tau_{xx} = (\lambda + 2\mu)\frac{\partial u_x}{\partial x} + \lambda\frac{\partial u_z}{\partial z}, \tau_{zz} = (\lambda + 2\mu)\frac{\partial u_z}{\partial z} + \lambda\frac{\partial u_x}{\partial x}, \text{ and} \quad (4.3.6)$$

$\tau_{xz} = \mu\left(\frac{\partial u_x}{\partial z} + \frac{\partial u_z}{\partial x}\right)$, where

τ = stress tensor, μ = Elastic Modulus

This is so called the stress-velocity formulation, emphasised by Barthwal (2010), which is implemented in the Tesseral software (tesseral Technology Incorporation, Calgary, Canada, 2007-2015), which was intensively used in this study. The methods produce both compressional and shear waves. It is accurate and computationally efficient.

4.4 Elastic wave modelling

1. 2D modelling with Tesseral software is utilised through several steps. Building a 2D velocity model is quite effective if one has the desired geological cross-section sketched in some form. The section is readily digitised and elastic parameters are assigned with assistance from the local Tesseral library.
2. Acquisition geometry is assigned.
3. Modelling parameters are chosen such as spatial and temporal sample rates, total travel time. These parameters have to be carefully chosen in order to avoid numerical dispersion.
4. Processed "shot records" are then input into the basic processing functions available within the software package or output in SGY form for more elaborate processing with a full commercial processing system, such is ProMAX by Landmark.

The initial geological model was derived from a simplistic interpretation of a 2D seismic line (Figure 4.4.1). A corresponding seismogram, that is, a CMP stack and migrated stack, are shown in Figures 4.4.2(A) and (B), respectively. In this case post-stack modelling was used based on the exploding reflector principle (Loewenthal et al., 1976).

Another model is presented in Figure 4.4.3., when forms a classic 'flower' structure, and now the aim is to investigate the seismic response over it. Post-stack modelling (Figure 4.4.4) produces a similar result to the one shown in Figure 4.4.2. despite the fact that different structural models shown in Figures 4.4.1 and 4.4.3, respectively, were used to generate the synthetic data.

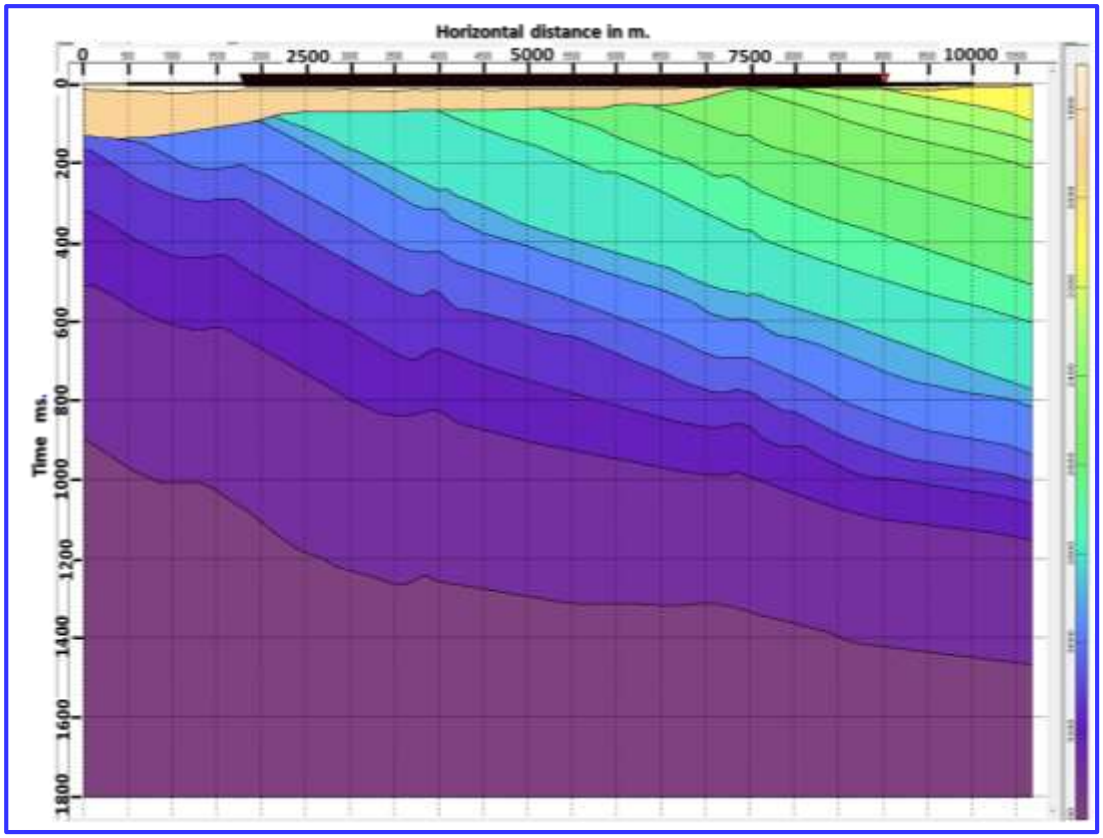

Figure 4.4.1: The geological model interpreted from 2D seismic lines: shots=280, interval=10 m, receivers=300, interval=5 m.

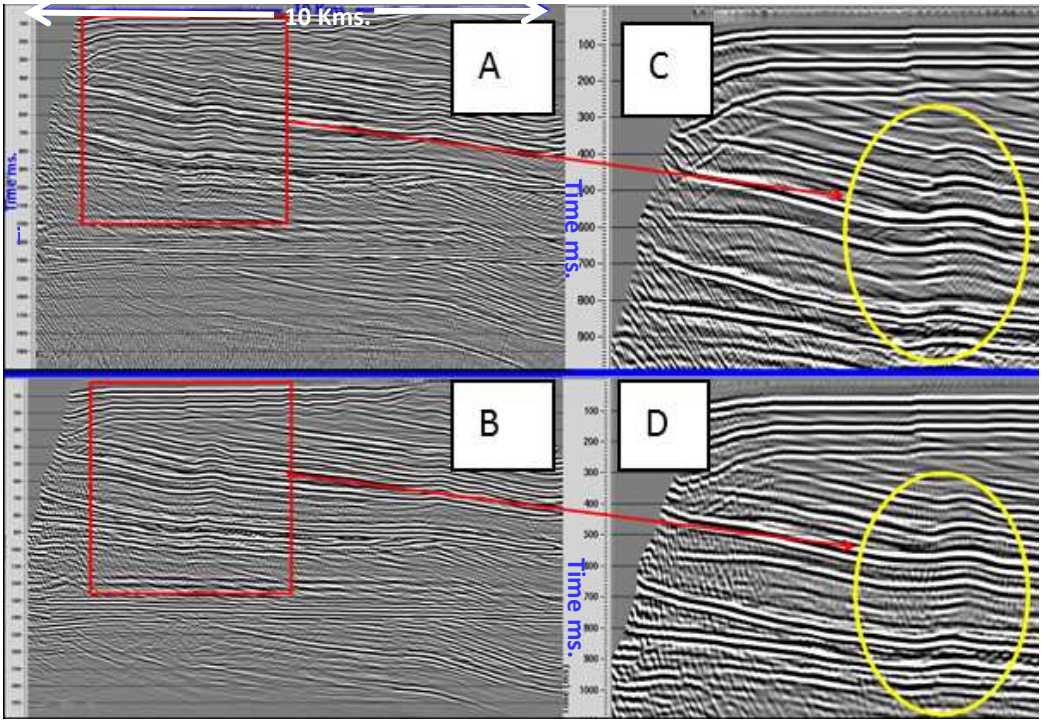

Figure 4.4.2: (A) Synthetic section, (B) the migrated synthetic line, (C) an enlarged structural feature from (A) and (D) the same feature from (B).

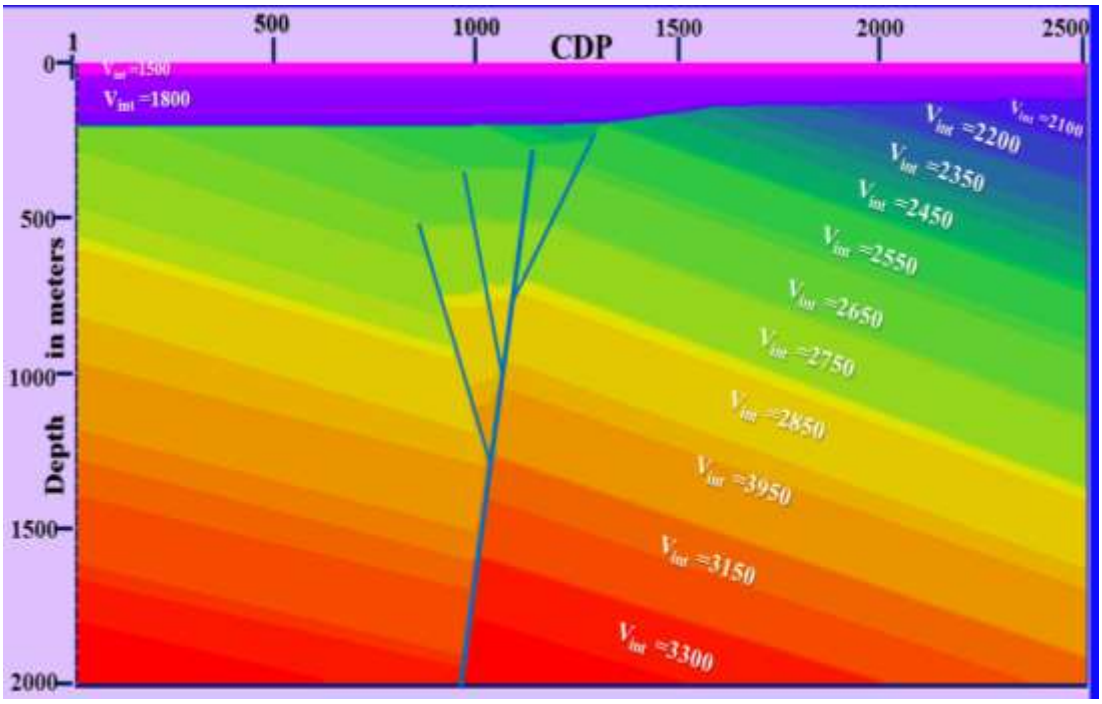

Figure 4.4.3: The 'flower' structure—2D Model with depth increasing velocities.

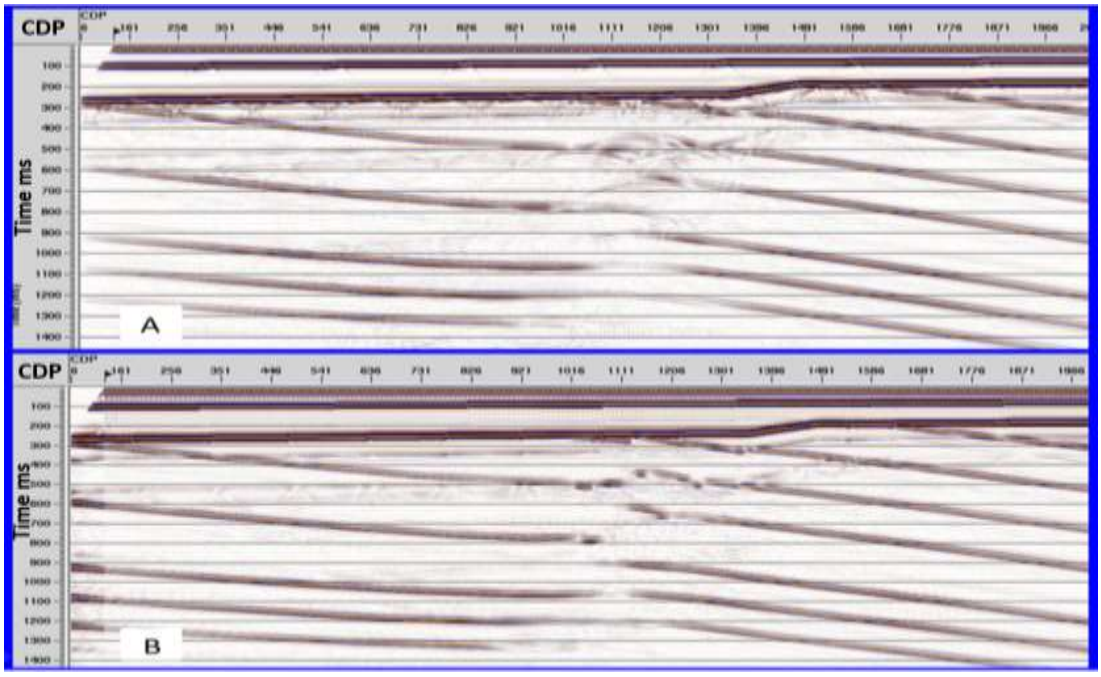

Figure 4.4.4: (A) Stacked synthetic data, (B) the post-stack migrated synthetic stack.

Subsequent modelling included pre-stack approach. 280 shots were fired across the model. Source interval was 10 m. 300 receivers were spaced at 5 m during the "shooting". After pre-processing, pre-stack time migrated (PSTM) sections using the best stacking velocities and true medium that is model velocities were produced, as

shown in Figure 4.4.5 (A) and (B), respectively. Structural breaks can be clearly observed now and a ‘flower’ structure can be inferred with some certainty. Full pre-stack depth migration (PSDM) shows clearly the ‘flower’ structure (Figure 4.4.6) that can be readily interpreted, as shown in Figure 4.4.7.

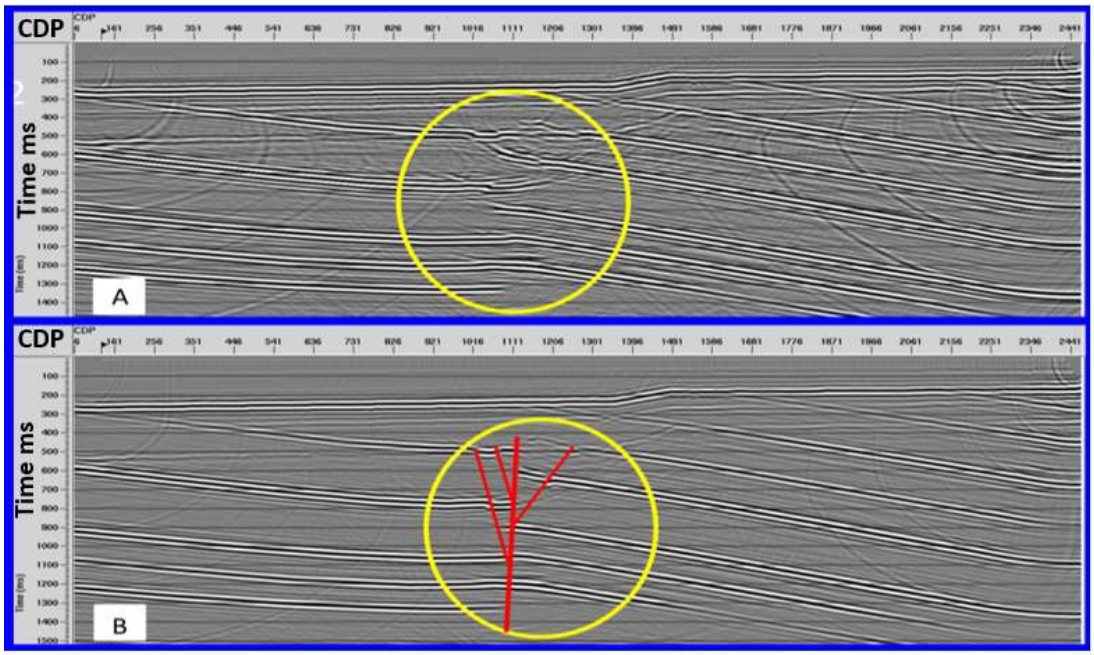

Figure 4.4.5: PSTM sections: (A) using RMS velocity and (B) using true model field velocity.

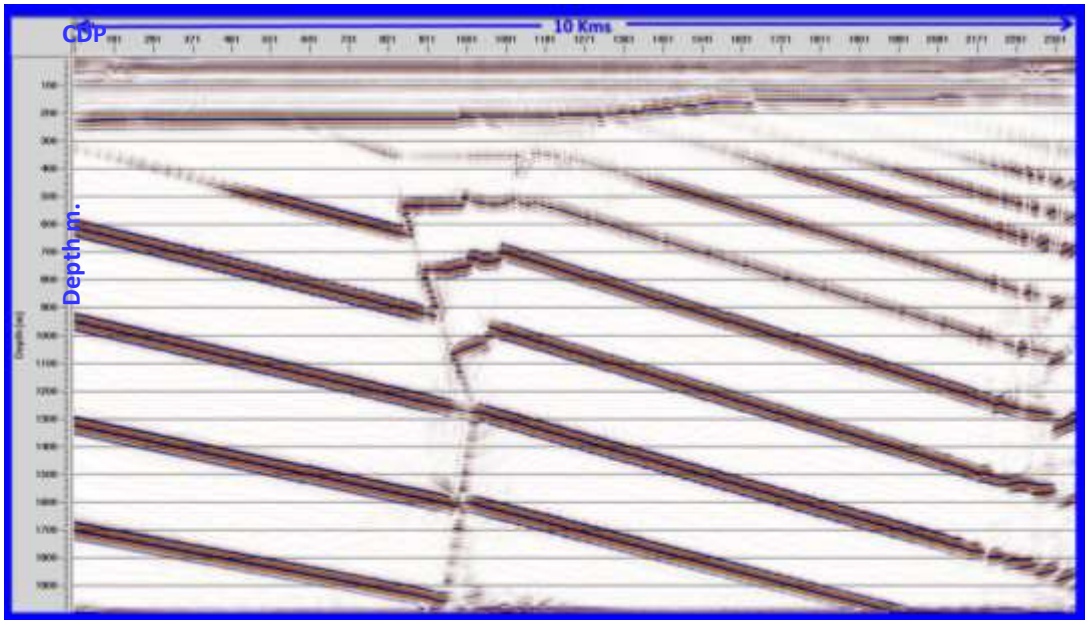

Figure 4.4.6: PSDM (Kirchhoff integral solution) section with true model velocities. The ‘flower’ structure is clearly imaged.

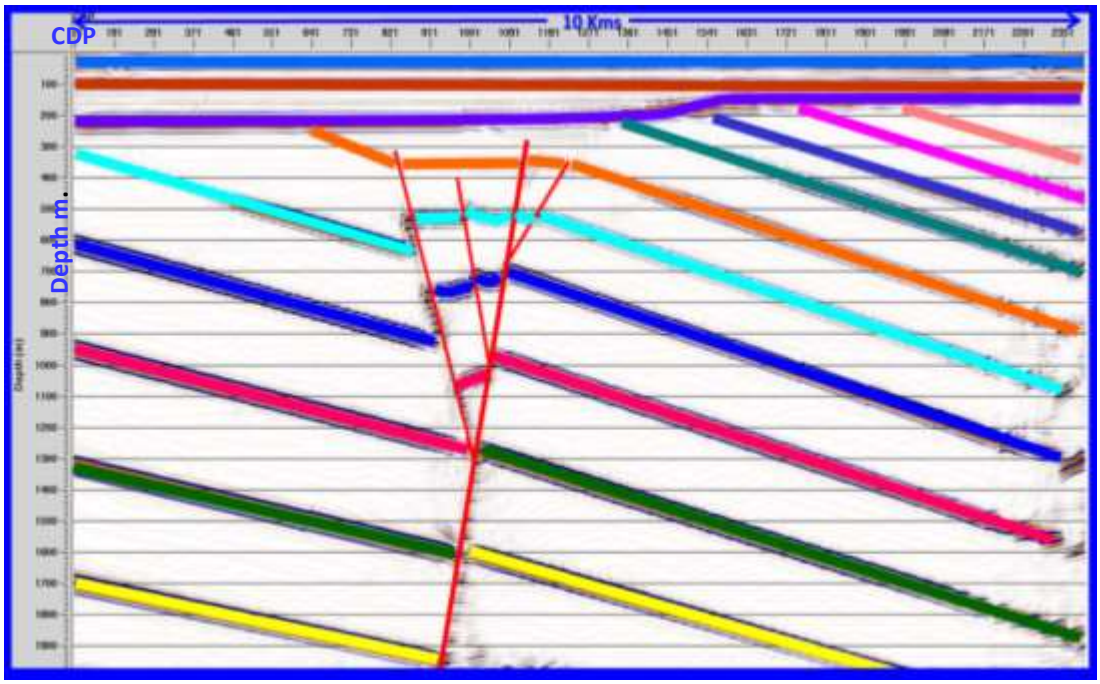

Figure 4.4.7: Interpreted prestack depth migrated (PSDM) section.

Summary

Forward modelling shows clearly an accurate velocity field (Guillaume, 2008) and a high signal-to-noise ratio (SNR) are critical for imaging complex structures, such as the 'flower' structure. After the application of the full pre-stack imaging we arrived at the result that suggested that in a favourable situation (proper dip line orientation) 2D seismic can provide information about complex faulting, which is vital for hydro-geophysical studies. However, it is further shown that only depth migration can fully reveal the nature of the structure. In the field case it is expected that borehole information is required to provide accurate velocities for PSDM. High SNR provided by highly energetic source and/or high fold are further needed to enable good performance on both PSTM and PSDM codes.

Chapter 5: Seismic expression of complex structures – 3D models

5.1 Introduction

The seismic modelling study presented in the previous chapter shows that in an ideal situation it might be possible to detect the presence of complex geological features, such as the proposed 'flower' structure, from 2D seismic data. However, it is be hard to prove its presence from 2D seismic data only, as 'flower' structures are always three dimensional. It is, therefore, of interest to investigate the 3D expression of such structures, particularly in terms of the future exploration strategy in the Perth Basin.

3D modelling can simply be described as the function of plotting points (vertices) within a three-dimensional (x, y and z axis) measured area of space (Fredman, 2008). When the points are connected with lines, they create a "simple polygon" in that space; by creating enough polygons, a three dimensional shape is created. This approach is used to model the response of a three dimensional geological model. The basic advantages of a 3D model generated using real seismic responses are: (a) the target is illuminated from all azimuths and incidence angles, (b) scattering is accounted for, and (c) different acquisition strategies can be investigated. This is subsequently used to devise interpretation approaches and future exploration strategies. For example, 3D modelling can be used to test the effect of different acquisition parameters (Gjøystdal, 2002), such as the shooting geometry or the maximum offset between the source and receiver and/or the difference between surface or so-called layer cake fold and the actual underground fold distributed over the geological targets. The synthetic seismic data is then processed with an optimal sequence that will be eventually used for processing of the field data.

Similar to 2D modelling, 3D modelling schemes can utilise a "liquid earth" model or actual elastic media (Kelly, 2007). The excitation can be a point source (prestack modelling) or the entire underground (3D exploding cube, which amounts to a poststack modelling approach).

The first and often most severe obstacle is building a 3D model representative of the underground geology (Ketcham, 2005). If only 2D information is available then

this process becomes even more challenging. Specifying the acquisition geometry is vital, but not simple, as it will be dependent on the hardware capabilities and would have to be custom specified as current commercial software is not capable of utilising flexible geometries.

5.2 3D modelling investigations

The Finite Difference Method (FDM) is a popular method for numerically solving either 2D or 3D wave equations (Kelly et al., 1976; Claerbout, 1985; Virieux, 1986; Igel et al., 1995; Etgen, 2007; Bansal and Sen, 2008). The foundation of finite difference seismic modelling can be found in several articles (Carcione et al., 2002; Marfurt, 1984; Margrave, 2003; Moczo et al., 2007). Extensive testing of the proposed algorithms are conducted on a so-called Marmousi 3D model created by Versteeg and Grau (1991). It is not easy to analyse and interpret even 3D acoustic seismic responses. A full elastic response is seldom used as it is hard to infer the crux of the problem from the data. Therefore from now on we will concentrate on the acoustic instigations.

.

5.3 3D modelling - finite difference approximations

The acoustic wave equation with the constant density has been most commonly used in seismic modelling (Villarreal, 1997), migration and inversion studies (The most popular scheme for solving the acoustic wave equation is the finite difference method. The methodology can be illustrated on a 1D wave equation, which in a homogenous medium and is given by:

$$\frac{\partial x^2 p}{\partial x^2} = \frac{1}{v^2}\frac{\partial^2 p}{\partial t^2}, \tag{5.3.1}$$

where ρ= ρ(x, t) is a scalar wave field and ν is the velocity.

From Equation (5.3.1), it can be seen that the spatial distribution of pressure wave front is controlled by the medium velocity. Temporal derivatives are commonly solved by the 2nd order finite differences:

$$\frac{\partial x^2 p}{\partial t^2} \approx \frac{1}{\tau^2}\left[-2p_{j,m} + \left(p_{j,m-1} + p_{j,m+1}\right)\right], \quad (5.3.2)$$

Where $p_{j,m} = p(jh, m\tau)$ and Pm-1 is the past pressure, Pm is the present and Pm+1 is the future pressure that we are interested in:

$$\frac{\partial^2 p}{\partial t^2} = \lim_{\tau \to 0} \frac{1}{\tau^2}[-2p_{j,m} + \left(p_{j,m-1} + p_{j,m+1}\right)]. \quad (5.3.3)$$

Consequently, a smaller step in time or space indicates a better accuracy for the computation of progressive derivatives. A higher-order approximation of Equation (5.3.2) can also be derived from the Taylor series. Spatial derivatives are commonly solved with 4th or 8th order of differencing (Liu and Sen, 2009).

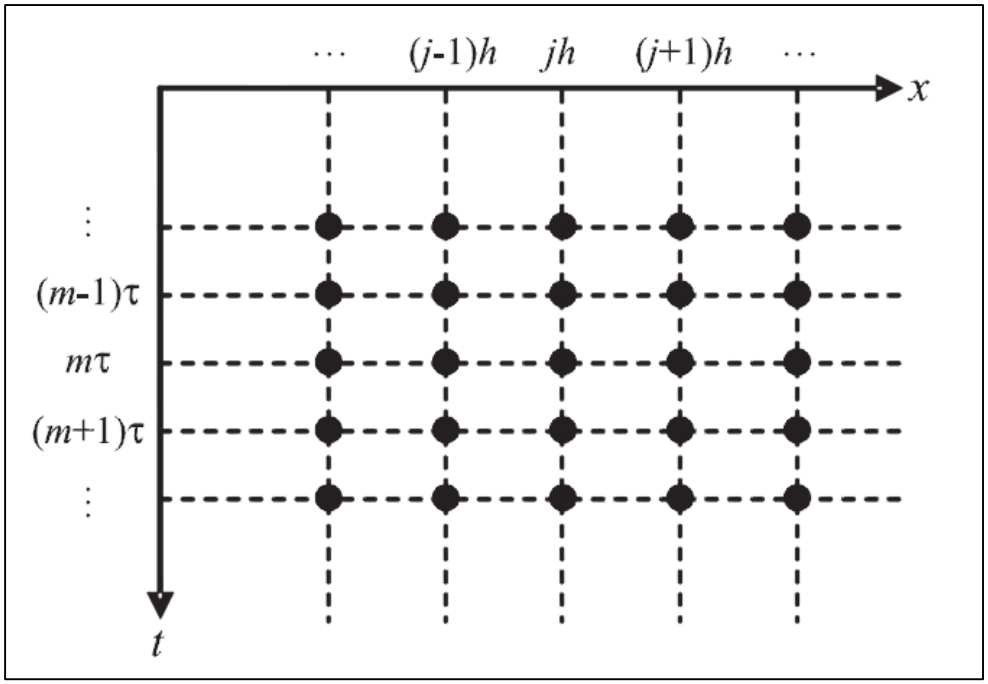

Figure 5.3.1: A diagram designs the grids for wavefields in the time domain; h and τ are grid size and time step, respectively (Liu and Sen, 2009).

Explicit high-order finite difference requires large computer memory and it can be unstable if the spatial and temporal sampling is unmatched through the velocity. Liu and Sen (2009) illustrated the grids for the wavefield in the time-space domain (Figure 5.3.1).

A $2N^{th}$-order finite difference formula for the 2nd-order spatial derivative is given by:

$$\frac{\partial^2 p}{\partial x^2} \approx \frac{1}{h^2}\left[c_0 p_{j,m} + \sum_{n=1}^{N} c_n\left(p_{j-n,m} + p_{j+n,m}\right)\right], \qquad (5.3.4)$$

Where $c_{n\ are}$ the finite-difference coefficients and their expressions are given in the following section. When N=1, we can obtain $c_0 = -2$, $c_1 = 1$, then Equation (5.3.4) is similar to Equation (5.3.2). When N=2, then $c_o = -5/2$, $c_1 = 4/3$, $c_2 = -1/12$. Also, a smaller grid size can help attain greater accuracy for spatial derivatives.

Substituting Equations (5.3.2) and (5.3.4) into Equation (5.3.1), we have

$$\frac{1}{h^2}\left[c_0 p_{j.m} + \sum_{n=1}^{N} c_n\left(p_{j-n,m} + p_{j+n,m}\right)\right] \approx \frac{1}{v^2\tau^2}\left[-2p_{j,m} + \left(p_{j,m-1} + p_{j,m+1}\right)\right]. \qquad (5.3.5)$$

Reorganising Equation (5.3.5), we get

$$p_{j,m+1} = 2p_{j,m} - p_{j,m-1} + r^2\left[c_0 p_{j,m} + \sum_{n=1}^{N} c_n\left(p_{j-n,m} + p_{j+n,m}\right)\right], \qquad (5.3.6)$$

Where $r = v\,\tau/h$. Equation (5.3.6) is the recursion formula for solving the ID wave equation using the finite-difference method. The recursion begins with the wavefield values known at two successive time steps $t=0$ and $t= \tau$. The wavefield values, that is, pressure distribution in space at a future time step, is computed using Equation (5.3.6).

5.4 Building a physical 3D model

As mentioned before, the construction of a 3D numerical model is a quite involved process, particularly if 3D structures were not a priori derived in one of the interpretation software applications, such as GoCAD, Petrel or Geomodeller. A way around this problem is to construct a physical model, and instead of simulating wave propagation, conduct an experiment that involves actual waves (Urosevic and Dzunic, 2013). The "waves" can be in any frequency range as long as they are matched to the model dimensions.

In this study a physical 3D model of the possible geologic 'flower' structure is constructed from wood with dimension 22x10x7cm.This model is filled with a casting and embedding resin between each layer, while the other layers are left hollow (Figure 5.4.1).

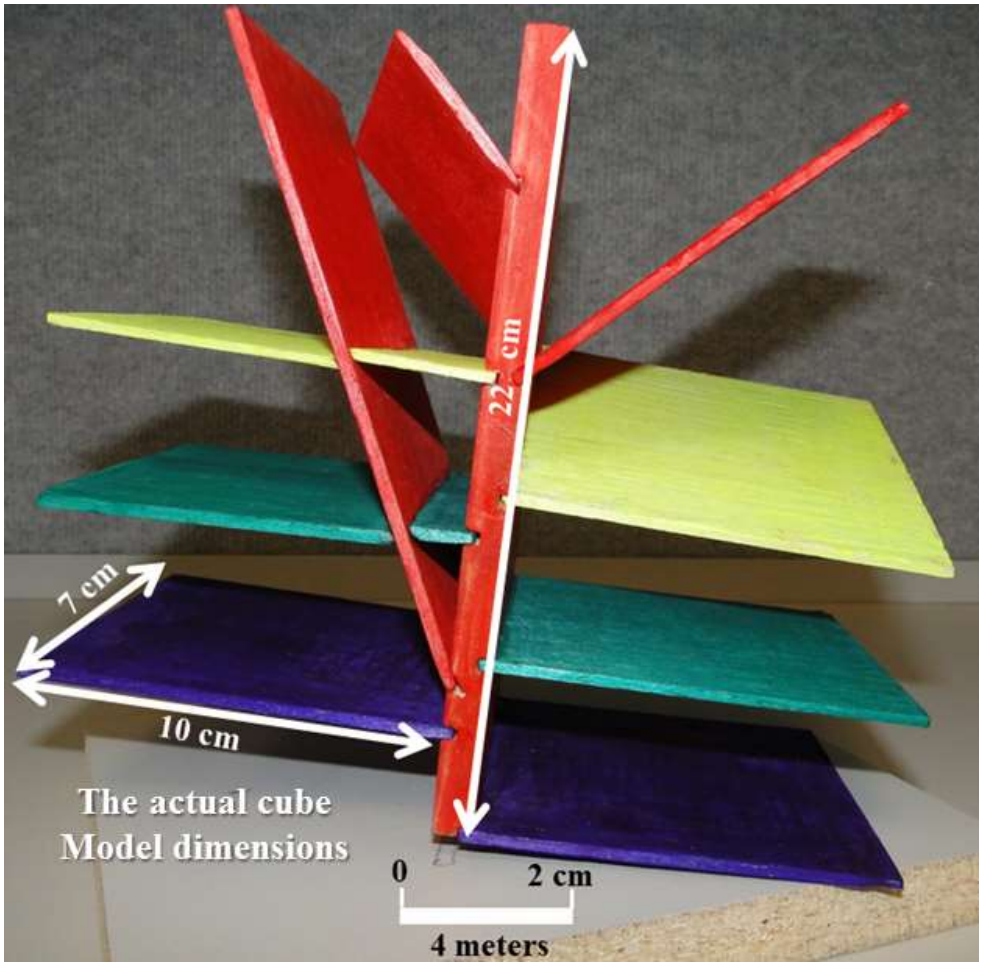

Figure 5.4.1: The physical (wooden) 3D constructed model of the 'flower' structure with the dimensions 22cm x 10cm x 7cm.

5.5 3D Model scanning

The “sources” for scanning the model are in the high-frequency range. A medical computerised tomography or computerized axial tomography (Seletchi, 2007; Engelberg, 2012). (CT or CAT) scan was used to “propagate” the waves through the physical 3D model. Tomography refers to imaging by sections or sectioning, through the use of any kind of penetrating wave (Russ, 1995; Carlson, 2006; Mees, 2003).

In the medical profession, specialised software applications are needed to analyse CT scans and structurally diagnose problems, such as cancers, cardiovascular disease, trauma, and others. It combines special X-ray equipment with sophisticated data processing (Cnudde, 2006) to form images of the inside of the body (Figure 5.5.1). In its basic form it takes many cross-sections to form a 3D image. This is exactly the principle used to create 3D geological models in digital space.

CAT scanning took place in the Royal Perth hospital. Some 410 DCM image sections were taken, which were subsequently used to create a 3D model.

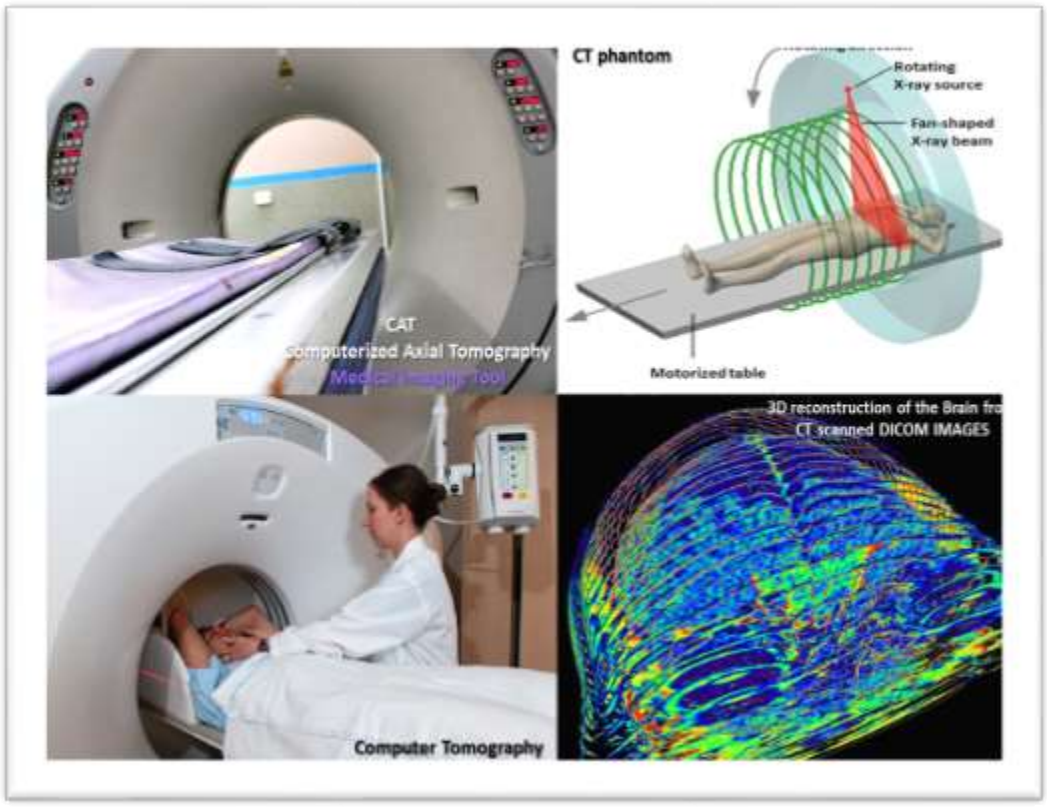

Figure 5.5.1: Images of the CAT scanner as used for medical purposes (Radiologyinfo.org).

A 3D-CT was used to scan through the 'flower' structure physical model (Figure 5.5.2). 410 images were produced and were then used to construct the 3D volume (Mukerji, 2008). The intensity of these images corresponds to X-ray attenuation. These images are saved in the digital imaging and communication (DICOM) image format.

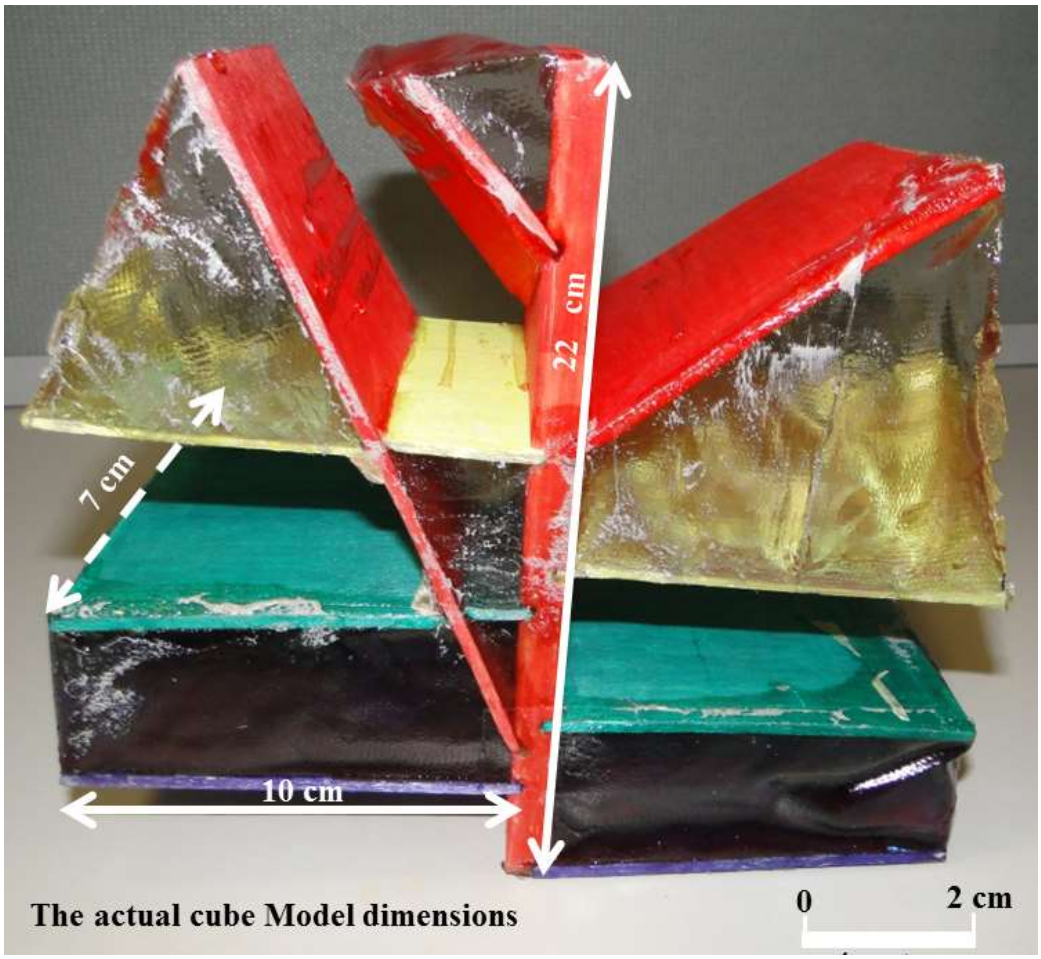

Figure 5.5.2: The 3D physical model of the 'flower' structure is comprised of simple materials such as wood and resins. These materials are used as they support the propagation of X-rays. The model is close to 2.5D but not exactly as some fault planes have different azimuths to the others.

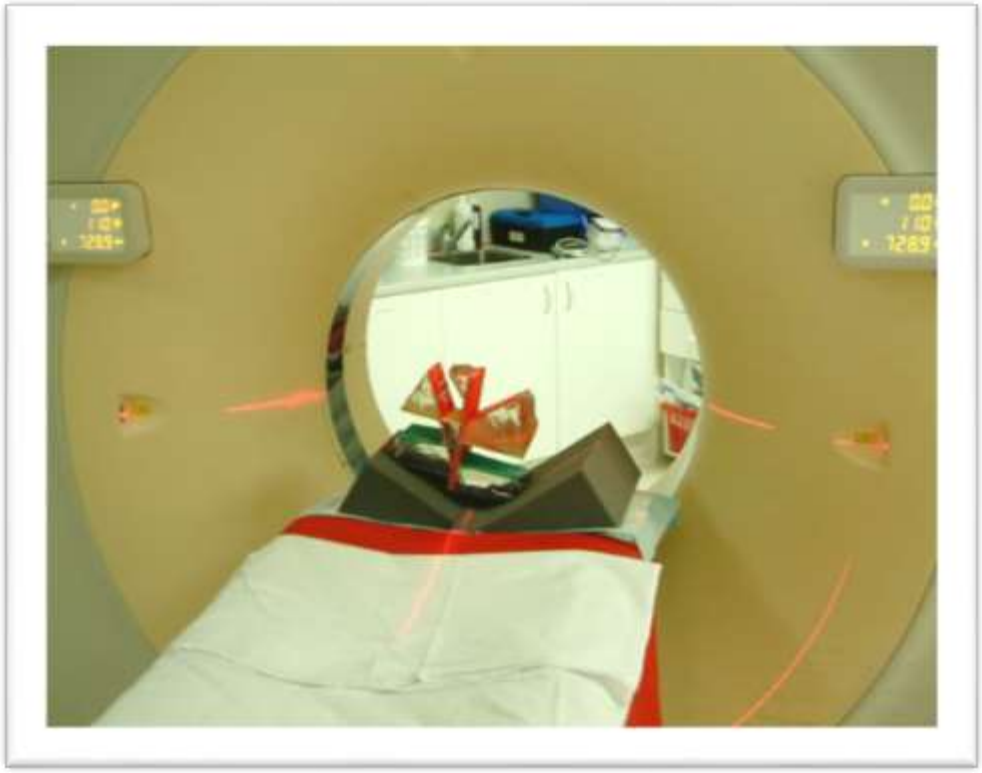

Figure 5.5.3: The 3D physical model inside the CAT scanner.

Figure 5.5.4: A zoomed view the 3D physical model inside the CAT scanner.

Image Compression is typically used: JPG splits image into colour and grey-scale information (Figure 5.5.5). The layers are defined by the CT imaging, but the scanned image is still not ready for the use for the synthetic seismogram creation.

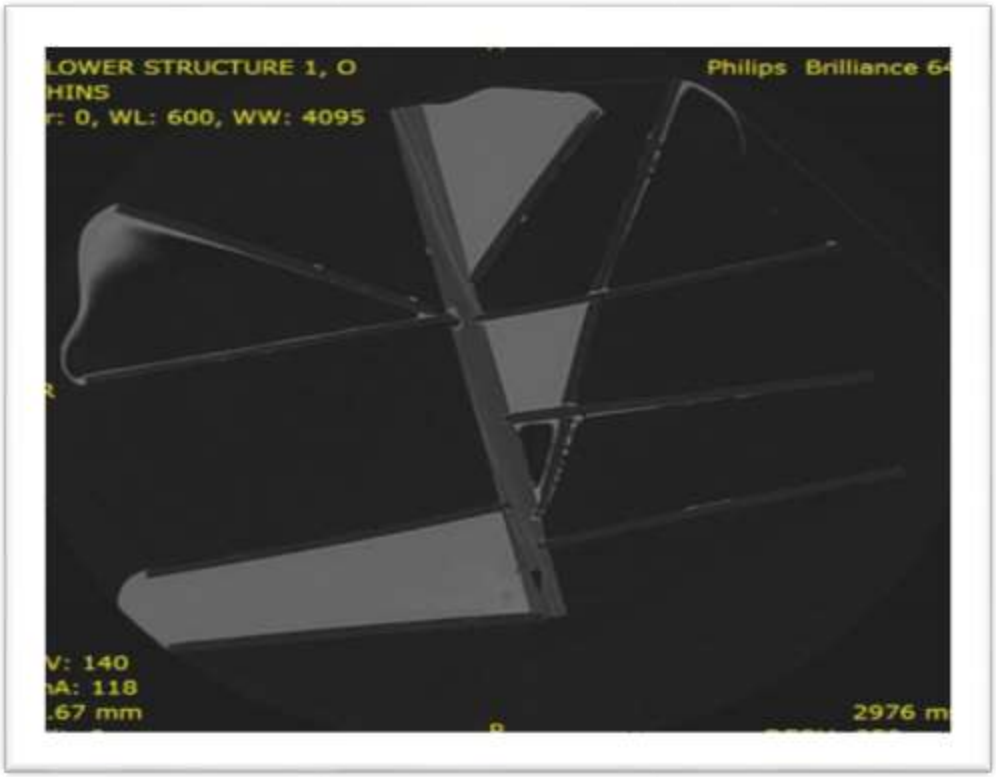

Figure 5.5.5: The JPG Split image of the 'flower' structure in grayscale using the Onis 2.5 image viewer.

5.6 Numerical model creation

The physical 3D model is initially created from a stack of scanned cross-sections (410 sections) using the medical software Drishti (Figure 5.6.1). Each cross-section has dimensions of 768x768 pixels.

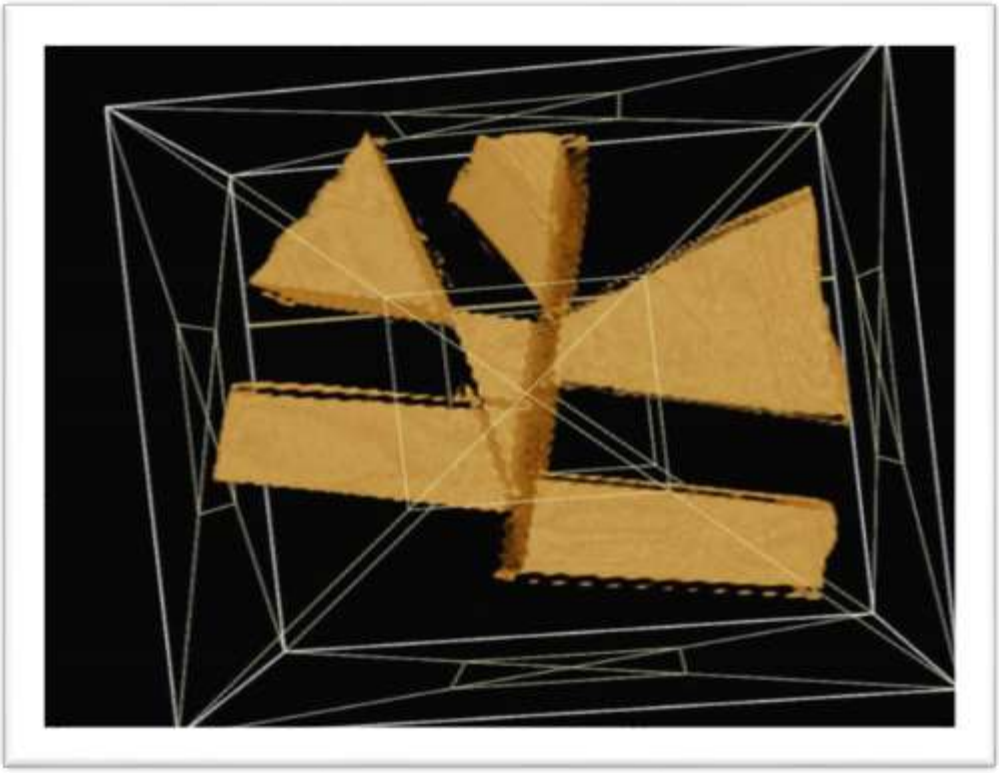

Figure 5.6.1: 410 DCM images are assembled into a 3D model using the Drishti software package.

The CT scanned model parameters are given in Table 5.6.1:

Type	Characteristic
Doc Type	Drishti Header
Raw file	Volume
Voxel type	Short
Pvl Voxel type	Unsigned char
Grid size (model dimensions)	410 x 768 x 768
Voxel size (mm)	0.325521 x 0.325521 x 0.329956
Raw map	-1024.01 x 3070.95 : original CT scan values
Each byte of unsigned integer	0 - 255 8 bit scaled (coded) density values used for velocity mapping
The assigned integer	255 x 255

Table 5.6.1: CT model parameters

The next step is to automatically create the parametrised model that can be used for numerical simulations. For that purpose different density regions are assigned to the appropriate elastic parameters. For that purpose a FORTRAN program was utilised. The code was written by Aleksandar Dzunic (Dzunic, 2014, personal communication) and enabled rapid assignment of elastic parameters.

5.6.1 X-ray analysis

The physical 3D model was created out of the different materials (air, wood, and resin) with different densities that will attenuate x-rays in different ways. These differences will later on be used to assign different elastic properties to the selected "geological" units. Therefore, not just one single material was used to create model, because it will be impossible to recreate an accurate geological model; three different materials with known densities are usually sufficient to build less complex models.

In essence the idea is to create desired shapes with different densities. This is very convenient as user do not need to model in the first instance velocities or any relationships, whether linear or not, between densities and velocities. The ideal case would be to have model densities to equal rock densities. In this case, a single function was used for mapping of the velocities using known density-velocity relationships, preferably for Perth basin.

In practice, the work at first started by analysing the density distribution and then localise zones that are clearly defined and was followed through the x-ray cube (Figure 5.6.2.3). If the regions can be well separated, then the velocity assignment can be readily accomplished. An example is shown in Figure 6.3.1, where separation was chosen for X-ray ranges of 0-120, 121-137, and 138-255. Now, for example, the resin can be selected to represent sandstones with the density range of 1.8 - 2.1. Then assumption for any flexibility can be assumed for this process. For example, it is assigned the velocities of 3500 m/s to a certain intensity range or density; let's say 1.8, while 3800 m/s can be assigned to 2.1 g/cc^3.

5.6.2 Seismic velocities across the Perth Basin

The study of P-wave velocity distribution in depth incorporated some 20 well logs covering the Perth Basin from north to south (Figure 5.6.2.1). The result shows that the Yarragadee Formation depth varies considerably, and is anywhere within the bounds of 300–3500 m. Velocity varies from 2200–4200 m/s (Figure 5.6.3.1). The average velocity depth curve for the Perth Basin is shown in Figure 5.6.2.2.This curve can be utilised to assign most probable velocities to the formations.

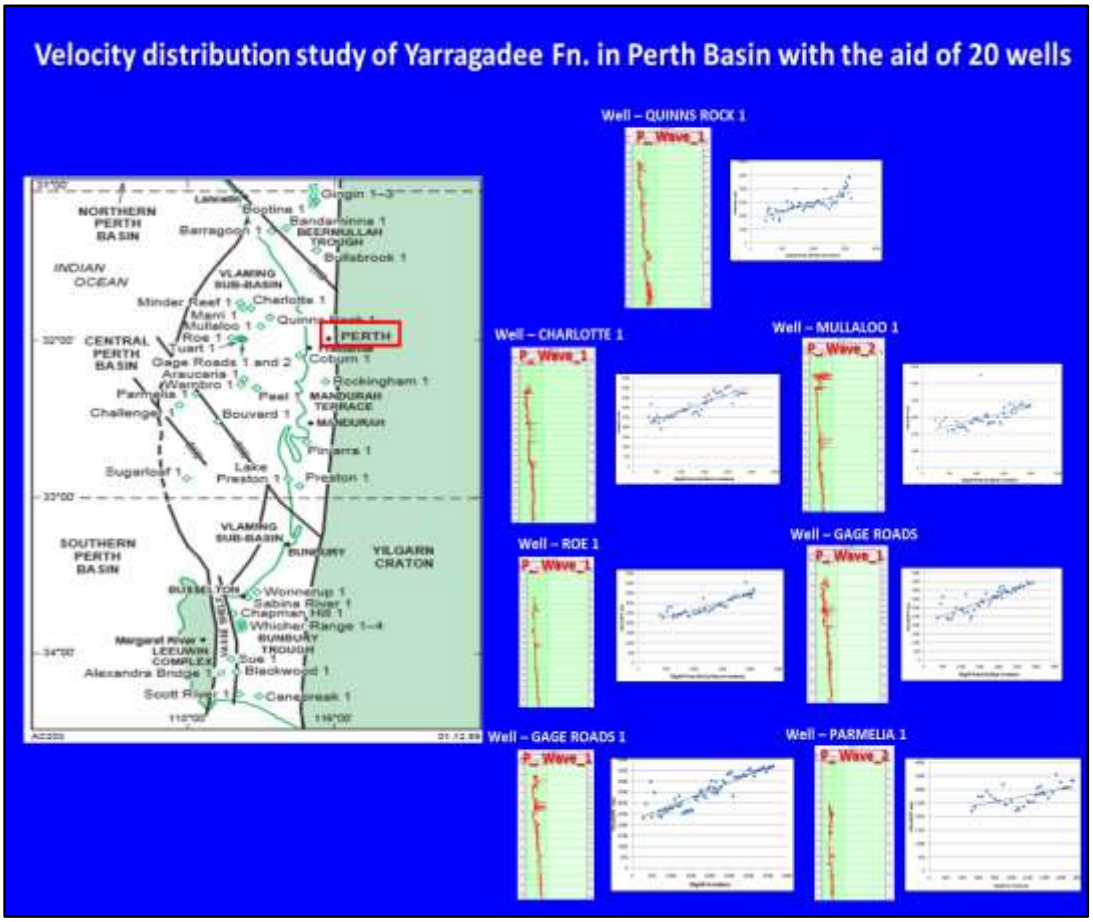

Figure 5.6.2.1: Twenty P-wave well logs in the Perth Basin were chosen to study the distributions of the interval velocities and to build the velocity-depth curves (Crostella and Backhouse, 2000).

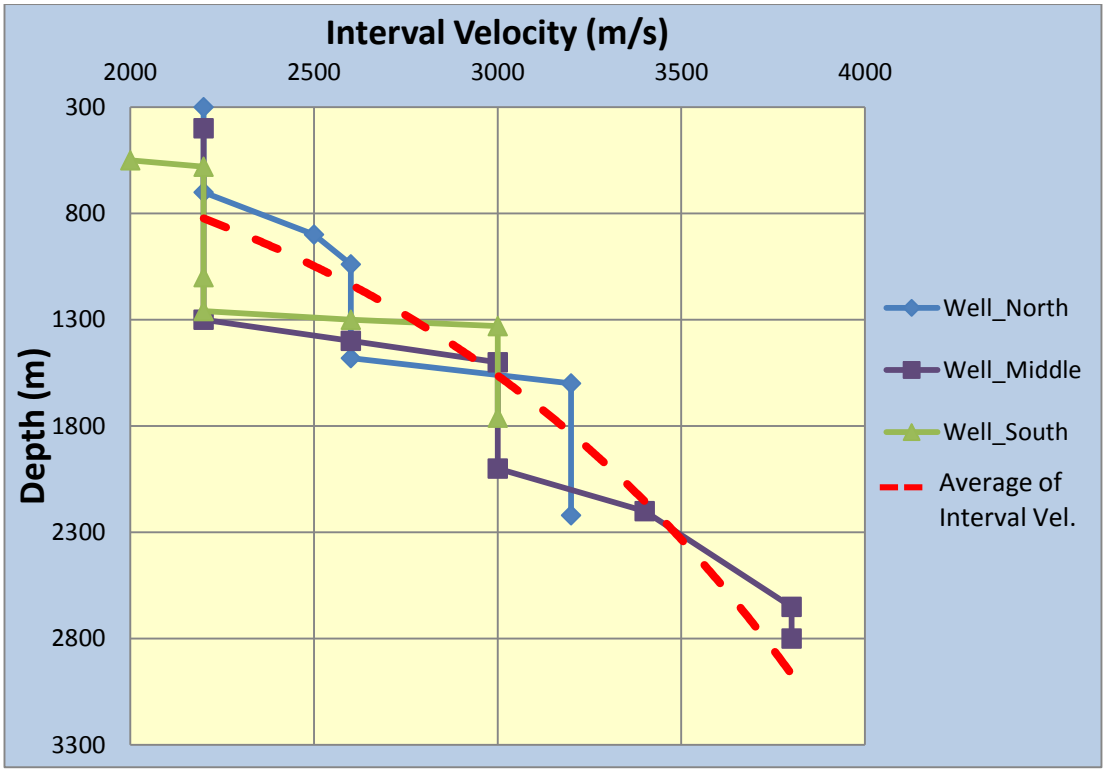

Figure 5.6.2.2: Distributions of interval velocities along the 20 wells in the Perth Basin.

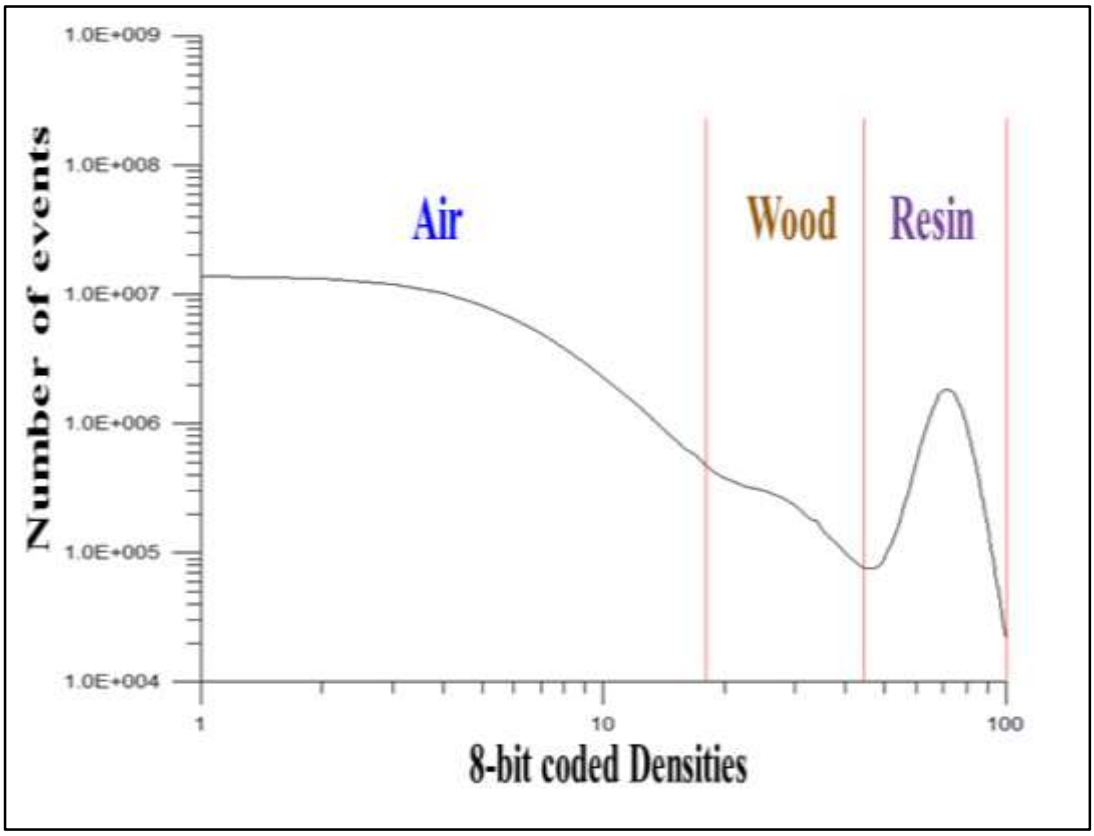

Figure 5.6.2.3: Variation of X-ray signals across the physical model.

5.6.3 Mapping velocities and densities

The X-axis is represented by voxels of 8-bit coded densities and the Y-axis is represented by voxels of velocities. To start building the 3D velocity model, scanning density values had been applied and then remapping them to P-velocities (Figure 5.6.3.1). The actual mapping is fully automated using a stand-alone FORTRAN program.

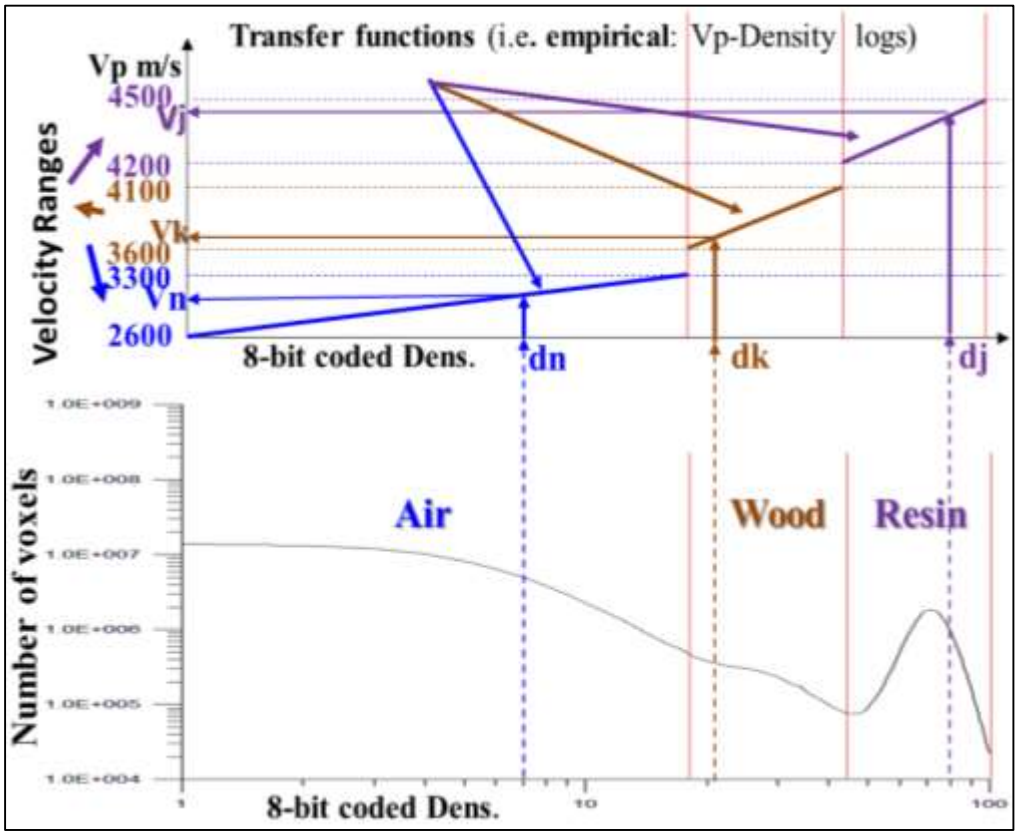

Figure 5.6.3.1: Density-velocity distributions (remapping).

The velocity mapping for the scanned model follows geological velocities (Johnson, 2002), which are averaged from the available logs of the most important units in a depth range. The area within the model occupied by air was assigned velocities ranging from 2600 to 3600 m/s according to the slope in Figure 5.6.3.1. Wood received the velocity range of 3600 to 4100 m/s, while for resins I used somewhat narrower velocity range of 4200 to 4500 m/s.

5.6.4 Numerical model

The Initial selection of the x-ray regions produced a simple cube, which was used for the seismic model (Figure 5.6.4.1). Model parametrisation was adjusted to the available computing resources and, therefore, 442 in-lines and 350 cross-lines were selected. 340 cells in the depth axis (N_Z) were selected. This meant that the initial model size was trimmed by about 30%.

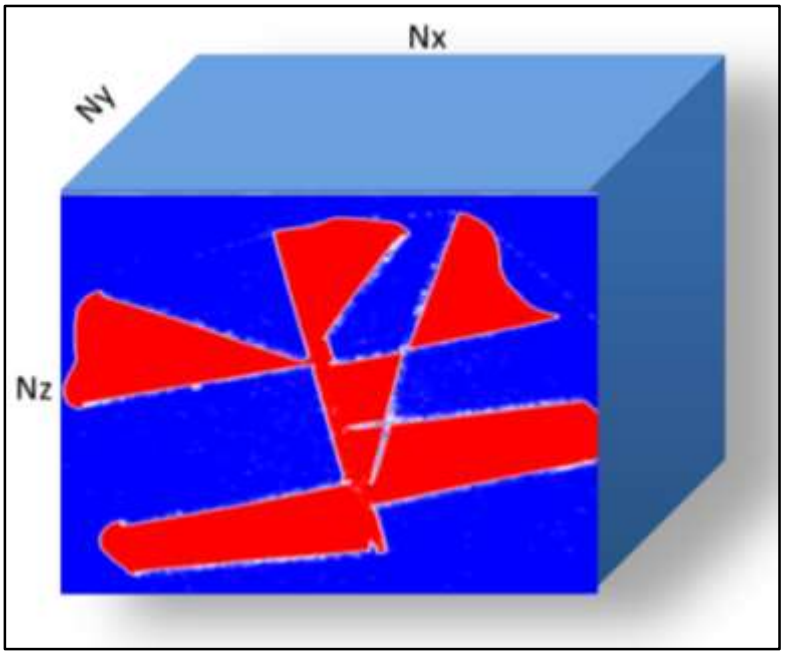

Figure 5.6.4.1: The resulting 3D velocity model

Model parametrisation is shown in Table 5.6.4.1

Axis	Old dimensions	New dimensions After Trimming
Ny	442	221
Nx	768	350
Nz	768	340

Table 5.6.4.1: The dimensions of the 3D velocity model

Automatic assignment of different regions to be populated by chosen elastic parameters significantly cut the model construction time and shortened the procedure

of parameters assignment. The refined velocity model was imported from Drishti (Figure 5.6.4.2) into the proMAX processing software (Landmark graphics, a Halliburton company). A 3D grid was used to define in-lines and cross-lines for post-stack modelling.

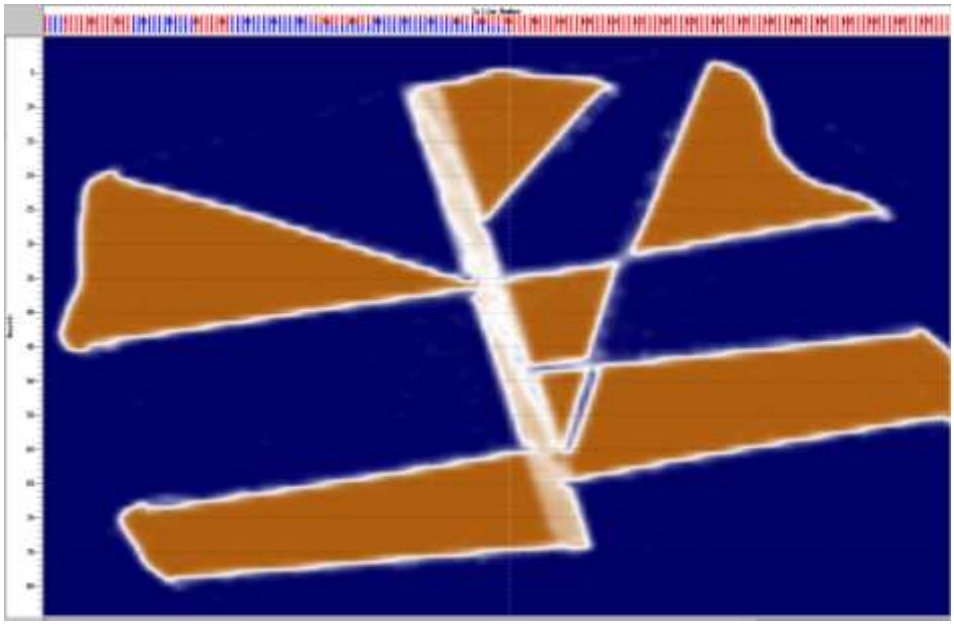

Figure 5.6.4.2: The final image of 3D velocity model imported into ProMAX

5.6.5 3D poststack modelling

For model parametrisations of NY=221, Nx=350, and Nz=340. I selected a uniform grid: DH=dx=dy=dz=7m, that is less prone to numerical dispersion (Mufti et al., 1996). In general, the following rule should be followed to avoid or reduce grid dispersion:

$$H \leq C_{min} / wf_{max}, \qquad (5.6.5.1)$$

Where C_{min} = minimum value of the migration velocity used in the model, f_{max} = maximum frequency in the data to be migrated, w = number of samples per minimum wavelength λ_{min}, given by $\lambda_{min} = C_{min} / f_{max}$

Furthermore, for a selected value of grid spacing, the system becomes numerically more stable when the time sampling satisfies the condition

$\Delta t \leq \mu h / C_{max}$, (5.6.5.2)

Where C_{max} symbolises the maximum value of the migration velocity and μ is a constant. According to Mufti (1996) μ = 0.5 and w = 3.5 are reasonable values for 3D modelling.

The modelling parameters were as follows:

(a) Maximum time: 2500 ms
(b) Sample rate: 0.5 ms
(c) Wavelet central frequency: 20 Hz
(d) Wavelet length: 45 ms

Numerical dispersion and stability have to be considered thoroughly before modelling commences. Stability is controlled by the grid sampling primarily and discrepancy between true and grid velocity. If true velocity (C) $\neq \frac{\Delta h}{\Delta t}$, then different frequencies will propagate with different velocities, resulting in numerical dispersion. Dispersion can be avoided if at least 6 grid points are used to sample the highest frequency. Further improvement is achieved if large velocity contrast and variation are avoided.

Using this, I calculated the critical parameters were calculated as shown in Table 5.6.1. The slowest velocity was 2600 m/s, while the highest velocity in the model was 4339 m/s. This is a significant span in velocities so the grid needs to be adjusted not only to the smallest velocity, but also to the contrast between them. That requires more samples per wavelet and hence a finer spatial sample rate. Subsequently the time sample rate ΔT is selected.

For R, the coefficient of stability; the following equation is used:

$R = V \cdot \Delta T / \Delta H \ < 0.7$,

where V is the maximum velocity, which is this case is 4339 m/s. Thus, in this case the controlling factor (R) is less than 0.31, which is satisfactory.

If the wavelet is well sampled (6 or more points per period) then the grid velocity is not far from the real velocity and we get reasonable results. Once the parameters were selected the actual post-stack modelling took approximately 30 hours. Instead of the common exploding reflector (boundary) modelling of Carcione et al. (2002), the exploding surface model was used. The solutions are not identical, but are very close, while the exploding surface model is easier to implement. Snap shots of the modelled wavefield are shown in Figures from 5.6.5.1 to 5.6.5.5, representing 3D poststack time sections: in-lines, cross-lines and are shown in Figures 5.6.5.2 and 5.6.5.4, and enlarged section area is shown in Figure 5.6.5.3 and 5.6.5.5.

The output was without any numerical dispersion yielding a 3D cube of excellent quality; these results suggest that the same parameters can be used for pre-stack modelling, which much more time is consuming and sensitive to errors.

The generated GNU/FORTRAN application contained parameter files (Appendix B) that were executed and output for parallelisation. A master parameter file (Appendix D) utilised second order finite difference in time and 4^{th} order for space derivatives. It was written and created in a way that it was supplied with the powerful parameter files; log files and the master parameter file (Appendices A to F). This is shown solely to illustrate the main steps taken and the complexities involved in 3D pre-stack modelling.

The main steps are:

- Parameterisation of geometry
- Selection of the numerical parameters (grid size, wavelet type and characteristics such as duration and peak frequency)
- Memory management and parallelisation
- Output grid management
- Data reorganisation
- Conversion to SGY format and porting to processing package

The Parameters	(Description) Information		
Cube dimensions	Ny = 221, Nx= 350, Nz = 340		
Sample rate [us]	500		
Number of samples	5000		
DH	7.0 m		
dx	7m		
dt	0.5 ms		
No of Wavelet samples	45 ms		
W = minimum phase wavelet	Dom. period ~ 45 ms (22 HZ +), are producing satisfactory result in regard to minimal dispersion and temporal resolution.		
Stability Analysis	Vhigh	Rmin = .1857	Rmax .3099 (<.7)
	Velocity	2600.	4339.
	grdPt/W avL	14 >12	31

Table 5.6.5.1: Parameters used for poststack modelling.

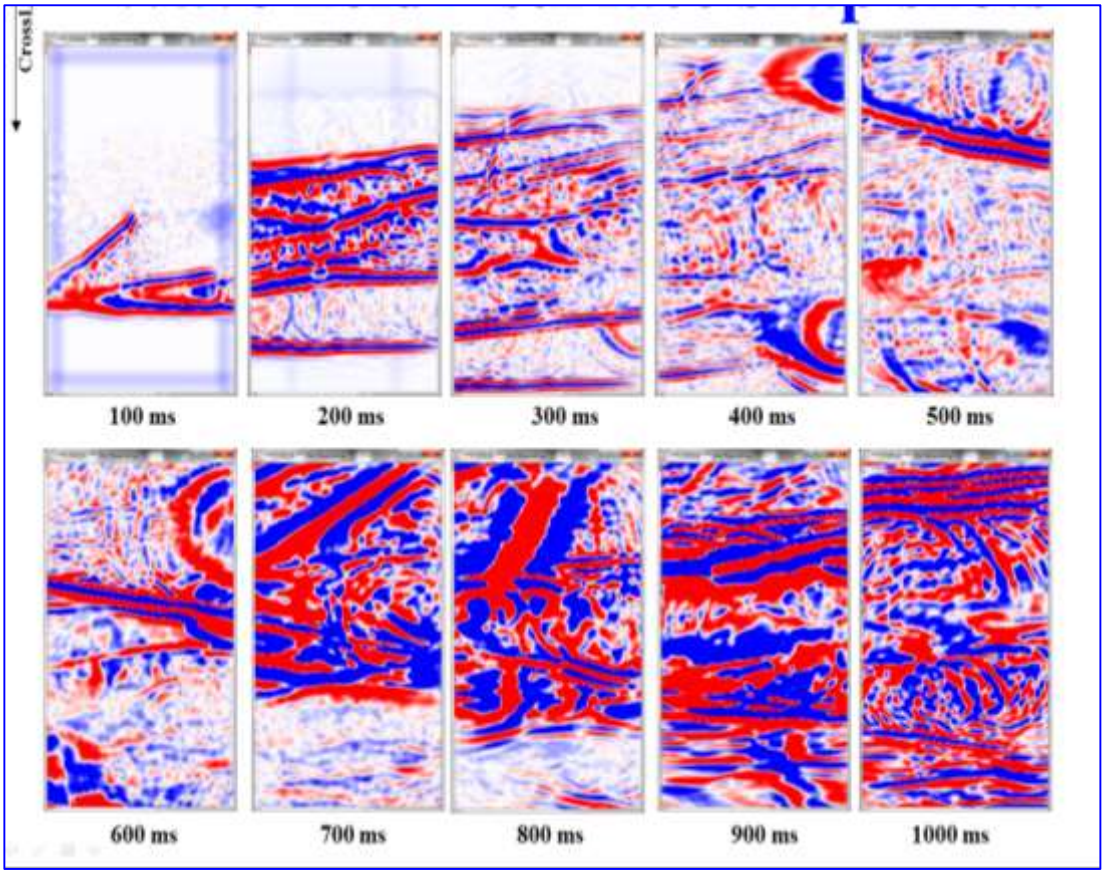

Figure 5.6.5.1: 3D poststack modelling snapshots of the pressure distribution in the model.

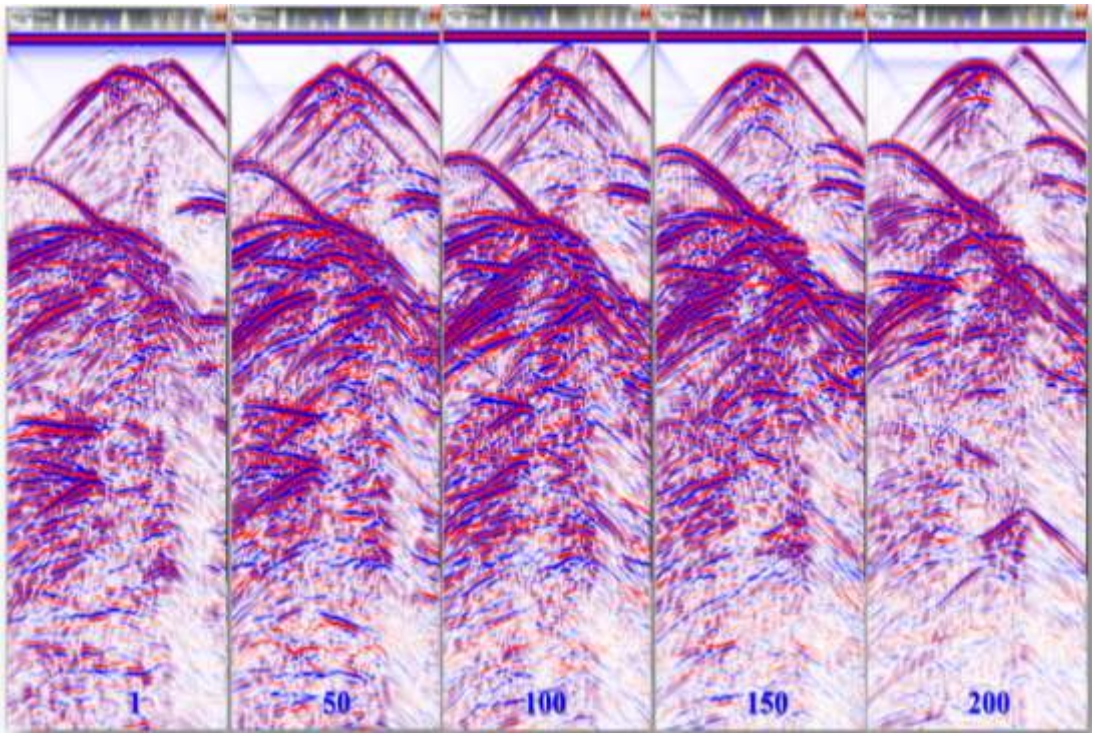

Figure 5.6.5.2: 3D poststack modelling (time sections). In-lines: 1, 50, 100, 150 and 200.

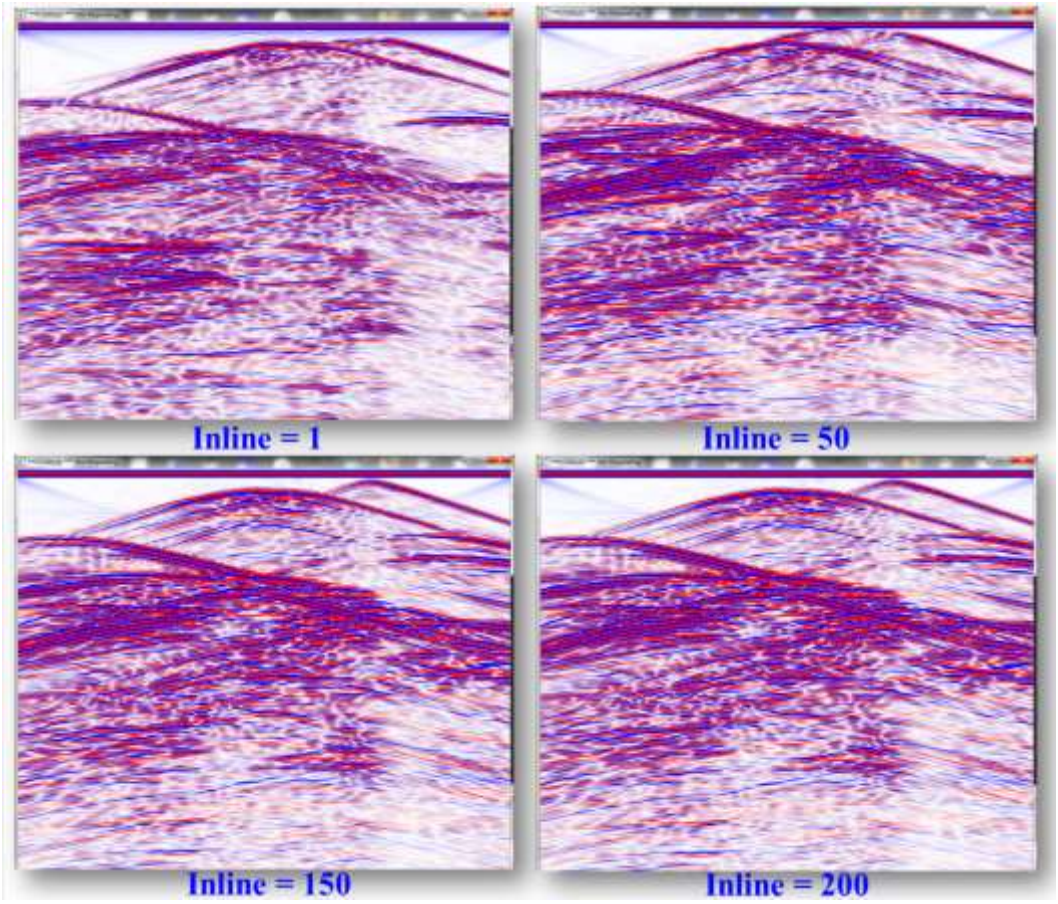

Figure 5.6.5.3: 3D poststack modelling in-lines.

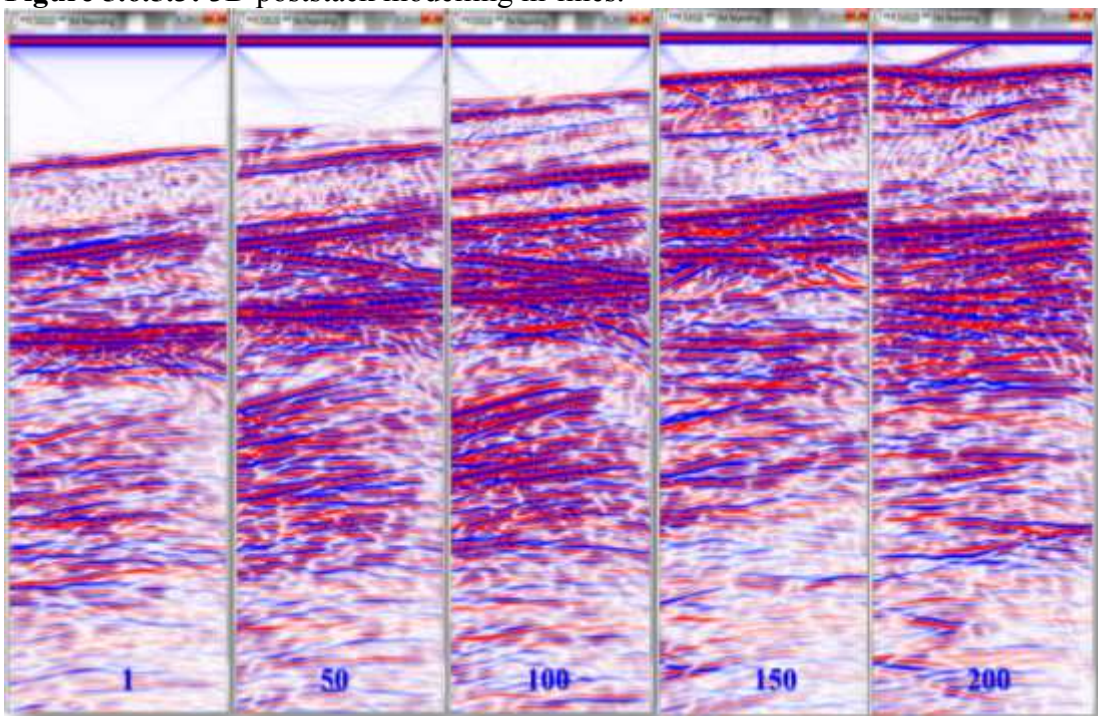

Figure 5.6.5.4: 3D poststack modelling time sections cross-lines: 1, 50, 100, 150, 200, and 300.

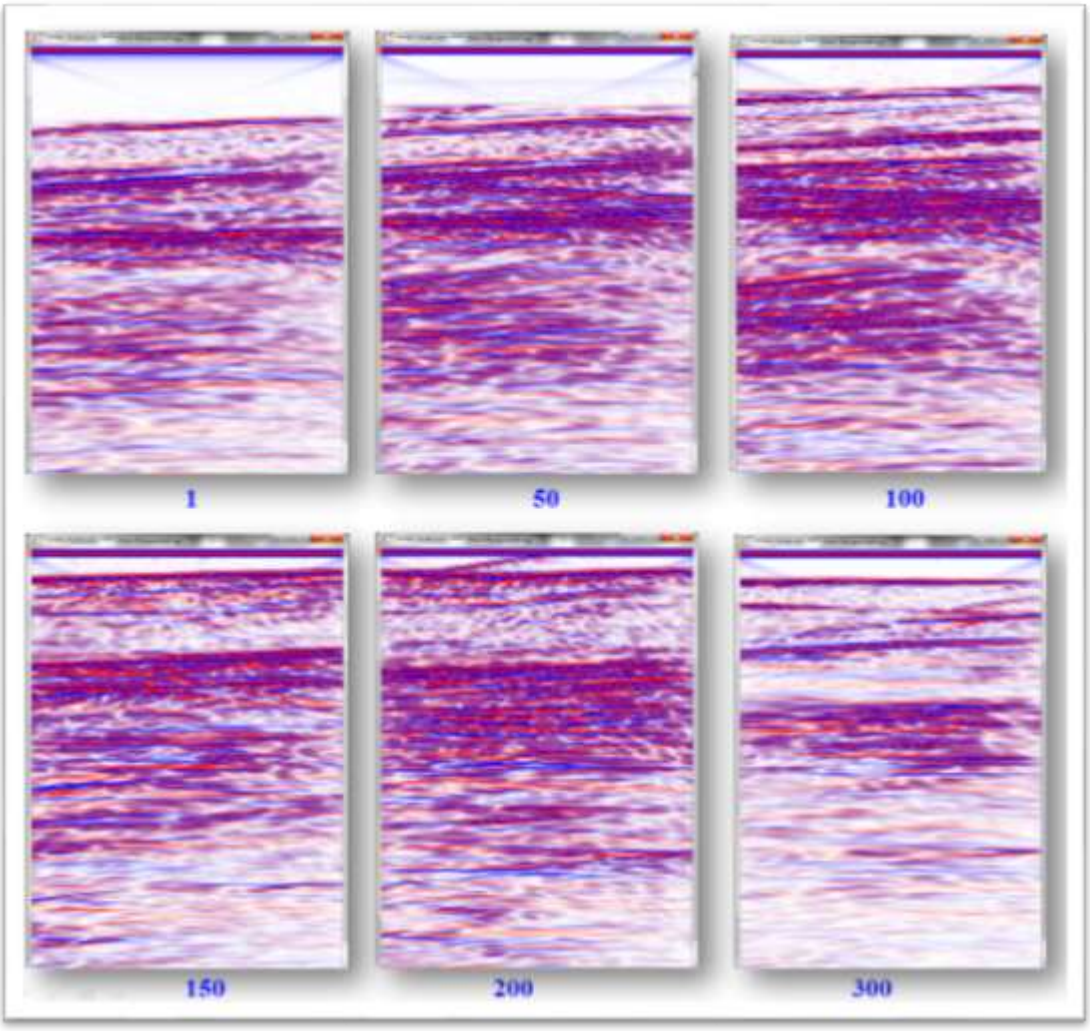

Figure 5.6.5.5: 3D poststack modelling cross-lines: 1, 50,100,150,200 and 300.

In summary, the quality of the images obtained with the 3D post-stack modelling approach was high. It is therefore hoped that the chosen parameters will result in good quality shot records that is non-dispersive shot records.

5.6.6 3D pre stack modelling

One of the first tasks for 3D modelling is to set the receiver and shot lines. The acquisition parameters are given in appendices B, D and E. The grid size again was: DY=221, DX=175 and DZ=170. The recording time was extended to 4000 ms so that large offsets are recorded properly.

The dominant frequency was slightly increased to about 33 Hz (Figure 5.6.61). The minimum phase wavelet was successfully used as it displayed high level of numerical stability in previous simulations. Hence the same wavelet was chosen in the next phase, for the 3D pre stack modelling. The number of grid points per wavelet was increased to 17 to reduce dispersion. Survey geometry included 10 shot lines (SL) and 8 receiver lines (RL).

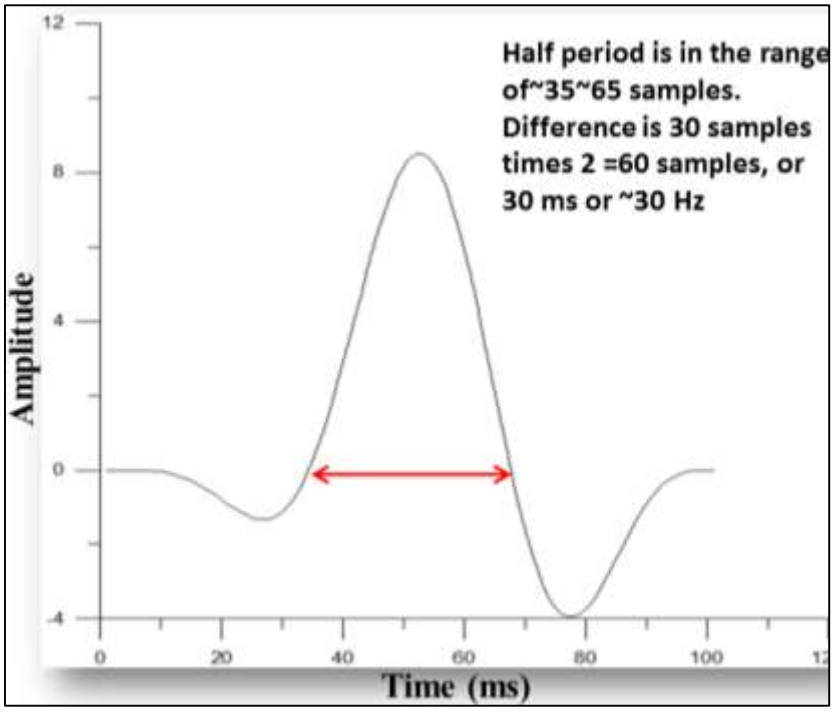

Figure 5.6.6.1: The wavelet used for prestack modelling.

Before discussing resultant shot gathers it should be noted that fully qualifying modelling (recording) geometry, in terms of ProMAX processing software requirements, is essential and not often trivial. Geometry is the most important stage before the data processing can commence. In this case a stand-alone FORTRAN program was used to populate trace headers properly (Dzunic, 2014, personal communication) so that the values could be loaded to the ProMAX data base. For that purpose, geometry information was extracted from the trace headers, and the 3D Geometry module (ProMAX) was used to complete binning (Figure 5.6.6.2). There was a difference between the modelling grid size of 7 x 7 m and the processing bin size of 7 x 3.5 m. While nominal bin size is 3.5 x 3.5 m; the increase in one direction by ½ will effectively double the data fold, which is desirable for later processing stages such as pre-stack imaging.

Shot/receiver lines are displayed in Figure 5.6.6.2 Binned grid and binning parameters are shown in Figure 5.6.6.3. The 3D fold is shown in Figure 5.6.6.4

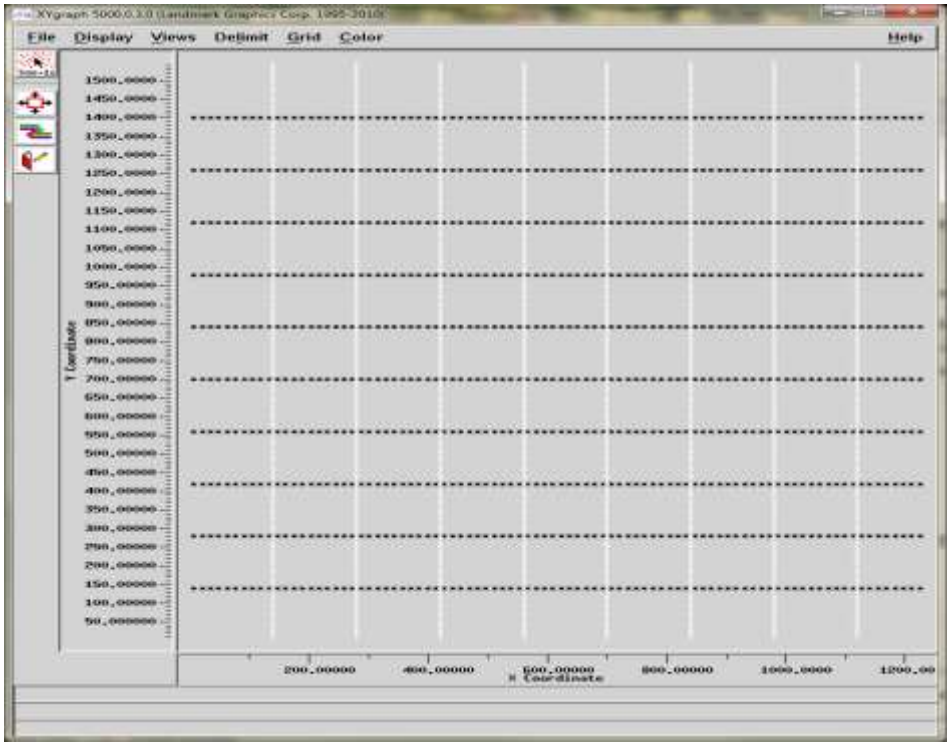

Figure 5.6.6.2: 3-D survey geometry Shot lines shown in black and receiver lines in white.

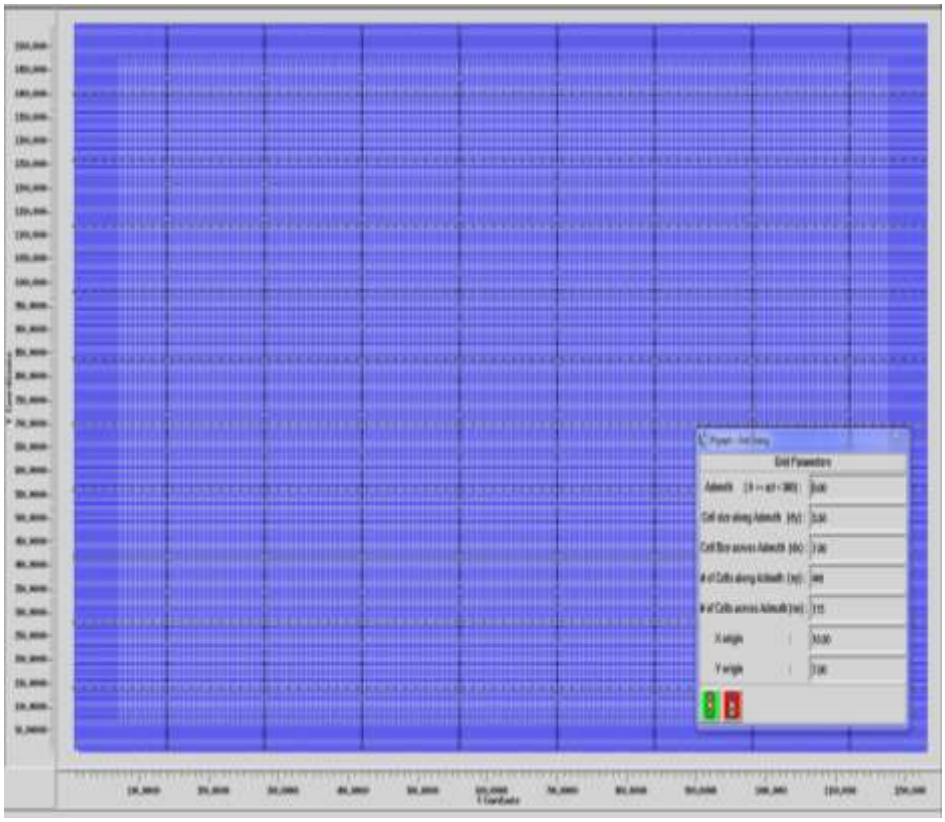

Figure 5.6.6.3: Binning parameters.

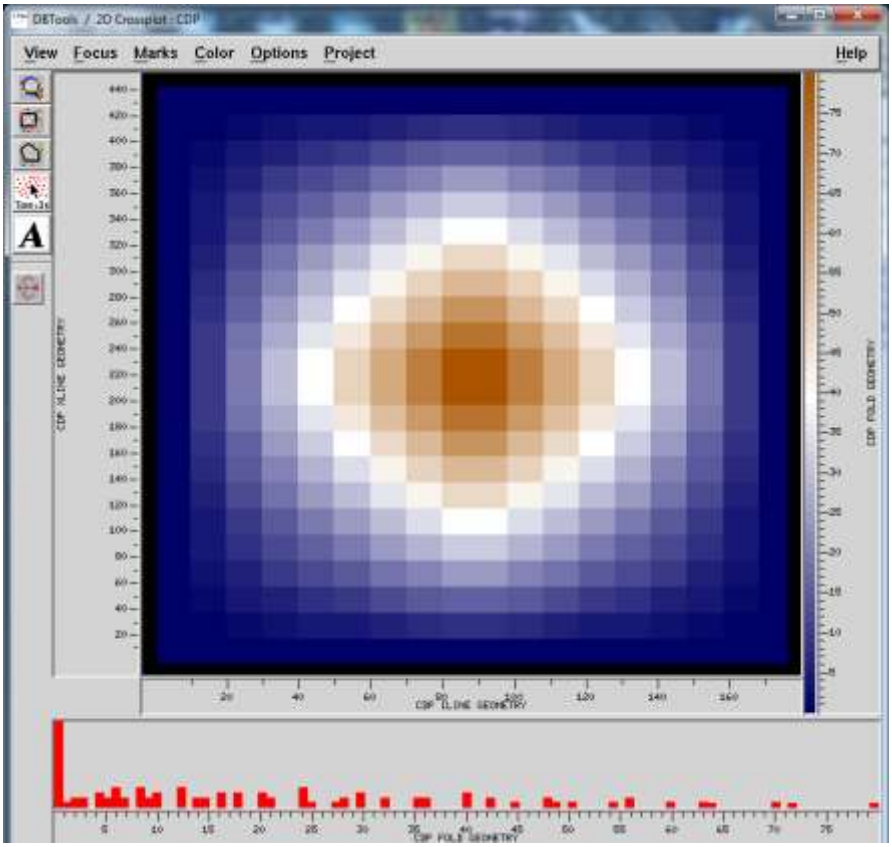

Figure 5.6.6.4: 3-D CDP fold map.

5.7 Results

An example of the 3D shot record is shown in Figure 5.7.1, where a very high quality result was again obtained. Consequently a simple processing flow comprised of AGC, NMO application and stacking produced clear images. Organisation of 3D in-lines, cross-lines and time slices and their relationships are shown in Figure 5.7.2. The resulting brute stack of a selected in-line and migrated stack are illustrated in Figures 5.7.3 and 5.7.4, respectively. The time slices are shown in Figure 5.7.5. In Figures 5.7.6 and 5.7.7, inline 201 was extracted from 3D stacked and migrated cubes, respectively. A "best guess" of the 'flower' structure is presented in Figure 5.7.7. It is clear that interpretation of complex structures is not trivial.

To move the interpretation of the results to the next level, and also to verify the validity of the procedure used from geometry definition to stacking and migration. the resultant seismic image was overlain over the input model in depth domain (Figure 5.7.8). It is now relatively easier to identify the flower structure, but it is also clear

that the data density and the processing need to be improved in order to produce a more interpretable image.

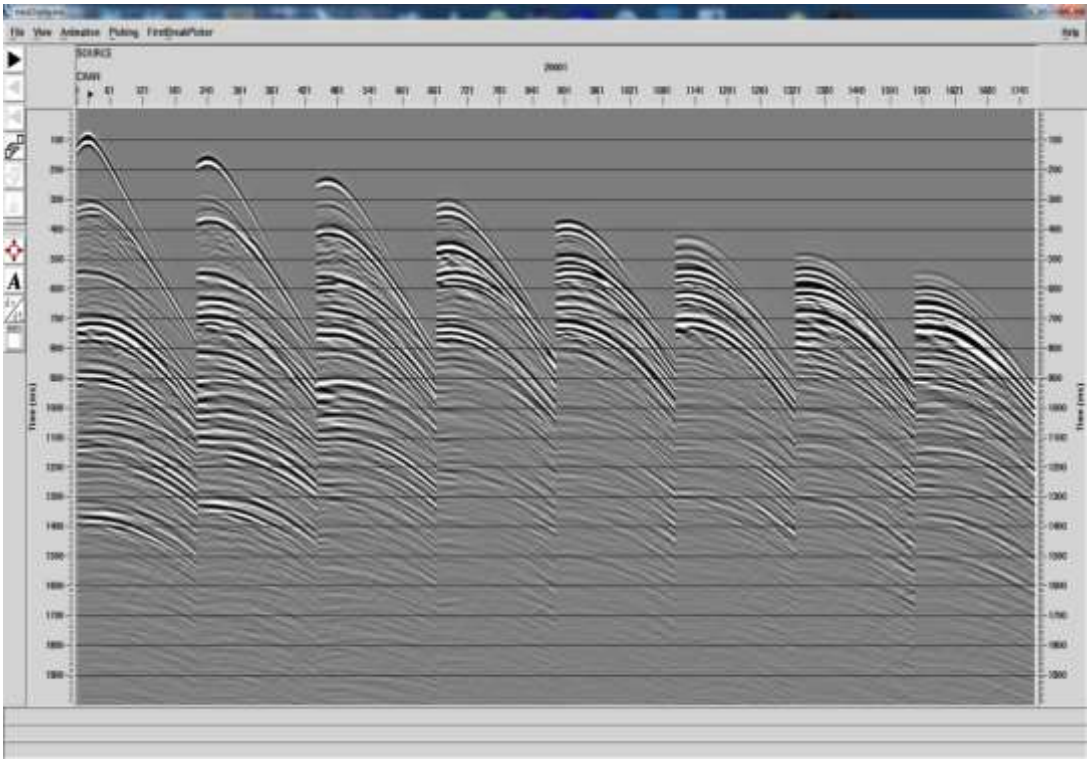

Figure 5.7.1: 3D shot gathering (8 receiver lines).

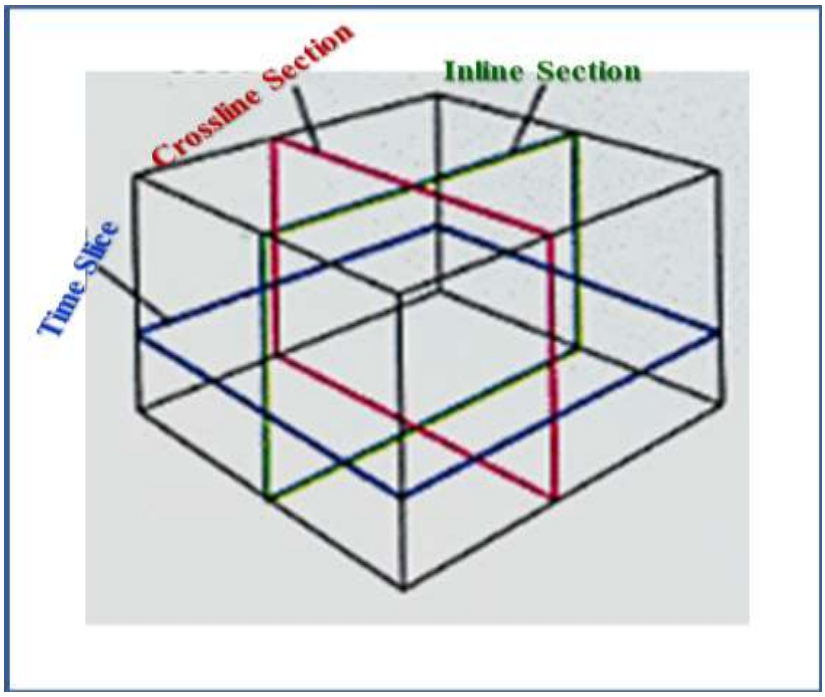

Figure 5.7.2: Crosslines, inlines and time slices, through the 3D Cube is conventionally used to analyse processed data.

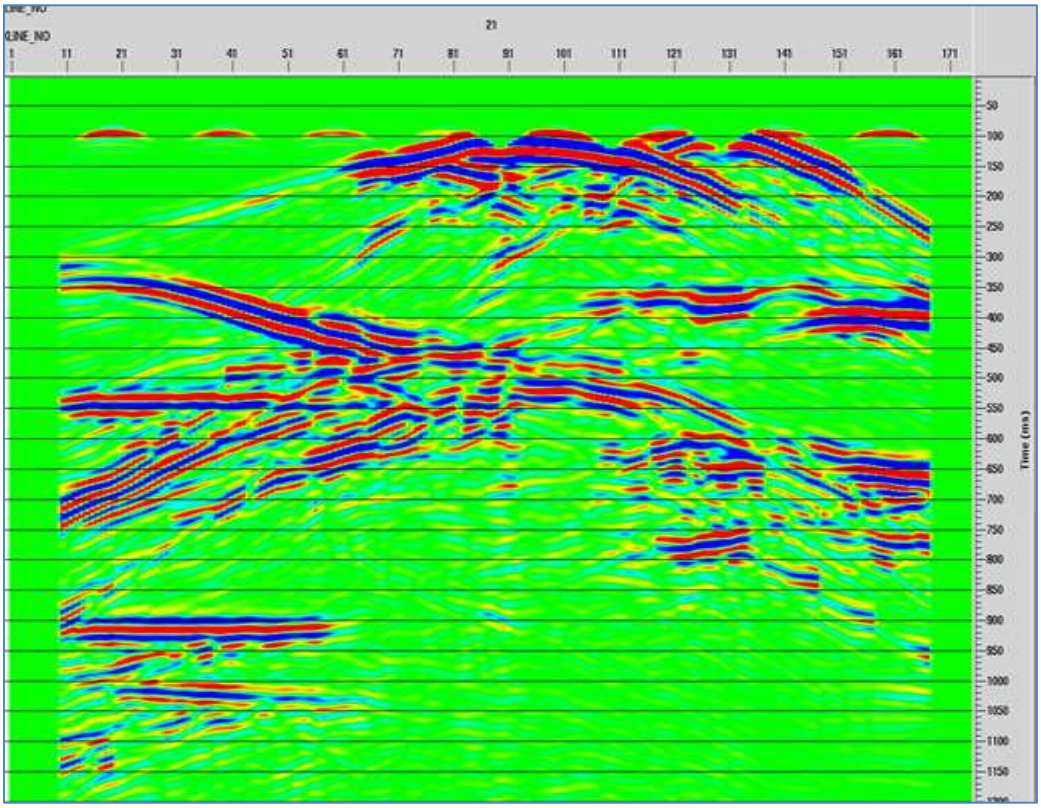

Figure 5.7.3: In-line 21 extracted from 3D brute stack cube.

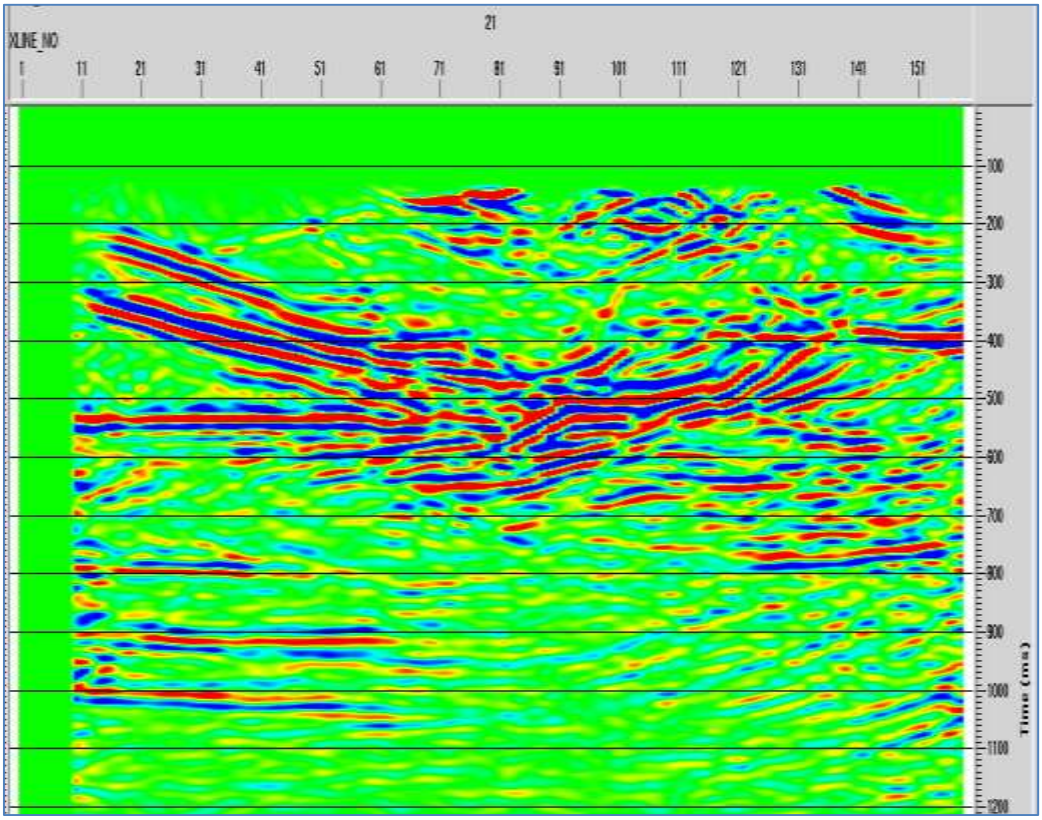

Figure 5.7.4: In-line 21 extracted from 3D migrated stack cube.

As with the 3D Model used, there were 1–441 in-lines (Receivers) and 1–175 cross-lines (Sources) and FFID (1–880) shots (Figure 5.7.4).

The time slices of the 3D post stack migration are shown in Figure 5.7.5 within a range of 200-1200 ms (step 200 ms), Duff (1989).

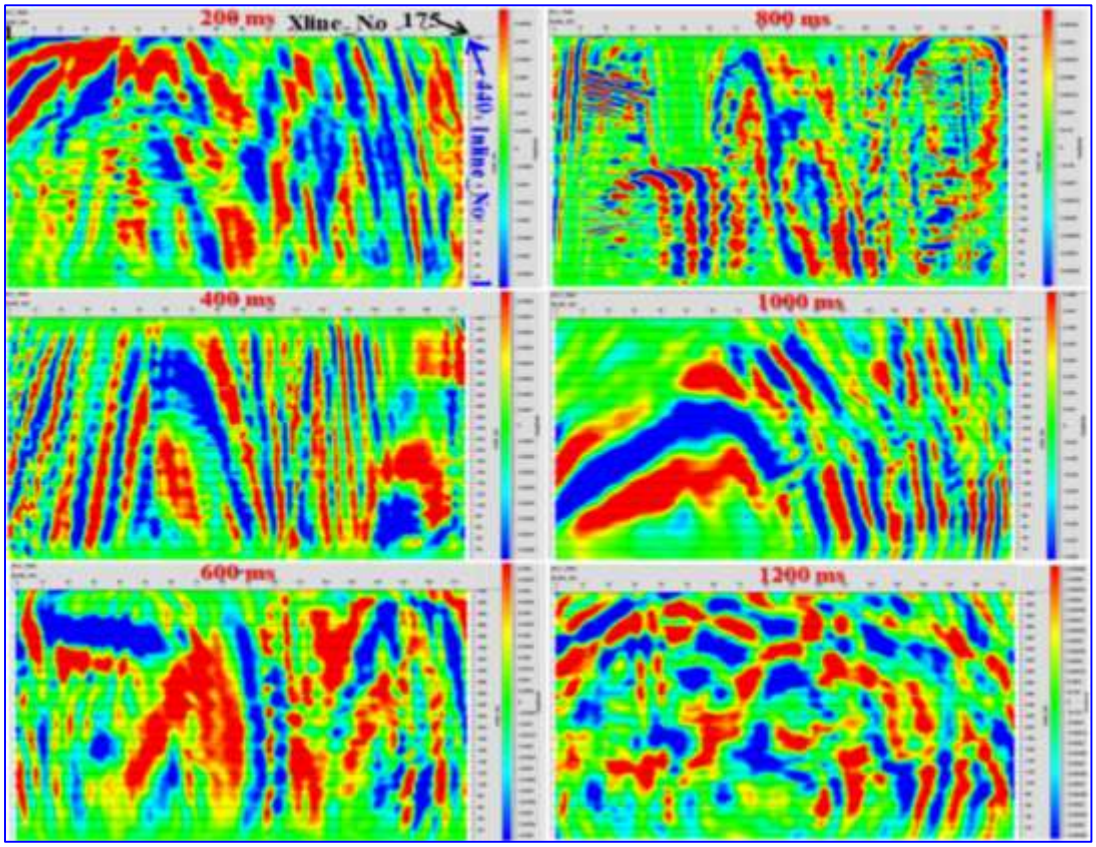

Figure 5.7.5: Time slices in the range 200–1200 ms, with a 200 ms increment.

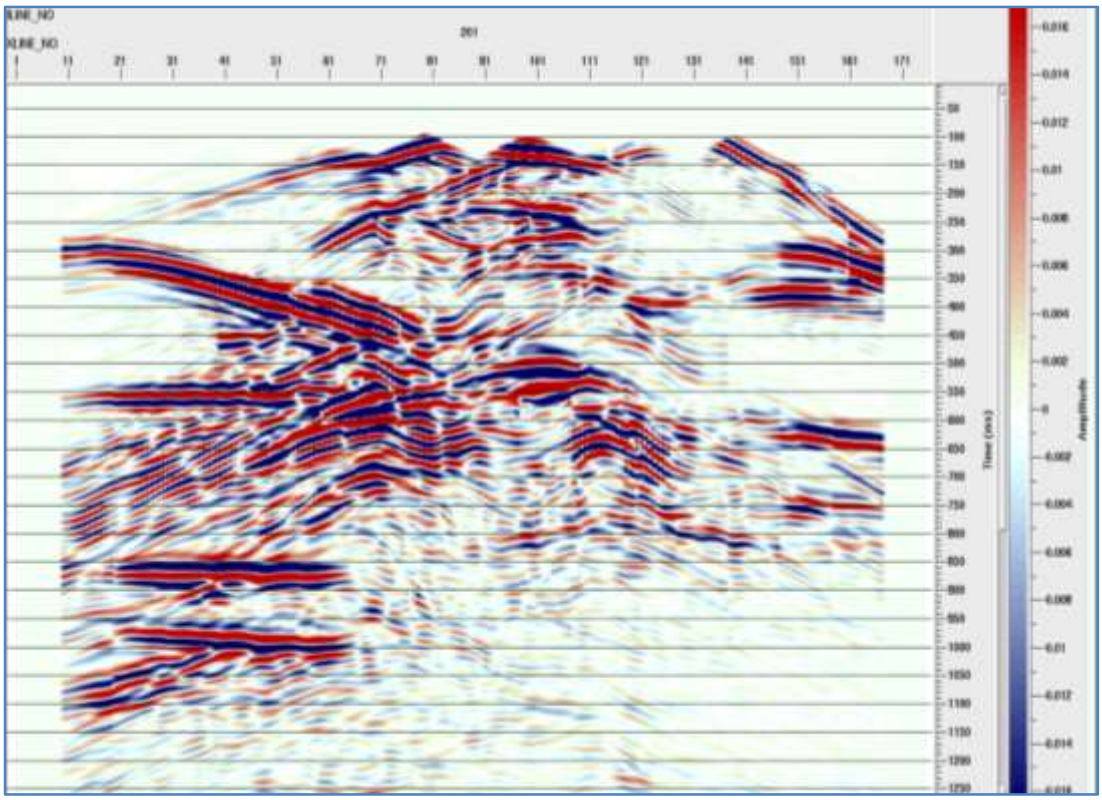

Figure 5.7.6: 3D stacked time section in-line 201.

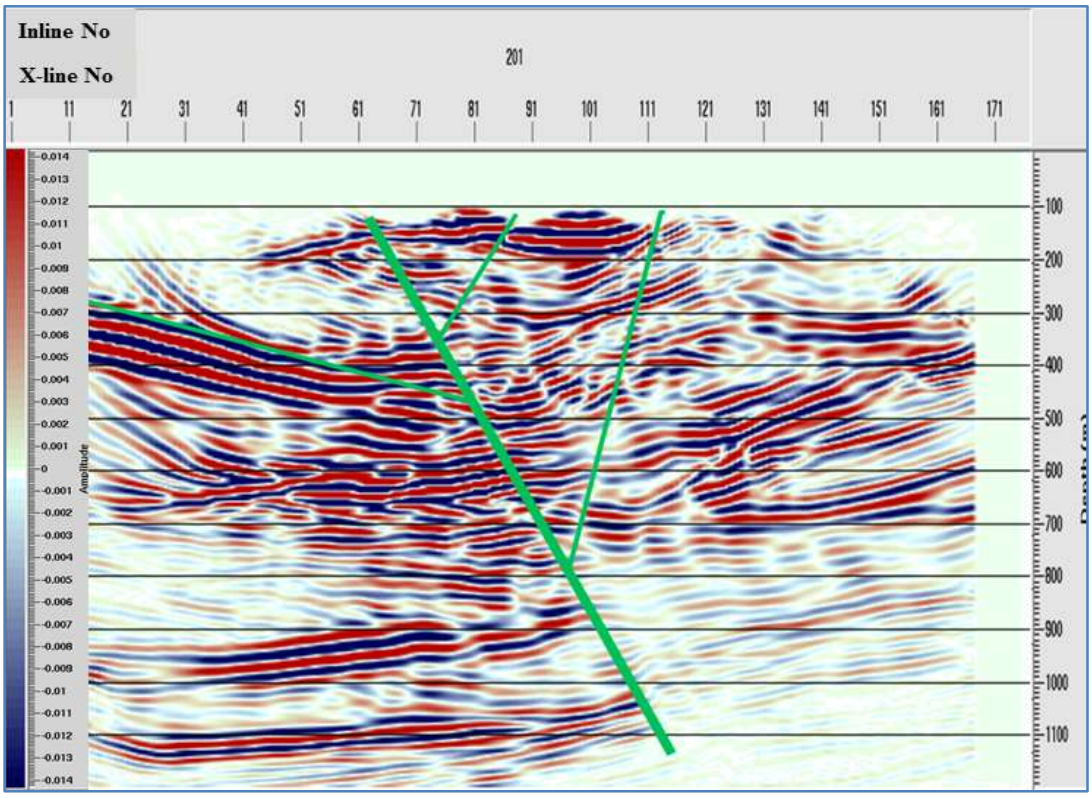

Figure 5.7.7: 3D migrated depth section in-line 201, where the 'flower' structure is viewed in its final profile.

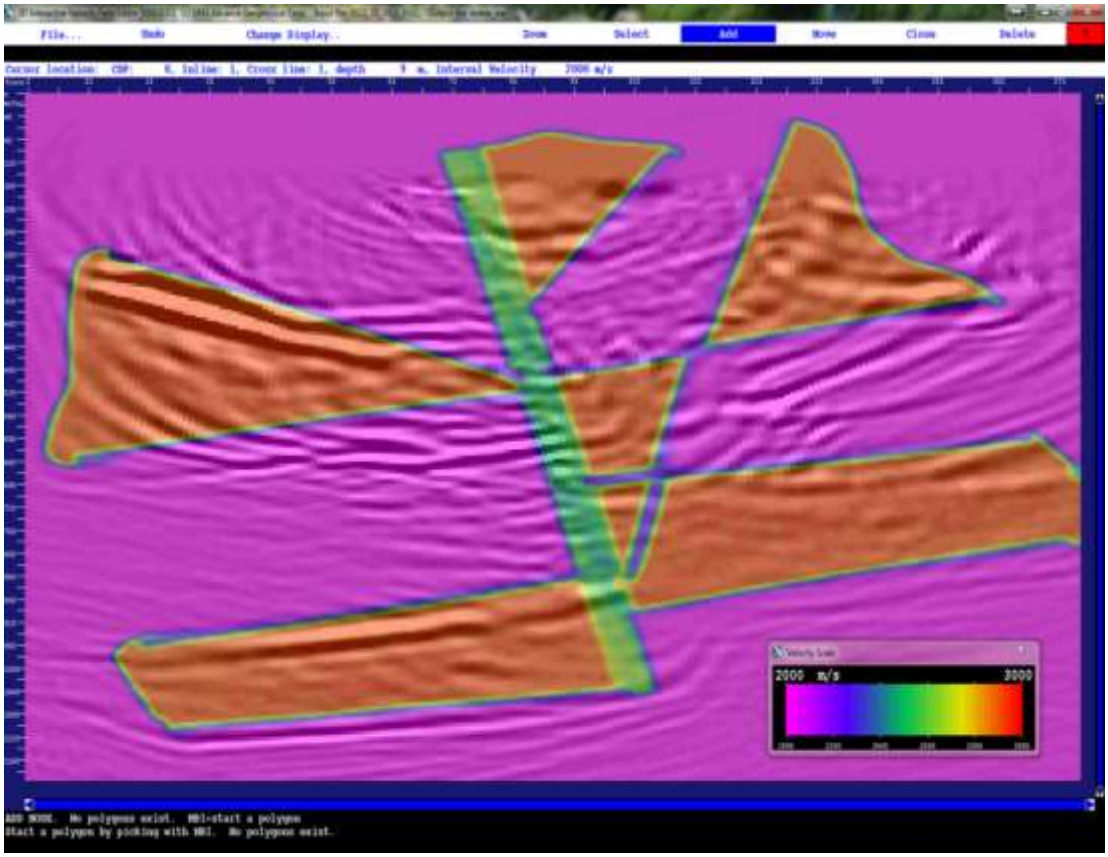

Figure 5.7.8: The seismic-migrated image with the modelling velocity field overlaid in the depth domain.

Chapter 6: Complex structures in the presence of noise

6.1 Introduction

Raw seismic data are often dominated by different types of noise (Bormann, 2013). Common types of disturbances fall into the category of so-called ambient noise, such as wind, rain, traffic, domestic farm animals, power lines, airplanes and so on (Novotny, 1999). The other type of noise is categorised as coherent noise (Newman, 1996), which is created by seismic sources and is, therefore, referred as source-generated noise. Coherent noise (White, 1984; Wentworth, 1989) mostly includes air waves and ground roll (Kummer, 2012). Other coherent events considered as noise in a reflection experiment include P-waves and converted shear head waves, multiple reflections of all orders, refracted reflections and reflected refractions.

Ambient noise can be generated by many sources and is often regarded as random (McNamara, 2004; Shapiro, 2005; McNamara, 2004; Schimmel, 2011; Murugan, 2012). However, the majority of this type of noise is in fact organised in some way, and is therefore also somewhat coherent. Both coherent and ambient noise (Yang, 2008) can significantly affect seismic data quality and must be considered in the seismic survey design. For example, to overcome high levels of noise requires energetic seismic sources, high fold and finer receiver spacing. This substantially raises the costs of the application of seismic methods. Even with the most careful seismic acquisition design, some noise will remain present in the seismic data. Remnant noise can create issues in processing, and subsequently, in interpretation. For example, otherwise continuous reflections can be intercepted by remnant, organised (coherent) noise. Such response can be misinterpreted as, for example, fracture swarm or complex fault zones. It is therefore important to understand the potentially harmful effect of the noise and attenuate it with appropriate processing procedures.

It should be also mentioned that a third type of noise is instrument-generated. However, in most of the seismic recordings, the instrument noise level is several orders of magnitudes below the other so-called seismic noise (Holcomb, 1989). It is clear that all types of noise have to be attenuated or eliminated with the appropriate choice

of seismic processing steps. Only then can seismic interpretation be accomplished with high degree of confidence.

Therefore, to make our 3D synthetic model (as presented in Chapter 5) to closer resemble an actual field situation, it is necessary to include different types of noise so that the reliability of the seismic interpretation of complex faults can be estimated. It is usually the case that the 3D seismic images are clearer than the corresponding 2D images. This can be attributed to the higher quality object illumination, which is achieved through the use of 3D seismic as well as the power of 3D processing algorithms (Urosevic, 2014, personal communication). However, some remnant noise is often observed, even in 3D land-seismic images, therefore it is required to include this noise in the resulted synthetic seismic response and use it in the objectives of this study. Moreover, we need to simulate the so-called remnant noise, that is, the noise that remains after the application of various noise attenuation techniques (Henley, 1999, 2003, 2011). This is indeed the most common situation occurring in real seismic data.

6.2 Objectives

In this chapter, two main tasks need to be completed before the interpretation stage: a) the introduction of realistic noise trains, and b) attenuation of the noise through processing and imaging (Cupillard, 2011). Some remnant noise is expected to remain in the data after processing. Different types of noise can be introduced into the synthetic data. Shot-generated noise, for example, emerges naturally from the elastic wave solution. If we are using the acoustic wave equation, which is more common approach, then this type of the noise will have to be introduced later in the process, after numerical simulation is completed.

The noise has to then be attenuated with selected seismic algorithms (Stein, 2007). One of the ways to remove the noise from the data is based on velocity, which is done through measuring coherent noise at a particular velocity or set of velocities (Dingus, 2010). Another way is by using a common process called the 'F-K filter' (Bekara, 2009). It should be noted that the application of the F-K filter, often creates artefacts Calvert, 2003, which may influence the interpretation process (Castro, 2007). Another familiar way to improve the signal quality is via high-frequency enrichment,

which can improve data frequencies without a corresponding increase in noise. This will produce an outcome resulting in a larger bandwidth seismic section with a much higher data frequency than that accompanying conventional seismic (Kumar et al, 2008).

The first step is to identify and analyse the raw seismic data and determine the noise type, its spectral characteristics and its origin. Only then a test can be applied using the required attenuation techniques.

6.3 Noise analysis from field data

Forward modelling of the seismic response needs to be related to the actual field conditions. Only then the modelling results can be used for the analysis of exploration issues specific to the area under investigation. Hence, it is first necessary to analyse seismic noise in the existing field records that are acquired over the area of interest for this study. This may tolerate to add the same type of noise to the synthetic data as is found in the field data. For that purpose, I analysed several field records. One such record is shown in Figure 6.3.1.

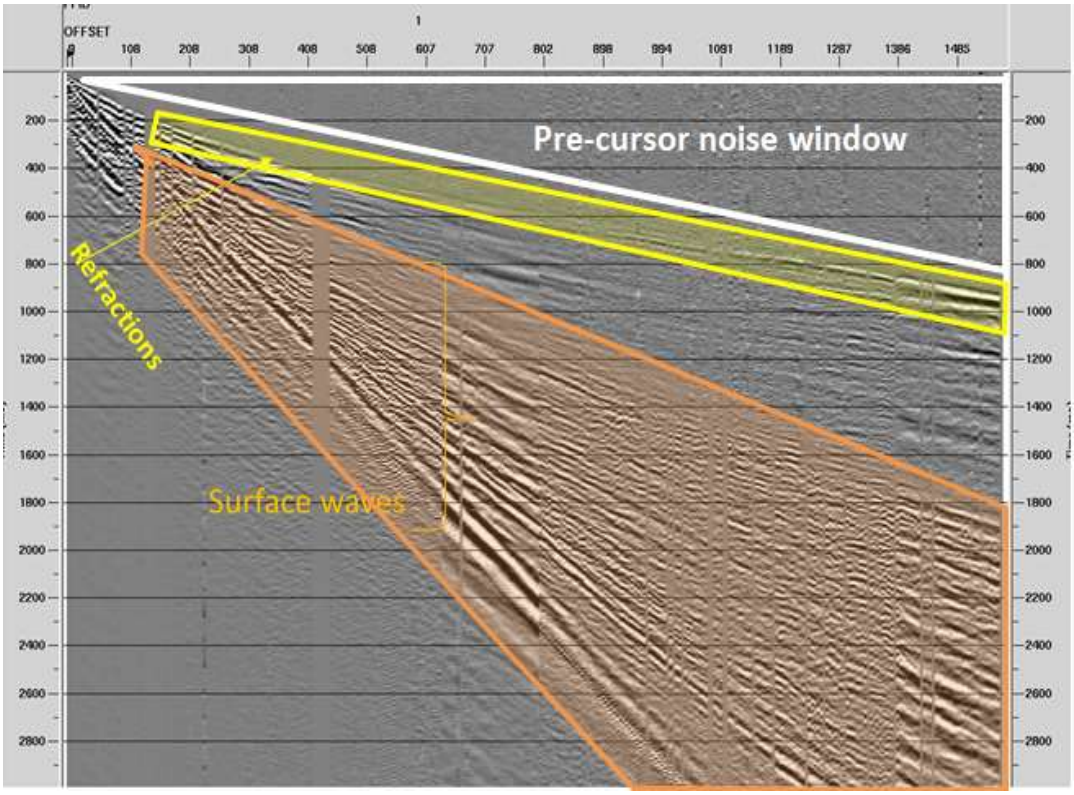

Figure 6.3.1: Selected field record from 2D seismic data acquired (time ms) over the Gnangara Mound. Refractions are marked by the yellow arrow while the area occupied

by surface waves is highlighted in orange. The precursor noise window (white triangle) represents ambient noise at the time of the recording (Bensen, 2007).

Measuring the field data is to establish the study of energy of the ambient noise; direct, refracted as well as surface waves in order to be used within the model (Peterson, 1993) (see figure 6.3.1). This is because in noisy environment, it is hard to see reflections from the target (source) but only coherent noise, first arrivals and ambient noise.

The precursor window is used to analyse the background noise properties (Figure 6.3.2). The different noise sources are labelled. The average noise intensity is estimated to be within an offset range of ±1000 m; refracted waves are then analysed and their intensity estimated (Figure 6.3.3).

In Figure 6.3.2, in the red colored ellipse, the near offset ambient noise produced is mostly by effect of vehicles or weight rather than winds (Machine or vehicle noise). Average ambient noise level is measured in the below window from zero at that moment when the ambient noise was taking place and could be when it was raining or windy or because of the effect of traffic or nearby machines working (factories), which has certain levels of noise. The reason why noise is so high in the vicinity of zero-offset, actually ± 200 is most likely because of the effect of the sources that creates the seismic waves.

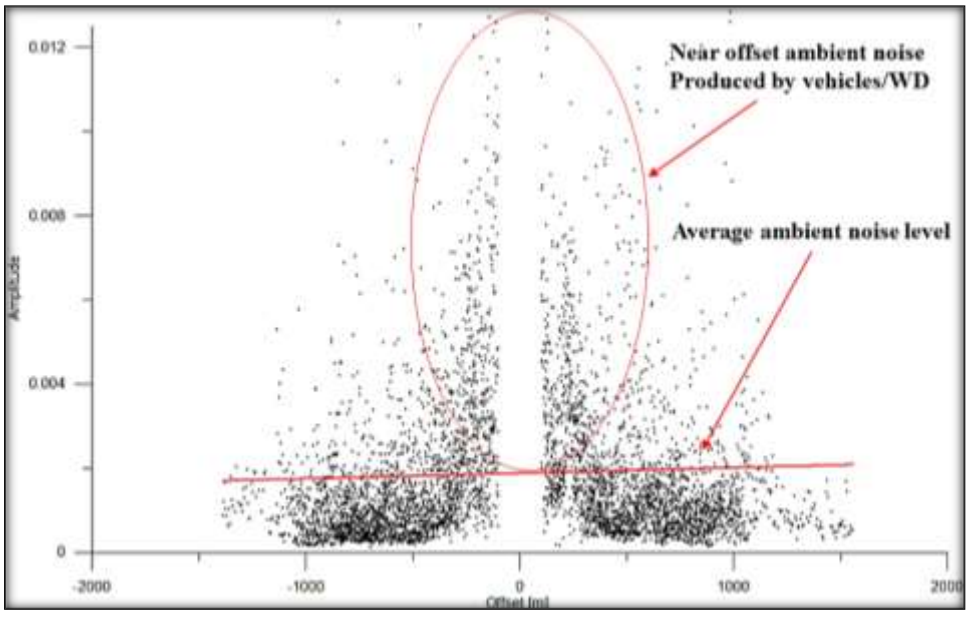

Figure 6.3.2: The ambient noise level as a function of offset. Linear fit can be used to estimate a range of the ambient noise as well as its average intensity.

Figure 6.3.3 is similar to Figure 6.3.2, represents the amplitude of the first arrival of the refracted waves.

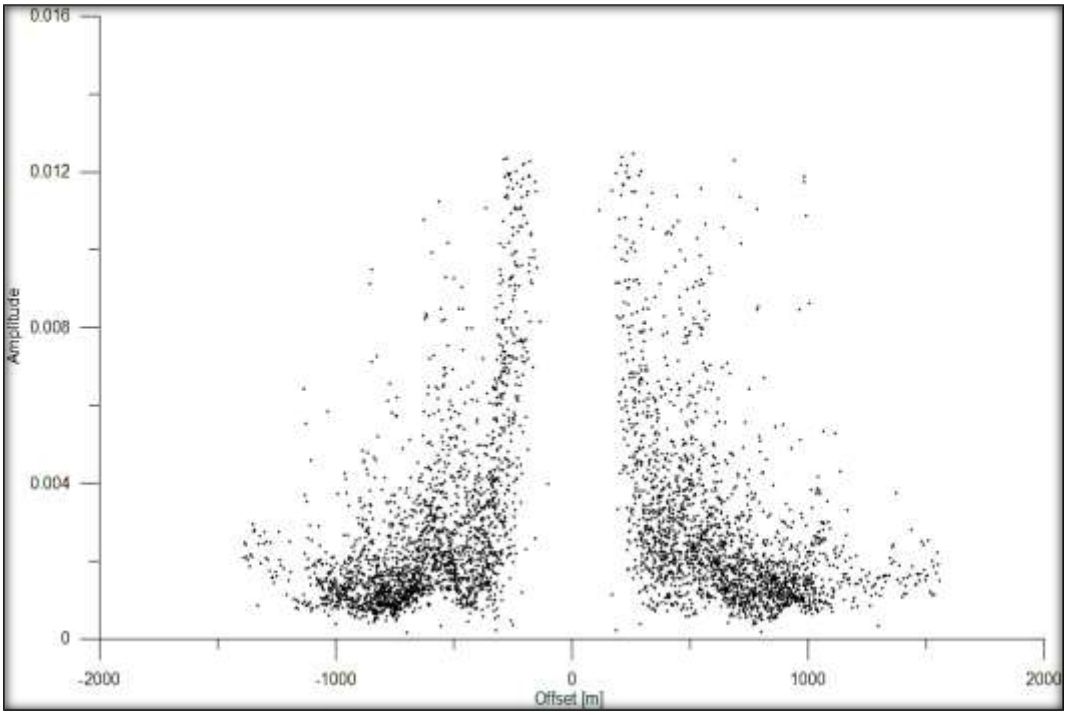

Figure 6.3.3: Refraction wave amplitude verses offset. These waves display moderate energy level.

The three figures 6.3.2, 6.3.3 and 6.3.4, indicate that the surface wave intensity is the highest while refractions are just above the ambient noise on moderate to far offsets, as expected.

The figures 6.3.2, 6.3.3, and 6.3.4 represent amplitude of the traces as a function of the offset for ambient noise (as seen in Figure 6.3.1 above the white colored triangle, the second strip is the yellow colored window that covers the refracted waves, and the orange strip that covers the surface waves)

Surface waves are analysed in a window limited to their presence. The intensity in the offset plane is shown in Figure 6.3.4.

Figure 6.3.4 shows the amplitude distribution verses offset in the window that covers the surface waves (as indicated by the orange colored strip in Figure 6.3.1), which depicts maximum value. The reason why this was measured, because acquiring those amplitudes on the representative shots that gives the amplitude of the important

features dealt with; ambient noise, direct waves, refracted waves (Colburn, 1986) and surface waves.

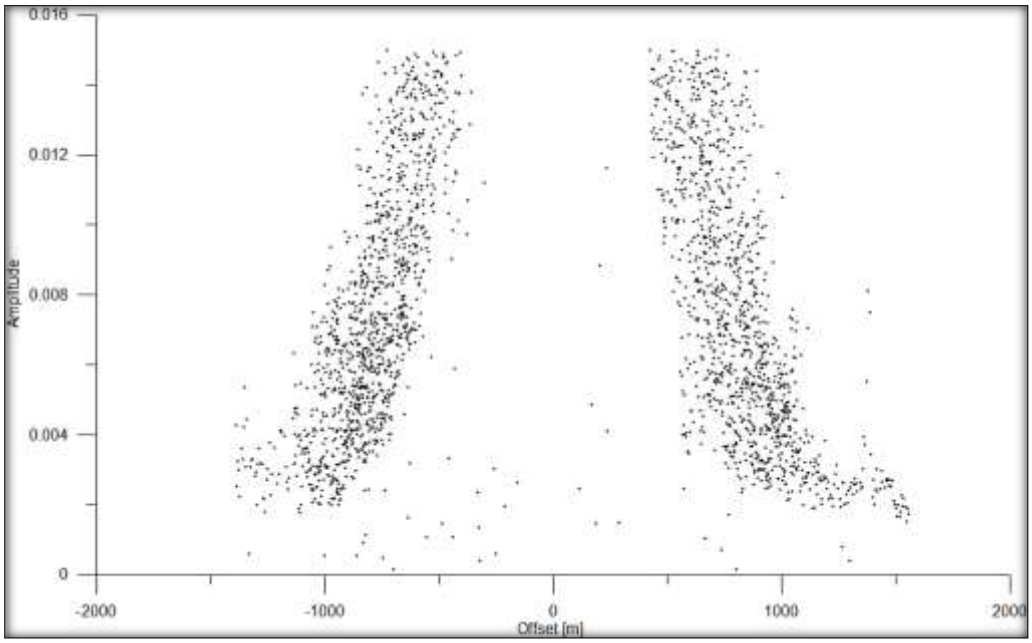

Figure 6.3.4: Surface wave energy along the offset plane. These waves display the highest energy level.

The energy of different events can be better visualised through computations of their ratios. The ratio of refracted/ambient noise is displayed in Figure 6.3.5.

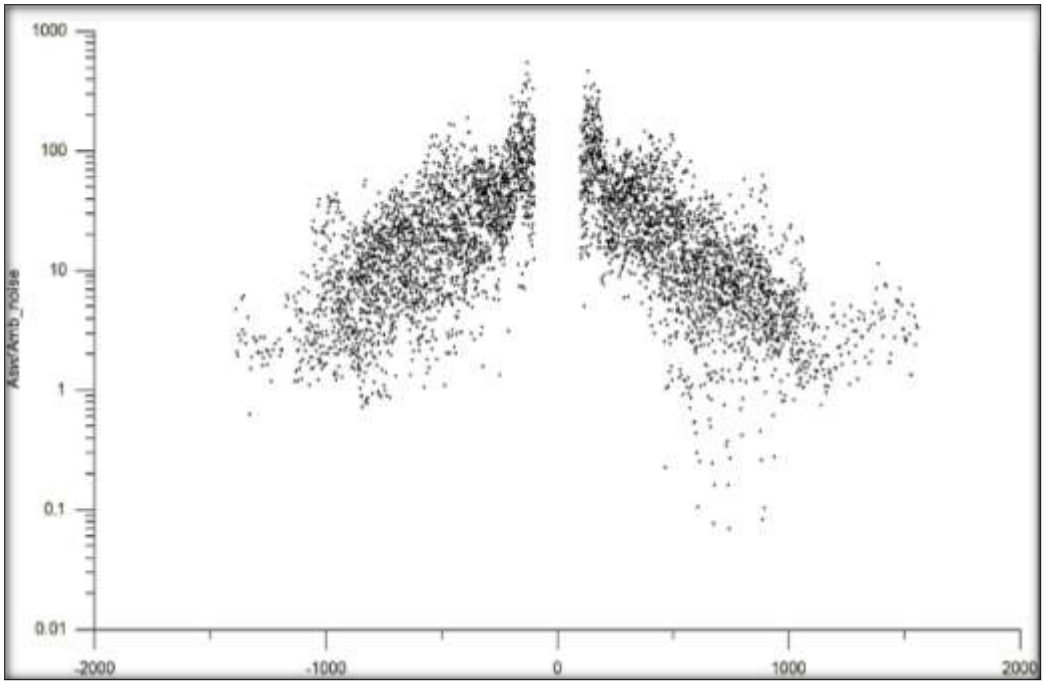

Figure 6.3.5: Amplitude of refracted waves compared to ambient noise amplitude.

Figure 6.3.5 shows the ratio of the amplitude of the refracted waves to amplitude of ambient noise. The vertical axis is Logarithmic to produce a god insight of the ratio. This is important because for with the used model, there was a need to provide certain levels of noise that has a parallel impact as with that ratio in the field.

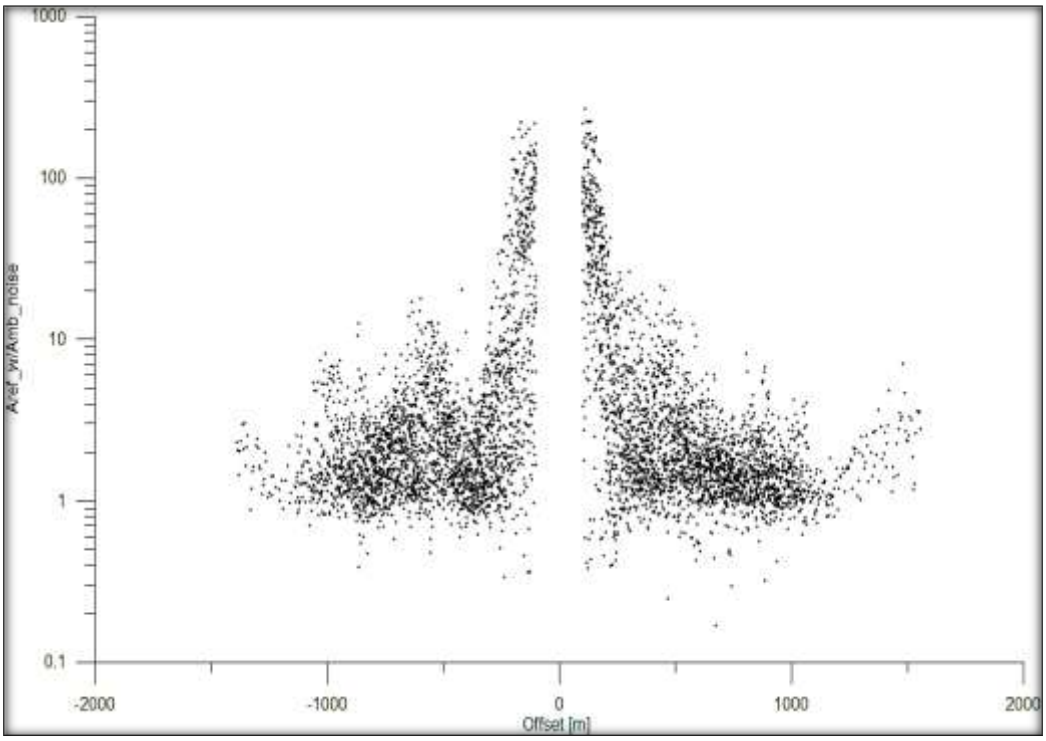

Figure 6.3.6: Amplitude ratio: surface wave/ambient noise.

There was a need to stablish how much amplitude or energy of surface waves must be added on top of our model to get a model data. A certain level of noise data (ambient noise) was added add then surface wave with certain amplitudes. But these amplitudes must follow ratio that is not measured in the field, that's the main idea. Figure 6.3.6 indicates the Amplitude ratio of surface wave to ambient noise.

Figure 6.3.7 shows that surface waves at the close offset are much smaller by amplitude compared to direct wave, and that is because when exploding was done the P-waves were first created which goes up very high and goes down then died out quickly very fast but when the offset at 300 meters, surface waves became much more stronger than P-wave as direct or refracted. So the curve in Figure 6.3.7 shows how the energy of surface waves and direct waves or refracted waves can be related in the field.

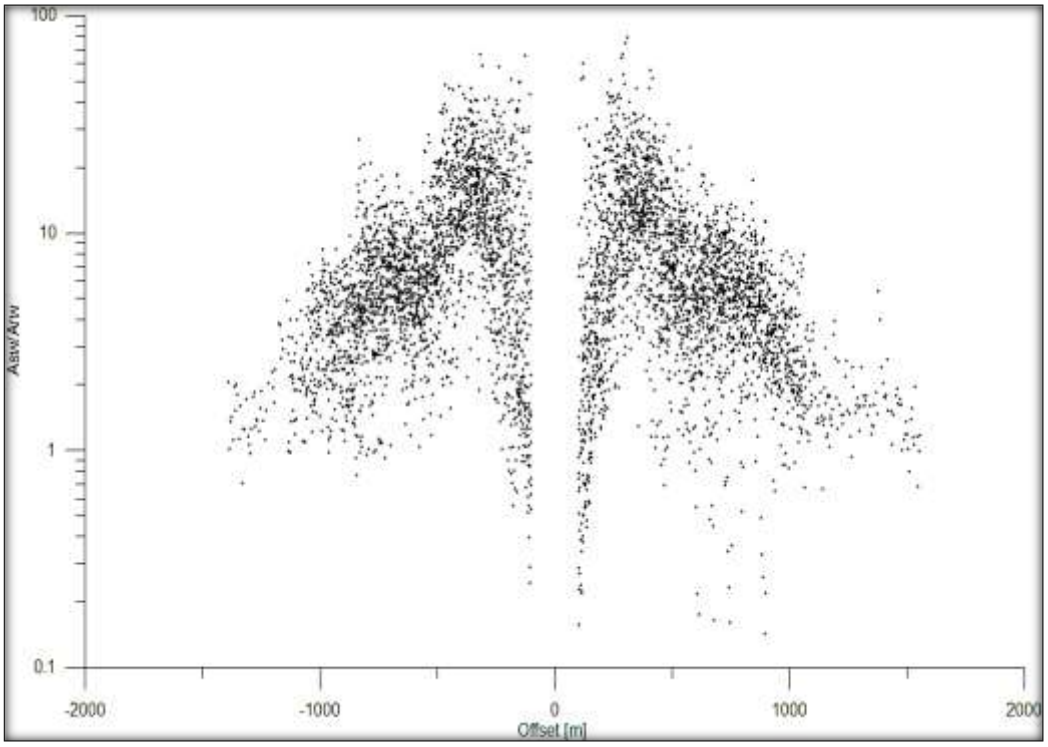

Figure 6.3.7: Amplitude ratio: surface wave/refracted wave.

6.4 "Noisy" synthetic data: simulating field data

After noise analysis in the field records, we are now in position to add ambient and coherent noise to our synthetic data. Several wave types are added to the 3D synthetic shot gathers in accordance with the results from the field data analysis. Coherent wavetrains include surface and air waves. Ambient noise is simulated by adding random noise (numbers) in percentages (Bekara, 2009), relative to the signal strength. Another type of noise is added through simulation of an imperfect static computation. This is achieved by adding random time shifts to the receiver and shot stations, by dta base manipulation and transfer to trace headers as time delays.

A "raw" 3D synthetic gather in its original shape, as produced by the numerical scheme, is shown in Figure 6.4.1.

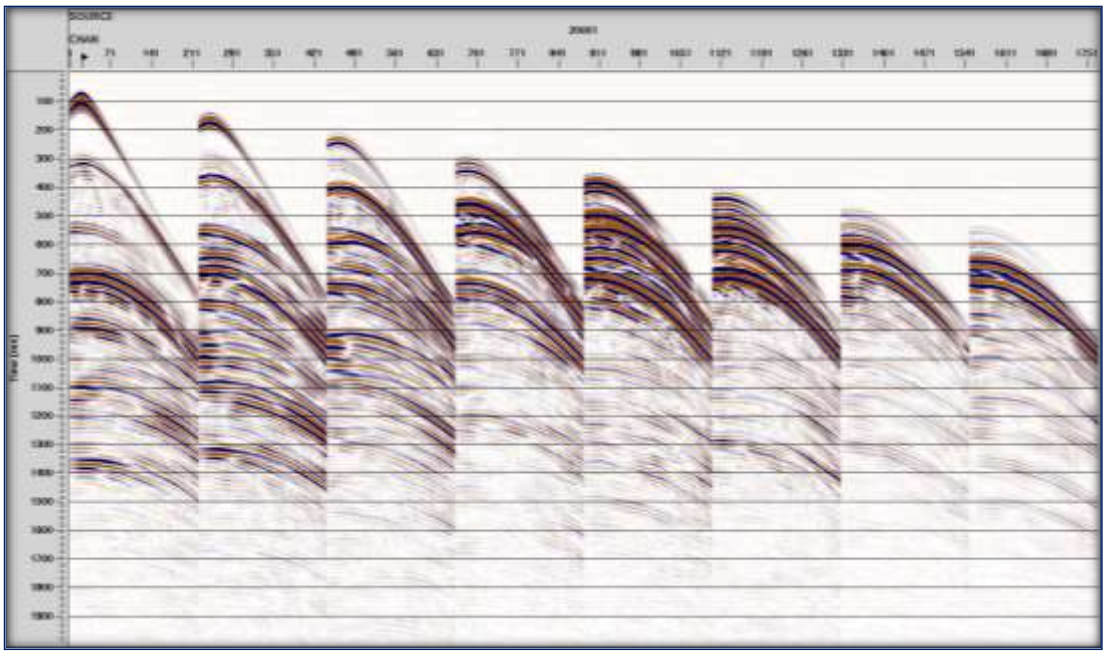

Figure 6.4.1: The 3D synthetic shot gather created by a stand-alone modelling program (A. Dzunic, 2014, personal communication). Data were written in SEG-Y format to simplify the importing process into the ProMAX® (Landmark Graphics Corporation) processing package. Individual trace scaling applied.

The same gather after the addition of surface and air waves is shown in Figure 6.4.2.

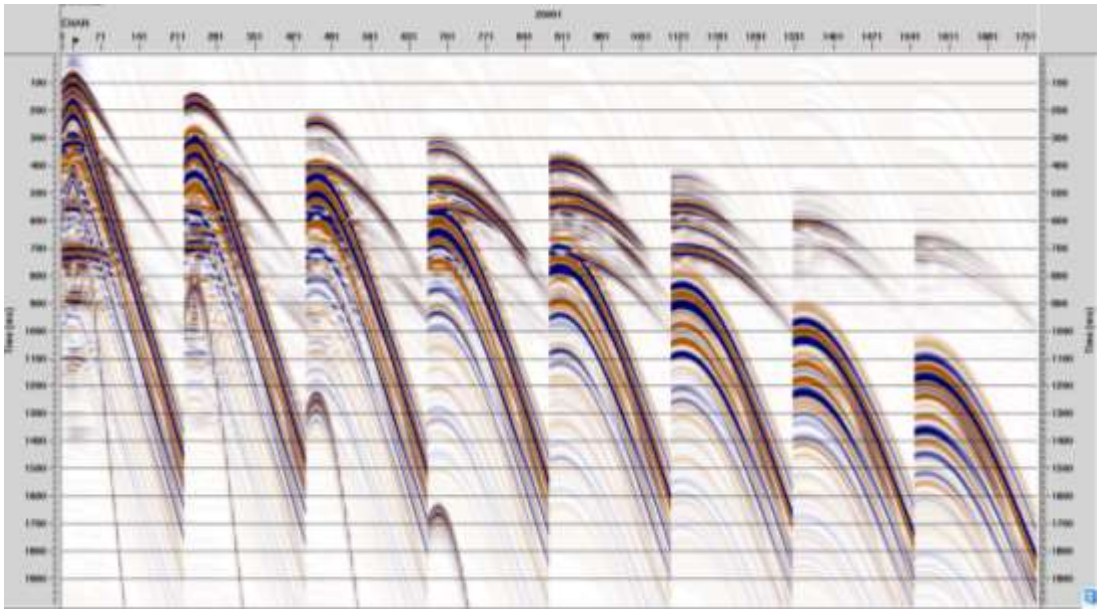

Figure 6.4.2: The 3D synthetic shot gather after the addition of source-generated noise: surface and air waves. Peak amplitude is scaled down relative to the raw gather to avoid clipping the surface waves.

Random noise is added in three stages to cover the range observed in the field gathers. This corresponds to the actual signal-to-noise values of 1, 1.3 and 1.6 respectively. In percentages, these stages can be expressed as 100%, 130% and 160%. The latest is stage 3 (Figures 6.4.3 to 6.4.5).

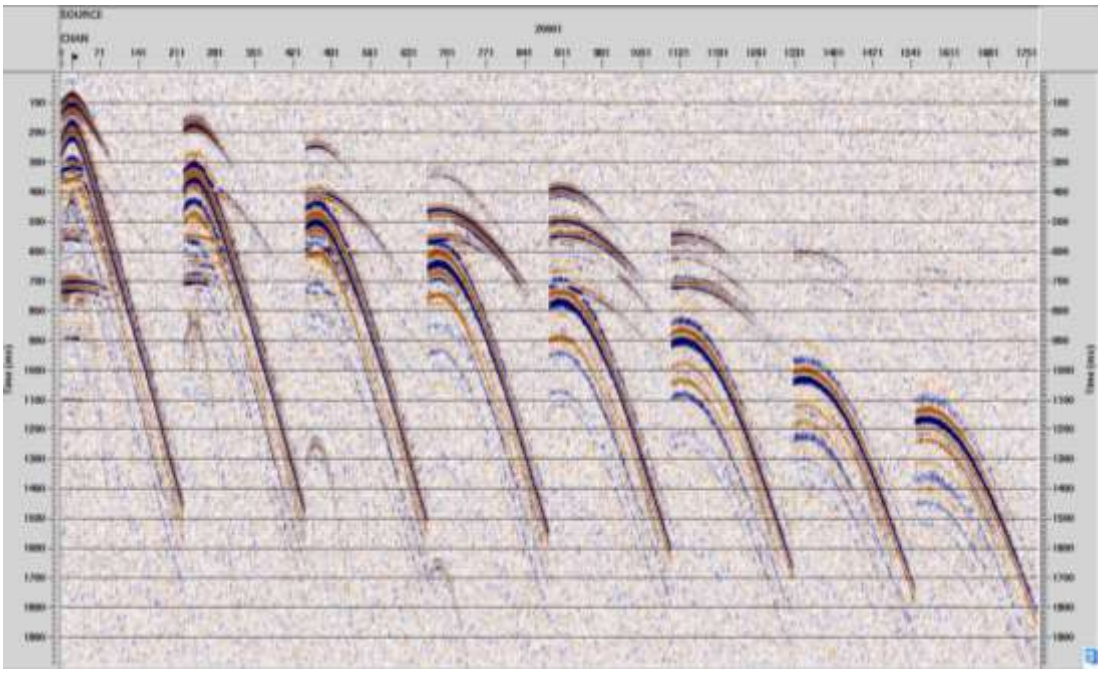

Figure 6.4.3: 100% of random noise added to the synthetic gather shown in Figure 6.4.2.

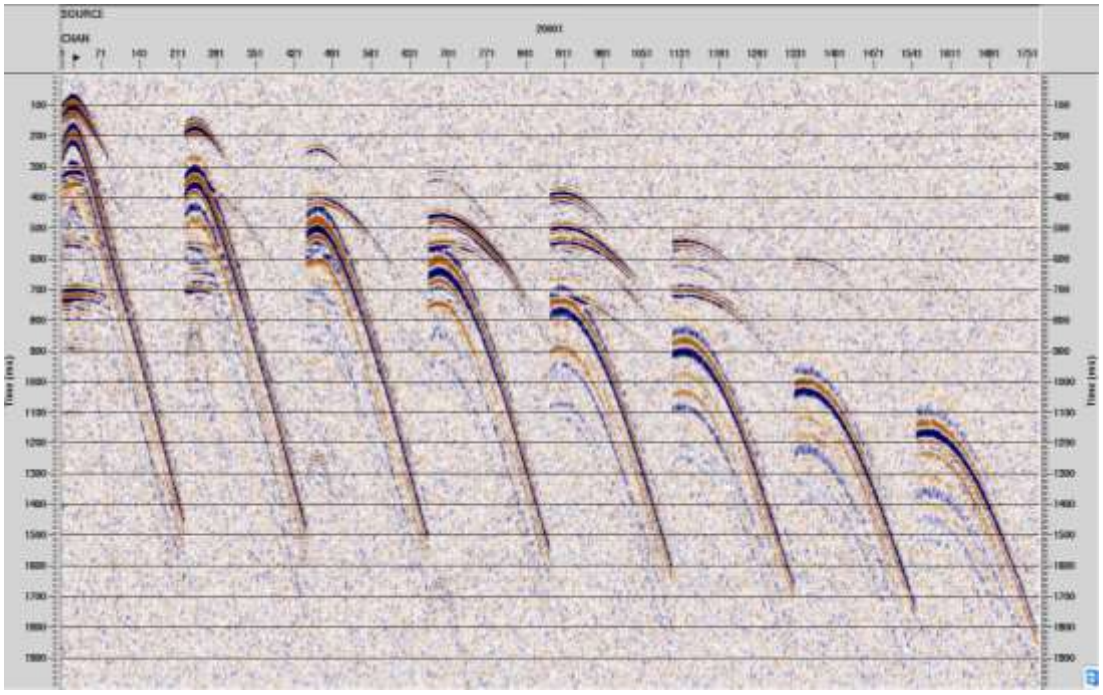

Figure 6.4.4: 130% of random noise added to the synthetic gather. Primaries are not clearly visible in the last two receiver lines that are furthest from the source.

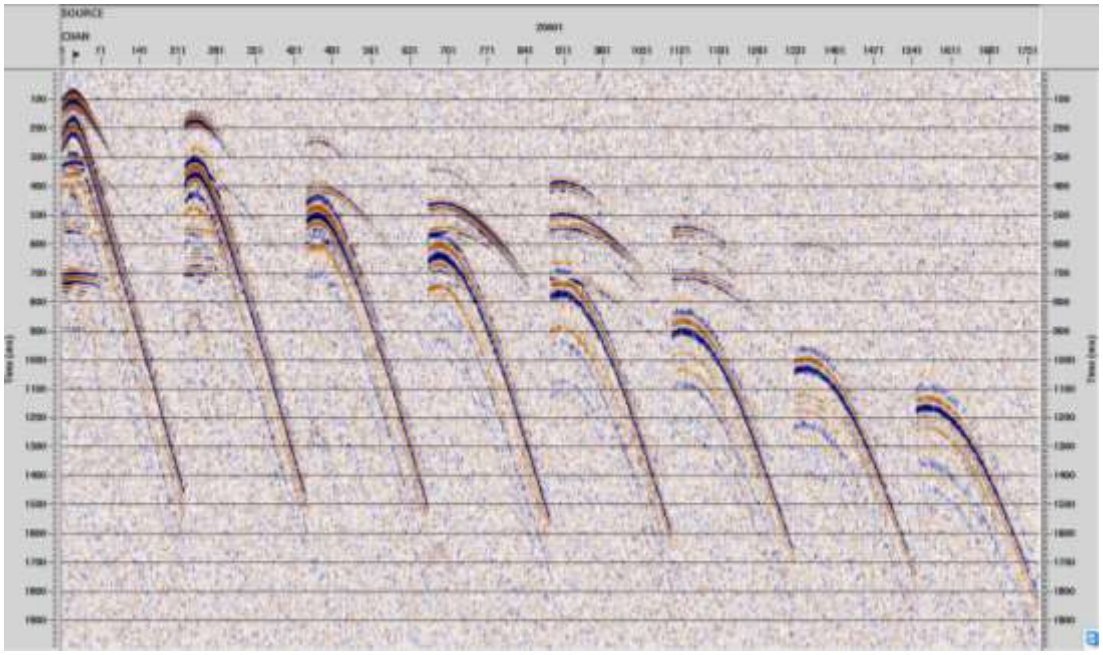

Figure 6.4.5: 160% of random noise added to the synthetic gather. Both direct and reflected waves are not visible in the last two receiver lines that are furthest from the source.

The final stage includes the addition of static shifts to simulate variable traveltimes through the near-surface weathered zone. Short wavelength statics are applied with variable intensities. The reason for this is that the refraction arrivals in the field gathers are not always visible, hence picking errors are likely and consequently, weathering static computed from the refraction arrivals may be inaccurate. The remaining traveltime misalignments after the application of the refraction statics may be of the magnitude of 5–10 ms. the net result is that reflection events will be misaligned to a degree proportional to the static correction error. Similarly, the higher the error is, the greater the attenuation of the high frequencies. This will be reflected in the interpretation process. Hence, it is of interest to observe the effects of imperfect static solutions on the image coherency and interpretability.

Figure 6.4.6 shows 3D shot record before the addition of static shots and random noise (130%), while Figure 6.4.7. shows the same record after the addition of ±5 ms static shifts and Figure 6.4.8 shows after the addition of 130 % of the noise to this misaligned data. The grey scale is used to make the shifts more visible and distinctive.

This example represents the most likely situation of small static errors combined with the moderate ambient noise.

Figure 6.4.6: Original 3D shot record displayed in grey scale

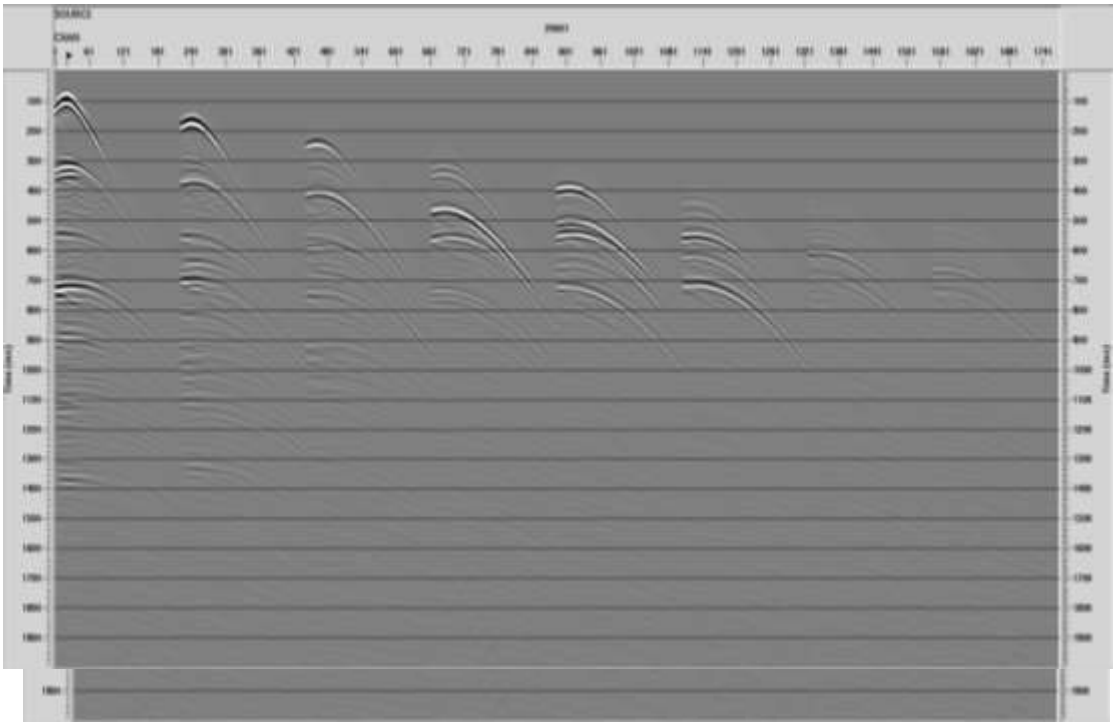

Figure 6.4.7: Original field record with addition of ±5 ms static shifts

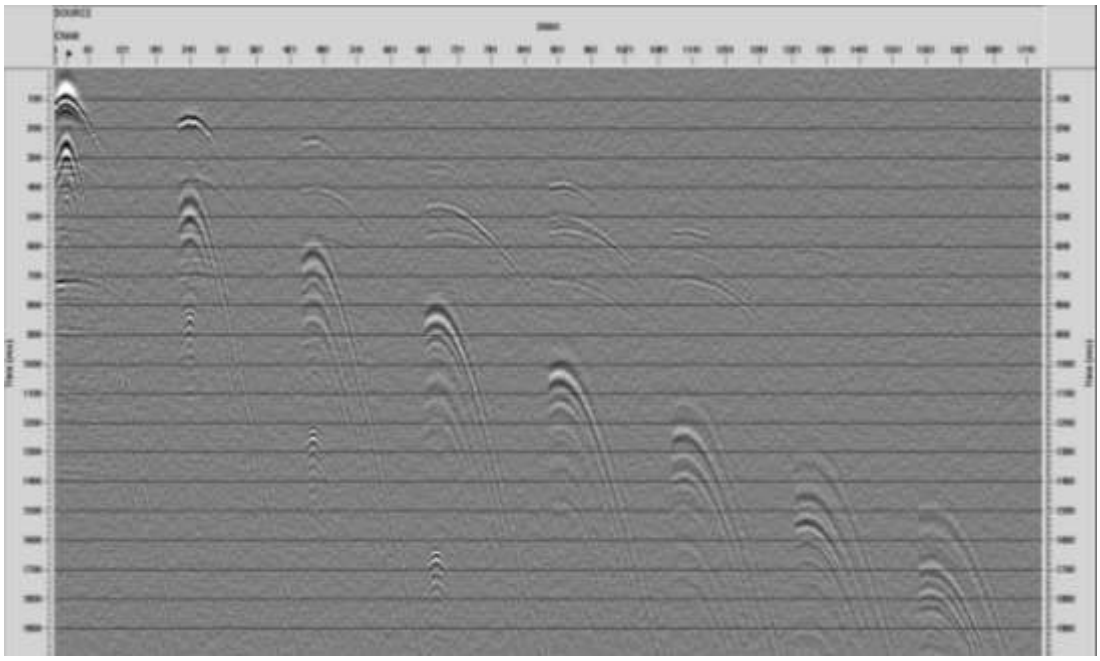

Figure 6.4.8: 3D shots after the addition of 130% noise and random static shifts of ±5 ms.

After adding coherent, ambient and processing (static) noise, the 3D synthetic shot gathers are now ready for full processing, stacking, migration and analysis.

These pictured figures presented in this chapter are to replicate conditions parameters in the field into the model data, because model data will always give perfect results. But the goal was not to replicate for something that is already known, but to establish how much noise we be handled. In other word, the ratios of such noises were taken from the field in order emerge them into the model and then by testing and decimation, reducing the number of channels, reducing the number of shots, in other word reducing the fold (effective number of traces within the CDP) that will produce high S/N ratio.

The purpose of measuring the amplitude of the noise, amplitude of the first break, amplitude of the refracted waves and amplitude of the surface waves is to establish ratio of the noises with respect to the initial signal (first arrival and the refracted wave) and perceive the effect on the model.

6.5 Effect of noise on stacked and migrated seismic images

The idea behind the noise examination in 2D field gathers and its reproduction in 3D synthetic gathers is to simulate the most likely outcome of a future 3D survey in this area, which may be undertaken for the detection of complex structures. Hence, to understand the impact of all types of noises discussed in Chapter 6.4 on the interpretability of seismic images, it is necessary to fully process the 3D gathers to the stack and migration stages.

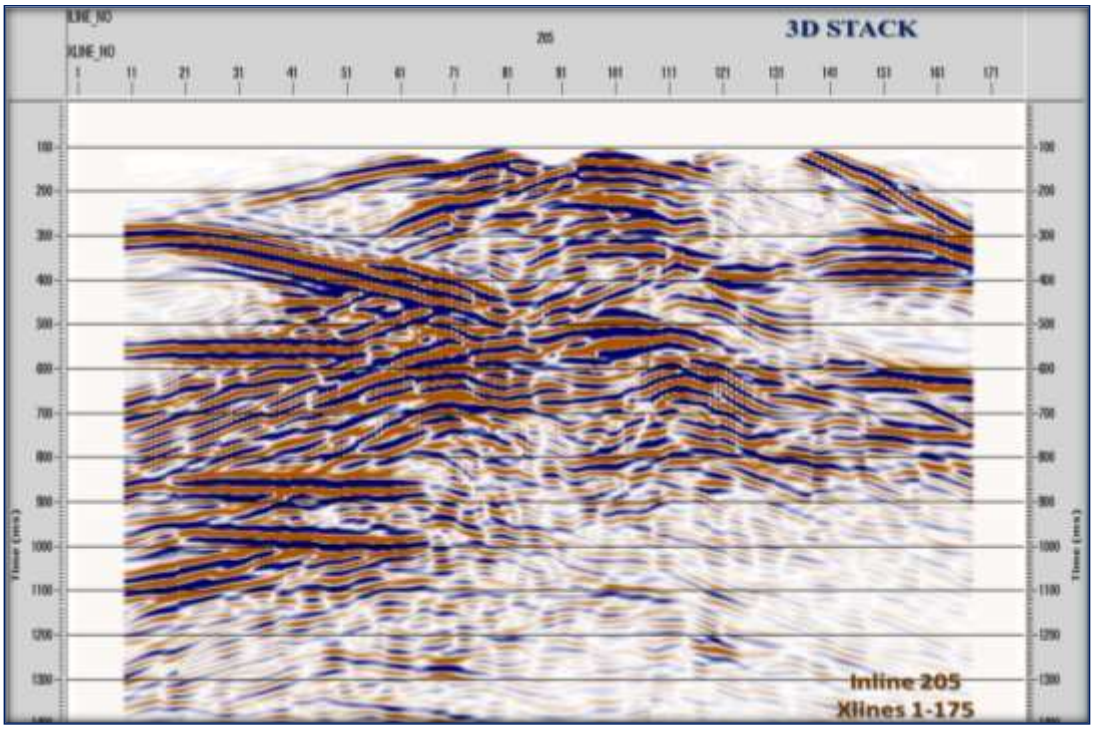

Figure 6.5.1: Inline 205 extracted from a 3D noise-free synthetic cube.

The first step is to process noise-free 3D synthetic shot gathers. That includes geometry application, CMP sorting, NMO application, filtering and 3D stacking. A selected inline from a 3D cube is shown in Figure 6.5.1. Despite of this noise-free inline, but it shows that the interpretation of complex structures is not a straightforward process. For land seismic, adding a relatively small percentage of ambient noise makes the process of interpretation a little harder, as some structural details appear to be lost, particularly at early times (Figure 6.5.2). Adding 160% of ambient noise and random static shifts of ±10 ms puts any interpretation effort into doubt (Figure 6.5.3). Clearly, such errors cannot be permitted if processing is to produce reliable 3D seismic images.

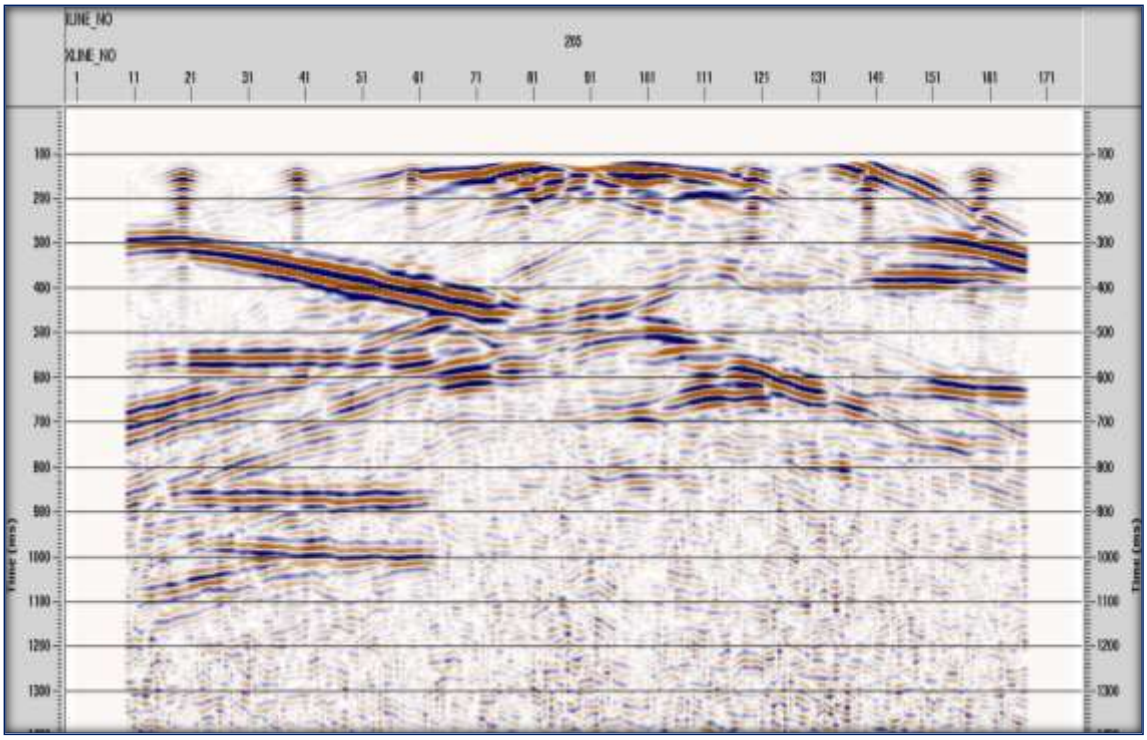

Figure 6.5.2: Inline 205 extracted from noisy 3D synthetic cube. 100 % of random noise and coherent, source-generated noise are added to the shot gathers.

In Figure 6.5.2 the 100% of random noise and coherent mans the same level or amount of field noise measured were added to the model data in order to get a normal model section with noise as in the field.

In Figure 6.5.3, Inline 205 extracted from noisy 3D synthetic cube with random and coherent noise, 100%, means the same amount or level measured in the field , source-generated noise are added to the shot gathers of the model.

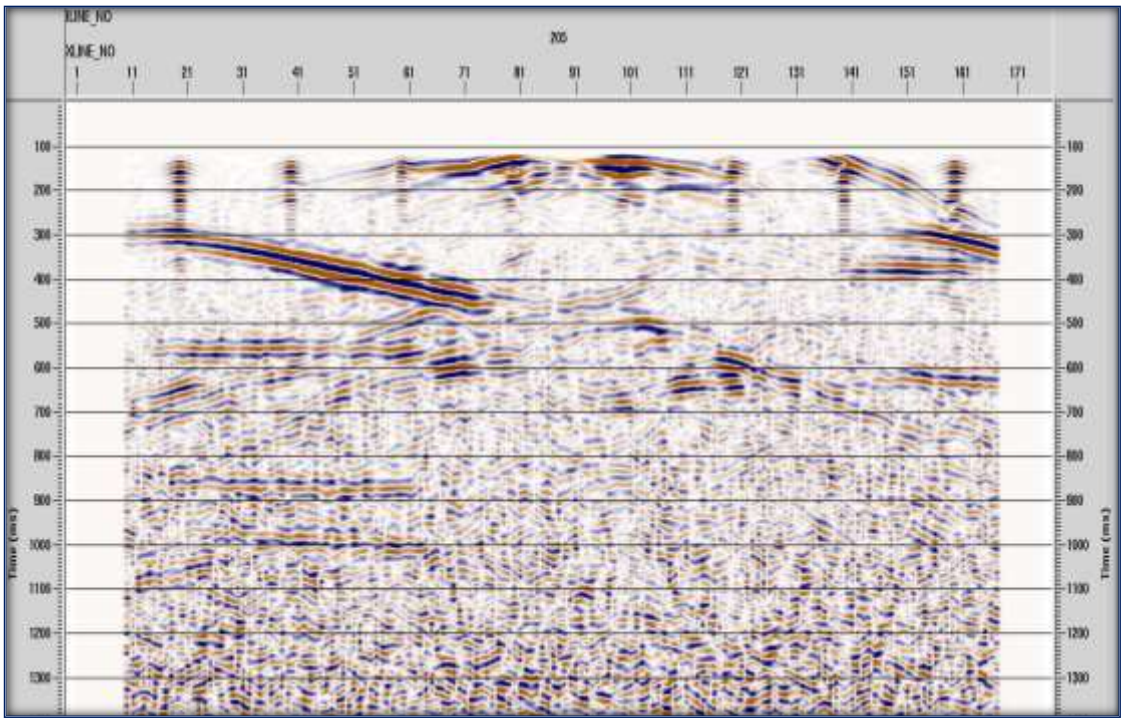

Figure 6.5.3: Inline 205 extracted from a noisy 3D synthetic cube. 100 % of random noise, coherent, source-generated noise and ±10 ms time delay errors are added to the shot gathers.

In figure 6.5.2 we do not have static correction shift introduced, but in Figure 6.5.3 we have error in resolving static correction. This showed us what the impact of the resolving the static correction has to do with the final outcome. When comparing the two Figures 6.5.2 and 6.5.3, it can reach to a conclusion that even 10 ms of static correction is not that critical for this can be solved through residual static correction.

The final analysis involves poststack depth migrated seismic images that are more likely to reveal the geometry of a complex structure. As before, the start of the work was by migrating the noise-free shot records (Figure 6.5.4). The image is simplified after migration and closer to the initial geological model. Equivalent migrated images after the addition of 160% of noise and ±10 ms static errors are displayed in Figure 6.5.5. Many structural details have been blurred and/or lost, which makes interpretation challenging. Another level of difficulties can be added by increasing the time delay errors to ±20 ms (Figure 6.5.6). Clearly, image coherency is completely lost and no viable interpretation can be achieved from such data.

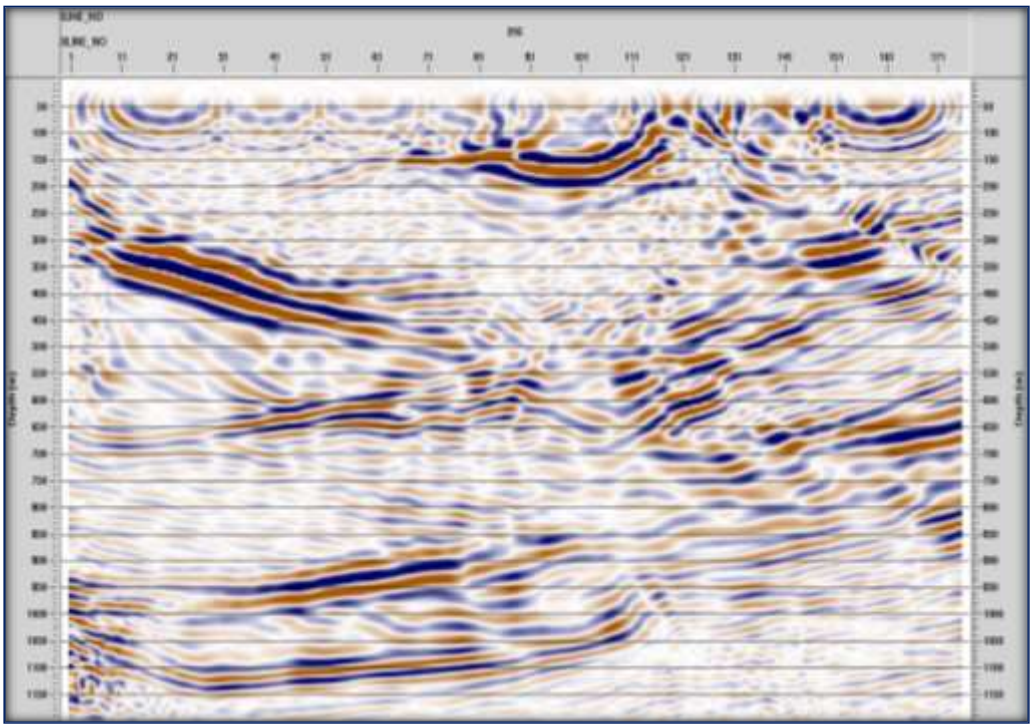

Figure 6.5.4: Inline 205: A 3D poststack depth-migrated noise-free seismic cube.

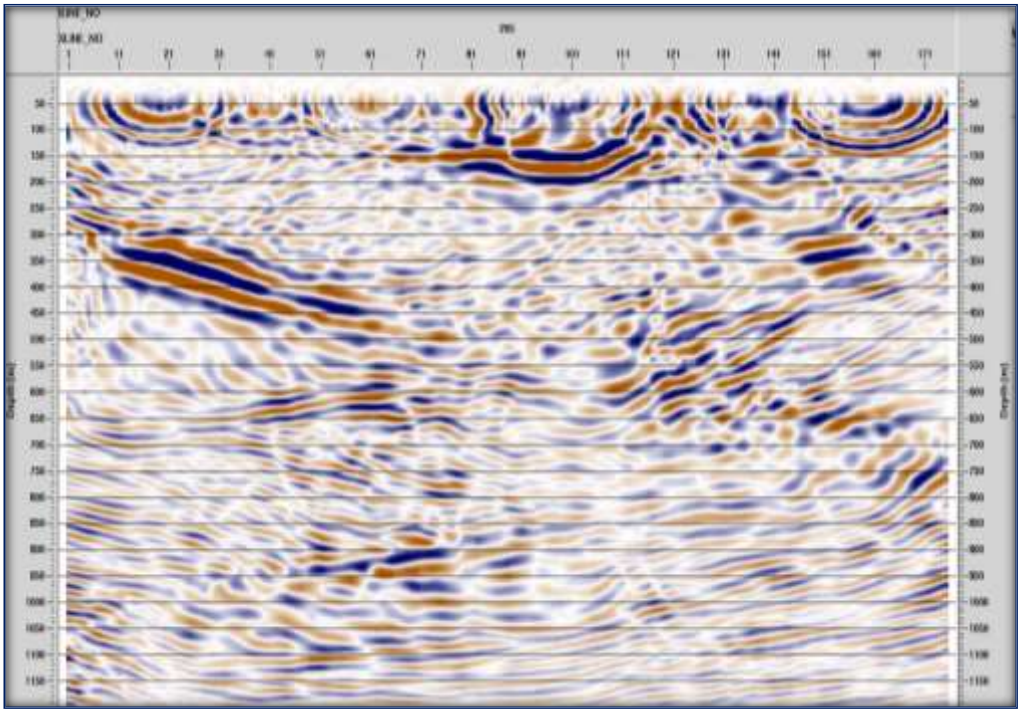

Figure 6.5.5: The inline poststack depth-migrated 3D volume after 160% of ambient noise combined with ±10 ms variable time delays is applied to the synthetic shot records. Inline section 205 is shown as extracted from the volume.

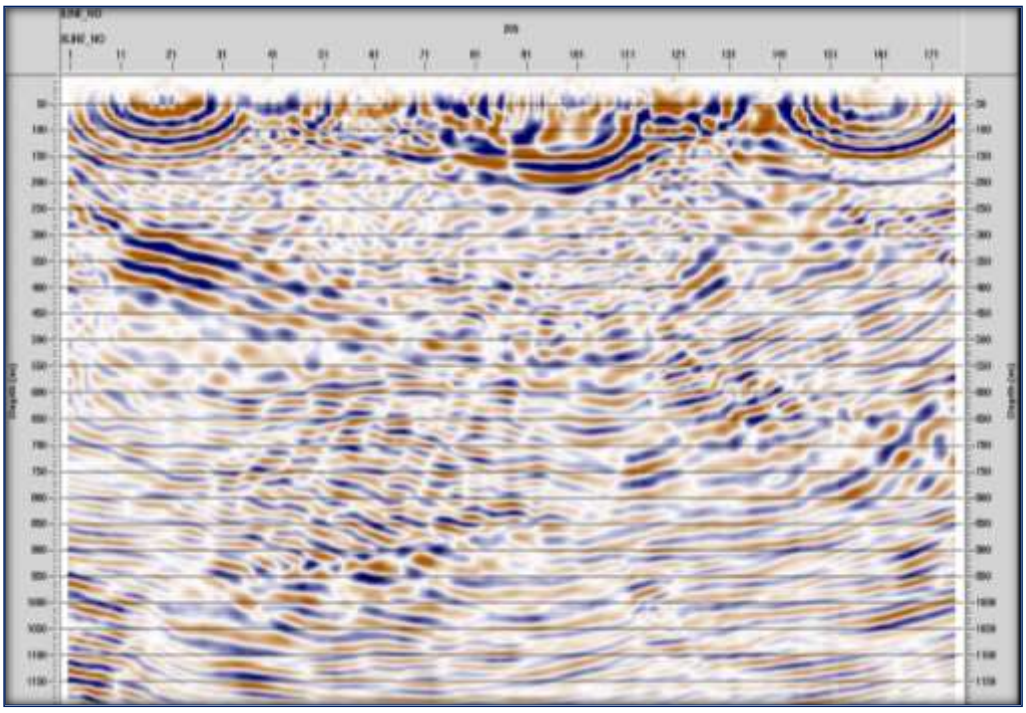

Figure 6.5.6: The inline poststack depth-migrated 3D volume after 160% of ambient noise combined with ±20 ms variable time delays is applied to the synthetic shot records. Inline section 205 is shown as extracted from the volume.

6.6 Conclusions

The idea of using a physical model to analyse the seismic response of complex structures is utilised in this research, so then the most probable geological situation can be built. A conventional 3D surface geometry is then used to acquire the 3D synthetic shot gathers over the "geological model". The output is refined to make it more similar to the real field data by incorporating appropriate noise trains that are inferred from the 2D seismic data. Numerical simulations are then used to study the seismic response over complex fault structures, such as the 'flower' structure. It appears evident that the addition of only a moderate amount of ambient noise, in combination with random delays through the weathered zone, makes the seismic images difficult to analyse. It can be concluded that complex structures, such as the 'flower' structure, are difficult to identify in low-quality seismic data. A very high S/N, skilful processing and careful interpretation are needed for the positive identification of a 'flower' structure.

CHAPTER 7

7.1 Conclusions and Discussions

Seismic interpretation of the six 2D seismic lines recorded along Tuart Road and Clover Road, across Gnangara Mound, Perth Basin suggests the presence of several faults within the Yarragadee aquifer over a depth range of 200–1500 m. The potential presence of complex discontinuities, such as the 'flower' structure of a negative type, is of particular concern for the purpose of building a realistic hydraulic dynamic model of this area. The existence of such structures could have significant impact on groundwater fluid flow within Yarragadee Aquifer. Therefore, it is necessary to further study seismic images and search for a better and more consistent data set for interpretation.

Complex faults are difficult to positively identify from 2D seismic data, particularly in the absence of wireline logging. The 2D interpretation study performed during this research work postulate the presence of complex faulting. However, to make an additional step towards the validation of such a hypothesis, I first conducted extensive 2D forward-modelling. A detailed 2D synthetic study reveals that in an ideal case, the detection of such structure is possible when there is an optimum line orientation with respect to the structure and exceptionally high signal to noise ratio S/N.

To make this examination more realistic I conducted 3D physical model of a 'flower' structure. The model was then CAT scanned and translated into a binary code using commercial and in-house developed packages by Dzunic (2014). Properly formatted output is utilised for the 3D numerical modelling studies. The modelling included the generation of hundreds of 3D shot records. To make the model closer to reality, I examined seismic noises in the field records and then generated the same type of noise numerically and included it into the 3D shot records. In addition to the source-generated noise and ambient noise, I added random static shifts, simulating imperfect refraction and residual static solutions. Full processing of noise-free and noise-contaminated 3D shot gathers was then conducted. The results suggest that 3D seismic has a better chance of illuminating and validating complex structures, but only if very

careful processing was conducted and the SNR is preserved or recovered through the survey design. When choosing acquisition parameters, the effect of source-generated noise on the final seismic image must be considered and then deploying appropriate spatial sampling. This will enable an unaliased recording of the coherent noise, which is removed using digital filtering. Sufficient CMP fold has to be utilised to combat ambient (random noise) (Bekara, 2009). Hence, 3D surveys that are used to obtain high definition images of shallow fault structures are very expensive. This situation can be somewhat mitigated since 3D seismic processing algorithms are a far more powerful tool for noise suppression than equivalent 2D processes. A good example is S/N suppression achieved by using F-XY (3D data processing deconvolution) in comparison to F-XY (2D data processing deconvolution) (Bekara, 2009). Therefore, the detection of complex, shallow fault structures requires dense acquisition and more reliable processing as a prerequisite for consistent interpretation. This presumes high spatial sampling that translates to a higher receiver and shot densities and hence more expensive surveys. True amplitude processing is necessary in either the time (or preferably) the depth domain, followed by prestack imaging.

Physical modelling and CAT scanning provide very effective process for generating realistic 3D numerical models. Subsequent seismic responses can then be rapidly computed in prestack or poststack domains. Physical model construction and scanning has now been developed to a stage where both can be achieved in a matter of 1–2 days. Hence, it is a far more cost-effective and efficient method of generating numerical 3D models than is generally in use today.

7.2 Recommendations

Utilising novel computer driven technology, such as 3D printers, can further perfect physical model construction process. This would bring new dimension to the current process by providing extra precision in model construction when required. The choice of modelling materials is yet to be fully assessed with respect to the X-Ray propagation effects. That could expand current studies to the area of fluid saturated media that might be of particular importance not only for water exploration but also for oil and gas exploration.

To make the proposed process of forward modelling, particularly in pre-stack domain, it is necessary to introduce additional effective flexibility into the numerical computations. To achieve this, there will be a need of very large computing clusters that can produce updated responses in very short time frame. The importance of fast computing response would be amplified by the introduction of full 3D elastic modelling. Additional elastic parameters, such as shear velocity, could help the process of identification and characterisation of complex structures, particularly in terms of their fluid flow properties.

In any case, it appears that forward 3D numerical studies are at least helpful, if not required, for characterising complex structures and further deriving dynamic models of a high relevance to water exploration objectives, at least in Perth Basin.

REFERENCES

Alaei, B., 2012, Seismic Modelling of Complex Geological Structures: INTECH (Institute of Technology), Open Access Publisher, 2012.

Allen, A. D., 1976, Outline of the hydrology of the superficial formations of the Swan Coastal Plain, Western Australia Geological Survey Annual Report 31-42.

Anderson, N., and Cardimona, S., 2000, Forward Seismic Modelling, The key to understand reflection seismic and Ground Penetrating (GPR) Techniques: Geophysics, 11–15

Australian Bureau of Statistics, 2010, Profiles of major minerals, oil and gas, Australia Bureau of Agricultural and Resource Economics (ABARE), 1301.0 - Year Book Australia, 2009–10.

Asquith, G. B., and Gibson, C. R., 1982, Basic well logs analysis for geologists*:* AAPG Methods in Exploration, **3**, 216.

Backhouse, J., 1984, Revised Late Jurassic and Early Cretaceous stratigraphy in the Perth Basin: Western Australia Geological Survey, Report 12, 1–6.

Backhouse, J., 1993a, Palynology and correlation of Permian sediments in the Perth, Collie, and Officer Basins, Western Australia: Western Australia Geological Survey, Report 34, p. 111–128.

Backhouse, J., 1988, Late Jurassic and Early Cretaceous palynology of the Perth Basin, Western Australia: Western Australia Geological Survey, Bulletin 135.

Ballesteros, M. W., 1991, A Two Dimensional Modelling Study, Exploration, Geophysics, **22**, 23–26.

Bansal, R., and Sen, M. K., 2008, Finite-difference modelling of Swavesplitting in anisotropic media: Geophysical Prospecting, 56, 293-312

Barbour, S. L., and Krahn, J., 2004, Numerical modelling–Prediction or process, Geotechnical News, **22**, 44–52

Barthwal, H., 2010, Finite difference modelling of P-SV wave propagation in 2D elastic media with PML boundary conditions: Wadia Institute of Himalayan Geology, Dehradun, 8th Biennial International Conference 7 Exposition on Petroleum Geophysics, 73.

Bekara, M. and Van der Baan, M., 2009, Random and coherent noise attenuation by empirical mode decomposition: Geophysics, **74**, 89–98.

Bensen, G., D., and et al., 2007, processing seismic ambient noise data to obtain reliable broad-band surface wave dispersion measurements: Geophysics Journal International **169**, 1239–1260.

Bozanic, D., 1969a, Gage Roads 1 well completion report: Western Australia Geological Survey, S-series, S431

Bormann, P. and Wielandt, E., 2013, Seismic signal and noise, Chapter 4, formerly GFZ German Research Centre for Geosciences, Department 2: Physics of the Earth, University of Stuttgart, Germany.

Bradshaw, J.1, et al., 2000, GEODISC Project 1- Regional Analysis, Stage 2 Basins – Perth Basin, Western Australia, Australian Petroleum CRC, Appendix 1 of report no. RPT06-0162

Bradshaw, B. E., et al., 2003, A revised structural framework for frontier petroleum basins on the southern and southwestern Australian continental margin. Geoscience Australia, Record 2003/03

Cadman, S. J., Pain, L., and Vuclovic, V., 1994, Perth Basin, WA, Australian Petroleum Accumulations, Bureau of Resources Sciences, Canberra, Report **10**.

Calvert, A., J., 2003, A method for avoiding artifacts in the migration of deep seismic reflection data: Department of Earth Science, Simon Fraser University, Canada, Technogeophysics, 338, 201-202.

Carcione, J. M., Feliciangeli, L. P., and Zamparo, M., 2002, The exploding-reflector concept for ground-penetrating-radar modelling: Annals of Geophysics, **45**, 3–4.

Carcione, J. M., Herman, G., C., and Kroode, A., P., ten, E. 2002, Seismic modeling: Geophysics, 67, 1304–1325.

Carlson, W. D., 2006, Three Dimensional Imaging of earth and planetary materials: University of Texas, Austin, Earth and Planetary Science Letters **249**, 133–147.

Carr1, L.K. et al., 2011, Structural and Stratigraphic Architecture of Western Australia's Frontier onshore sedimentary Basins: The Western Officer and Southern Carnarvon Basins, Geological Survey Division, Department of Mines and Petroleum, Western Australia.

Castro, J. S., Suarez, K., Jeantet, D., and Germain, C., 2007, Coherent Noise Filtering using Reconstructed Phase Space: Laboratoire de l'Intégration du Matériau au Système, Bordeaux University, BP. 99, F-33402, Talence - Cedex, France.

Chopra, S., 2005: Seismic Elastic Modelling: CSEG National Convention, Calgary, Canada, presented at the (2004).

CSIRO, 2005, Water for a Healthy Country, National Research Flagships publications, Canberra, Australia (2005)

Claerbout, J. F., 1985, Imaging the earth's interior: Blackwell Scientific Publications, Inc., Palo. Alto, CA, USA

Cnudde, V., et al., 2006, Recent progress in x-ray CT as a Geoscience Tool: Ghent University, Sedimentary Geology and Engineering Geology, Belgium, department of Applied Geochemistry, **21**, 826–832.

Cockbain, A. E., and Playford, P. E., 1973, Stratigraphic nomenclature of Cretaceous rocks in the Perth Basin: Western Australia Geological Survey, Annual Report for 1972, p. 26–31.

Cockbain, A. E., 1990, Perth Basin, the geology and mineral resources of Western Australia, Geological Survey of Western Australia, Memoir **3**, 495-525 .

Colburn, R., H., and Mooney, W. D., 1986, Two-dimensional velocity structure along the synclinal axis of the Great Valley, California: Bulletin of the Seismological Society of America., **76**, 1305–1322.

Collins, A. S., 2003, Structure and age of the northern Leeuwin Complex, Western Australia: constraints from field mapping and isotopic analysis, Australian Journal of Earth Sciences, 50, 585–599.

Crain, E. R., 1974, modelling with Gardner's Equation, Crain's Petrophysical Handbook, Canada.

Crostella, A., 1995, An evaluation of the hydrocarbon potential of the onshore northern Perth Basin, Western Australia. Western Australia Geological Survey, Report 43, 67p.

Crostella, A., and Backhouse, J., 2000, Geology and petroleum exploration of the central and southern Perth Basin, Western Australia: Geological Survey of Western Australia, Report **57**.

Cupillard, P., Stehly, L., and Romanowicz, B., 2011, The one-bit noise correlation: a theory based on the concepts of coherent and incoherent noise: Geophysical Journal International, **184**, 1397–1414.

Davidson, W. A., 1960, Perth Shallow Groundwater Systems Investigation, Lake Muckenburra; Government of Western Australia, Department of Environment, Hydrogeology record series, Report no. HG**46**.

Davidson, W. A., 1995, Hydrogeology and groundwater resources of the Perth region; Western Australia: Geological Survey of Western Australia, Bulletin **142**.

Davidson, W. A., and Yu, X., 2004, Perth Region Aquifer Modelling System PRAMS: Hydrogeology and groundwater modelling: WA Department of Environment, Hydrogeology, Report **202**.

Davidson, W., A., and Yu, X., 2006, Perth Regional Aquifer Modelling System (PRAMS) model Development; Hydrogeology and groundwater modelling: Western Australia Department of Water, Hydrogeological record series HG 20.

De Silva, J., 2009, Perth region aquifer modelling system (PRAMS) scenario modelling for the Gnangara Sustainability Strategy, Hydrogeological record series report no. HG39, Department of Water, Perth

Department of Water, 2009, Gnangara, Water resource allocation and planning series, Report no 30, Government of Western Australia.

Dingus, C., 2010, Seismic Processing-Noise Attenuation Techniques for relative Amplitude Processing: Petroleum Africa, Technology and Solutions, 47–49.

Duff, B. A., and D. J. Mason, 1989, The Instantaneous-Phase Time Slice, A Crucial Display for Enhancing 3D Interpretation: Exploration Geophysics **20**, 213–217.

Dzunic, A., 2014, Personal communication, Department of Exploration Geophysics, Curtin University, Western Australia

Empire Oil & Gas NL, 2015, Perth Basin, ASX Release, Western Australia

Energy in Australia, 2012, Bureau of Resources and Energy Economics, Australian

Engelberg, D. L., and et al., 2012, 3D imaging of inhomogeneous lithologies using x-ray computed tomography: Mineralogical Magazine, **76**, 2931–2938.

Etgen, J. T., and O'Brien, M. J., 2007, Computational methods for large-scale 3D acoustic finite-difference modeling: A tutorial: Geophysics, 72, SM223–SM230.

Fairbridge, R. W., 1953, Australian Stratigraphy, University of Western Australia Text Books Board, Western Australian Press, Perth.

Falvey, D. A. and Mutter, J. C., 1981, Regional plate tectonics and the evolution of Australia's passive continental margins: BMR Journal of Australian Geology and Geophysics, v. 6, p. 1-29.

Fredman, N., et al., 2008, Faults Facies Modelling; Techniques and approach for 3D conditioning and modelling of faulted grids: Department of Earth Science, University of Bergen, Norway, AAPG Bulletin **92**, 1457–1478.

Gjøystdal, H., et al., 2002, Review of ray theory applications in Modelling and imaging of seismic data: Stud. Geophysics Geodesy Prague; **46**, 113–164.

Guillaume, P., Chazalnoël, N., Talaalout, A., Zhang, X., Epili, D., and Dirks, V., 2003, 3D finite-offset depth tomography model building: Green Canyon, Gulf of Mexico, Analysis, **5**, 1.

Guillaume, P., et al., 2008, Kinematic invariants: an efficient and flexible approach for velocity model building: In 78th annual SEG meeting, SEG workshop "Advanced velocity model building techniques for depth imaging"

Glasson, S. H., Sheldon, R. L., and Oldham, C., 2011, Investigation of salinity within the Yarragadee Aquifer in the Perth area: University of Western Australia, Doctoral dissertation, University of Western Australia.

Hall, P.B. and Kneale, R.L., 1992, Perth Basin rejuvenated, APEA J., **32**, 33–43.

Harris, L. B., 1994, Structural and tectonic synthesis for the Perth basin, Western Australia, Journal of Petroleum Geology, **17(2)**, 129–156

Harris, B. D., et al, 2011, Seismic Reflection and Ground Penetrating Radar Transects across the North Gnangara Mound; Perth Basin; Western Australia, ASEG – PESA, 2013, Melbourne, Australia.

Heath, J., 2013, the water supply in Perth, Western Australia**,** Water Corporation of Western Australia, VICORP.

Henley, D. C., 1999, Coherent noise attenuation in the radial trace domain: Introduction and demonstration: CREWES Research Report, **11**.

Henley, D. C., 2003, Coherent noise attenuation in the radial trace domain: Geophysics, **68**, 1408–1416.

Henley, D. C., 2011, Attenuating 2D Noise in a 3D World: Recovery, CSPG CSEG CWLS Convention.

Holcomb, L. G., 1989, Seismic noise: Encyclopaedia of Earth Science, Geophysics, Van Nostrand Reinhold.

Howell, L. G., and Frosch, A., 1939, Gamma-ray Well-logging: Geophysics, **4**, 106–114.

IESC, 2014, Connectivity between water systems, Independent Expert Scientific Committee on Coal Seam Gas and Large Coal Mining Development, Department of the Environment, Canberra, Australia

Igel, H., Mora, P., and Riollet, B., 1995, Anisotropic wave propagation through finite-difference grids: Geophysics, 60, 1203–1216.

Janssen, D. P., Collins, A. S., and Fitzsimons, I. C.W., 2003, Structure and tectonics of the Leeuwin Complex and Darling Fault Zone, southern Pinjarra Orogeny, Western Australia; a field guide, Western Australia Geological Survey Record, 2003/15, 33 pp

Johnson, M., and Vincent, C., 2002, Development and testing of a 3D velocity model for improved event location, A case study for the India-Pakistan region: Bulletin of the Seismological Society of America, **92**, 2893–2910.

Julien, N., 2008, Advantages of CT in 3D Scanning of Industrial Parts: 3D Scanning Technologies Magazine, **1**, no. 3, 2008.

Karina, M., et al., 2011, Using ^{14}C and ^{3}H to delineate a recharge 'window' into the Perth Basin aquifers, North Gnangara groundwater system, Western Australia: Science of The total Environment, **414**, 456–469.

Katsavounidis, T., 2006, Policy on Accessing the Leederville and Yarragadee aquifers in Perth: Department of Water/Government of Western Australia.

Kayal, J. R., 1979, Electrical and gamma-ray logging in Gondwana and Tertiary coal fields of India: Geoexploration, **17**, 243–258.

Kelly, K. R., Ward, R. W., Treitel, S., and Alford, R. M., 1976, Synthetic seismograms, a finite-difference approach: Geophysics **41**, 2–27.

Kelly, A., England, R. W., and Maguire, P. K. H, 2007, A three-dimensional seismic velocity model for north-western Europe: Geophysical Journal International, **171**, 1172–1184.

Ketcham, R. A., 2005, Computational methods for quantitative analysis of three-dimensional features in geological specimens: Geosphere, **1**, 32–41.

Krassay, A. A., 1998, Outcrop and drill core gamma ray logging integrated with sequence stratigraphy: examples from Proterozoic sedimentary successions of northern Australia. AGSO Journal of Australian Geology and Geophysics **17(4)**, 285-299.

Krebes, E., S., 2004, Seismic Forward Modelling, CSEG Recorder April, 28–39.

Kumar, S., et al., 2008, Frequency enhancement of seismic data-a comparative study: Reliance Industries Limited, Petroleum Business (E&P), Mumbai, India, Recorder, **33**, no. 04.

Kummer, B. J., 2012, Elimination of incoherent noise from seismic data: University of Hamburg, Germany, SP5.3, 1586–1571, SEG-1994 Annual Meeting, Los Angeles.

Lambeck, K., 1987, The Perth Basin: a possible framework for its formation and evolution: Exploration Geophysics, **18**, 124–128.

Lasky, R. P., R. A., Young, and Middleton, M. F., 1991, Structural study of the Southern Perth Basin by Geophysical Methods: Exploration Geophysics, **22**, 199–206.

Lasky, R. P., and A. J., Moray, 1993, Structural and Tectonic Framework of the on shore Northern Perth Basin: Exploration Geophysics, **24**, 585–592.

Lasky, R. P., 1993, A Structural study of the Southern Perth Basin, Western Australia: Geological Survey, Report **31**, 56.

Lasky, R. P., et al., 1998b, A structural interpretation of the Gascoyne Platform, southern Carnarvon Basin, WA. In: Purcell, P.G. & Purcell, R.R., (Eds), the sedimentary basins of Western Australia 2. Proc. PESA Symposium, Perth, 587–598.

Lasky, R. P., D'ercole, C., Ghori, K. A. R., Mory, A. J., and Lockwood, A. M., 2003, Structure and petroleum prospectivity of the Gascoyne Platform, Western Australia: Geological Survey of Western Australia Report **87**.

Liu, Y., and Sen, M. K., 2009, Advanced finite-difference methods for seismic modelling: Geohorizons, 5-16.

Loewenthal, D. L., Roberson, R. Lu., and Sherwood, J. W. C., 1976, The wave equation applied to migration: Geophysical Prospect., **24**, 380–399.

Leyland, L., 2011, Hydrogeology of the Leederville Aquifer, central Perth Basin, Western Australia: Sort, **50**, 500.

Manning, P. M., and Gary F. M., 2004, Finite-difference modelling with correction filters in variable velocity, SEG Annual Meeting, 2004.

Marfurt, K. J., 1984, Accuracy of finite-difference and finite-element modeling of the scalar and elastic wave equations: Geophysics, 49, 533–549.

Marshall, J. F. et al., 1989, Hydrocarbon prospectivity of the offshore South Perth Basin: Australia Bureau of Mineral Resources, Record 1989/23.

Martin, M., and Xu, C., 2008, Assessing Impacts of Confined Abstraction on the Gnangara Mound, Western Australia: using Transient Response Functions, 2008: 1665–1676.

Martin, M., et al., 2013, High Resolution Seismic Reflection for Hydrology, ASEG, PESA, 23rd International Geophysical Conference and Exhibition, Melbourne, Australia

McPherson, A., and Jones, A., 2005, Appendix D: Perth Basin geology review and site class assessment: Natural Hazard Risk in Perth, Western Australia, 313–344.

McNamara, D. E., and Buland, R. P., 2004, Ambient noise levels in the continental United States: Bulletin of the seismological society of America, **94**, 1517–1527.

Mees, F., Swennen, R., Van Geet, M., and Jacobs, P., 2003, Applications of X-ray computed tomography in the geosciences: Geological Society, London, Special Publications, **215**, 1-6.

Meredith, K., Cendón, D., Hollins, S. North Gnangara Groundwater Dating, Western Australia, A report prepared for The Government of Western Australia (WA), Department of Water. ANSTO/C-1084 (2010)

Meredith, K., Cendón, D., I. Pigois, J-P., Hollins, S., and Jacobsen, G., 2012: Gnangara groundwater system, Western Australia, Science of The Total Environment, **414**, 456-469 (2012).

Moczo, P., et al., 2007, The Finite-Difference and Finite-Element Modelling of Seismic wave propagation and Earthquake motion, acta physica slovaca vol. **57** No. 2, 177 – 406

Mory, A. J., and Lasky, R. P., 1996, Stratigraphy and structure of the onshore northern Perth Basin, Western Australia: Geological Survey of Western Australia, **46**.

Mory, A. J., Haig, D.W., Mcloughlin, S., and Hocking, R. M., 2005, Geology of the northern Perth Basin, Western Australia—a field guide: Geology, 9.

Mufti, I., R., Pita, J., A., and Huntley R., W., 1996, Finite-difference depth migration of exploration-scale 3-D seismic data: Geophysics **61**, 776–794.

Mukerji, R. T., and Mavko, G., 2008, Analysing Thresholds for 3D Reconstruction of Rock from CT-Scan Images: SEG Annual Meeting, Society of Exploration Geophysicists (2008).

Murugan, S., Natarajan, V., and Kumar, R., 2012, Estimation of noise model and Denoising of wind driven ambient noise in shallow water using the LMS algorithm: Acoustics Australia, **40**, 111.

Meredith, K., Cendón, D.I., Pigois, J. P., Hollins, S., Jacobsen, G.,2012, Using 14^{C} and 3^{H} to delineate a recharge 'window' into the Perth Basin aquifers, North Gnangara groundwater system, Western Australia, Science of The Total Environment, **414**, 456-469 (2012).

Newman, M. E. J., and Sneppen, K., 1996, Avalanches, scaling, and coherent noise: Physical Review E, **54**, 6226.

Norris, S. E., 1972, The Use of Gamma Logs in Determining the Character of Unconsolidated Sediments and Well Construction Features: Groundwater, **10**, 14–21.

Novotny, O., 1999, Seismic Surface waves; Lecture notes for post-graduate studies: Instituto de Fisica, Instituto de Geociencias, Universidade Federal Da Bahia, and Brazil.

Offshore Petroleum Exploration Acreage Release, 2013, regional geology of the Perth Basin: Australia 2013, Department of Resources, Energy and Tourism, Geoscience Australia.

Owad, J. D., and Ellis, G., 2000, Western Australia atlas of petroleum field, onshore Perth Basin, Petroleum Division, Department of Minerals and Energy Western Australia, Vol. **1**,114.

Peterson, J., 1993, Observations and modelling of seismic background noise, 93–95

Pigois, J. P., Johnson, S., and Martin, M., 2010, A Window to Perth's confined aquifers on the north Gnangara Mound, Western Australia, 1–4.

Pigram, J., 2007, Australia's water resources: from use to management: CSIRO publishing.

Playford, P. E., Cockbain, A. E., and Low, G. H., 1976, Geology of the Perth Basin, Western Australia: Bulletin (Geological Survey of Western Australia) 124.

Plumb, K. A., 1979, The tectonic evolution of Australia: Earth-Science Reviews, **14**, 205–249.

Mukerji, R. T., and Mavko, G., 2008, Analysing Thresholds for 3D Reconstruction of Rock from CT-Scan Images: SEG Annual Meeting.

Owad-Janes, D. and Ellis, G., 2000, Western Australia atlas of petroleum fields, onshore Perth Basin, Petroleum Division, Department of Minerals and Energy Western Australia, Volume **1**, 114p

Russ, J. C., and Woods, R. P., 1995, The image processing handbook: Journal of Computer Assisted Tomography, **19**, 979–981.

Salama, R. B., Bekele, E., Hatton, T. J., Pollock, D. W. and Lee-Steere, N., 2002, Sustainable yield of groundwater of the Gnangara Mound, Perth, Western Australia: CSIRO Land and Water.

Schimmel, M., et al., 2011, Using instantaneous phase coherence for signal extraction from ambient noise data at a local to a global scale: Geophysical Journal International, **184**, 494–506.

Seletchi, E. D., and Duliu, O. G., 2007, Image Processing and Data Analysis in computed Tomography: Romanian Journal of Physics, **52**, 667–675.

Shan, C., Javandel, I., and Witherspoon, P., 1995, Characterization of Leaky Faults; Study of Water Flow in Aquifer-Fault-Aquifer Systems: Water Resources Research, **31**, 2897–2904.

Shapiro, N. M., Campillo, M., Stehly, L., and Ritzwoller, M. H., 2005, High-resolution surface-wave tomography from ambient seismic noise: Science,

Simpson, K. L., and Hayes, K. P., 1998, Drinking water disinfection by-products: an Australian perspective: Water Research, **32**, 1522–1528.**307**, 1615–1618.

Sinclair K. M., 2011, Evolving Issues and Practices in Groundwater-dependent ecosystem management, National Water Commission, Australian Government Protecting GDEs in a regional multi-aquifer system: South, Department Environment and Resource Management, Gnangara Sustainability Strategy, Perth Regional Aquifer Modelling System, Full Report Series No **46**,

Smith G. Le Blanc and S. Kristensen, 1998, Geology and Permian coal resources of the Vasse River Coalfield, Perth Basin, Western Australia, 1951-; Format: Book; vi, 49p.

Song, T., and Cawood, P. A., 2000, Structural styles in the Perth Basin associated with the Mesozoic break-up of Greater India and Australia: Technophysics **317**, 55–72.

Stefan, T., 2004, Digital Imaging, Data Handling Basic Image Processing: EMBL (European Molecular Biology Laboratory).

Stein, J. A., and Langston, T., 2007, A review of some powerful noise elimination techniques for land processing: 69th EAGE Conference and Exhibition-Workshop Package.

Summary of Petroleum Prospectivity: Perth Basin, 2014, Department of Mines and Petroleum, Petroleum Division, Government of Western Australia.

Thomas, B. M., and Brown, S. A., 1983, Hydrocarbon generation in the northern Perth Basin, APEA J., **23**, 64–74.

Thorpe, P. M., and W. A., Davidson, 1991, Groundwater age and hydrodynamics of the confined aquifers, Perth, Western Australia, in: Proceedings of International Conference in Large Sedimentary Basins, Perth, Western Australia, 1990: Australian Water Resources Council, Conference Series no **20**, 420-436.

Urosevic, M., Juhlin, C., 2007, An analysis of seismic information obtained from crooked line seismic surveys in crystalline rocks, Australia: 69th Meeting, EAGE.

Urosevic, M., et al., 2007, Seismic Exploration of Ore Deposits in Western Australia: Advances in regional exploration, in Proceedings of Exploration 07: Fifth Decennial Conference on Mineral Exploration, DMEC, 525-534.

Urosevic, M., and Dzunic, A., 2013, A Method for Rapid Generation of Complex 3D Models for Numerical Simulations: 75th EAGE Conference & Exhibition incorporating SPE EUROPEC.

Valenta, R. K., Jessell, M. W., Jung, G., and Bartlett, J., 2008, Geophysical Interpretation and Modelling of three-dimensional structure in the Duchess area, Mount Isa Inlier, Australia, ASEG **23**(2) 393-400.

Versteeg, R., and Grau, G., 1991, The Marmousi Experience, Proceeding of the 1990 EAEG workshop on practical aspects of seismic data inversion, European Association Exploration Geophysics, 1991.

Villarreal, A., and Scales, J. A., 1997, distributed three-dimensional finite-difference modelling of wave propagation in acoustic media: Computers in Physics, **11**, 388–399.

Virieux, J., 1984, SH-wave propagation in heterogeneous media, velocity-stress finite difference method: Geophysics **49**, 1933–1957.

Virieux, J., 1989, P-SV wave propagation in heterogeneous media, Velocity-stress fi nite-difference method: Geophysics **51(**4**)**, 889–901.

Weijia, S., Zhou, B., and Fu, Li-Y., 2010, Dip angle—compensated on-way wave equation Migration, Exploration Geophysics **41**, 137–145.

Wentworth, R. H., 1989, Theoretical Noise Performance of Coherence-Multiplexed Interferometric Sensors: Journal of Lightwave Technology **7**, 941–956.

Willmott, S.P., 1964, Revisions to the Mesozoic Stratigraphy of the Perth Basin, Western Australia. Eneabbba No.1. Petroleum Search Subsidy Acts. Publication, 54, p11-17

Woodcock, N. H., and Schubert, C., 1994, Continental strike-slip tectonics, In: HANCOCK, P. L. Continental Tectonics, Pergamum Press, Oxford, pp. 251-263.

White, R. E., 1984, Signal and noise estimation from seismic reflection data using spectral coherence methods: Proceedings of the IEEE, **72**, 1340–1356.

Xu, C. and Martin, M., 2008: Assessing impacts of confined abstraction on the Gnangara Mound using transient response functions, Infrastructure Planning Branch, Western Corporation of Western Australia.

Xu, C., 2008, Modelling of groundwater levels on the Gnangara Mound, text book, Water Corporation, Leederville, Western Australia.

Yang, Y., and Ritzwoller, M. H., 2008, Characteristics of ambient seismic noise as a source for surface wave tomography: Geochemistry, Geophysics Geosystems, **9,** no. 2.

Yilmaz, O., 2001, Seismic Data Analysis: Processing, Inversion and Interpretation of Seismic Data, Hardcover, 2nd Edition.

Zahradnik, J., 1995, A New Program Package for Modelling Seismic Ground Motions, Proc. Fifth International Conference on seismic Zonation, Nice (France), 2, 1221-1226.

Zahradnik, J., and Priolo, E., 1995, Heterogeneous formulations of Elastodynamic equations and finite-difference schemes: Geophysical Journal International, **120**, 663–676.

Zeng, Z., 2005, Termination of a strike-slip fault, Zhoukoudian, West Mountain, a short report about Zhoukoudian system, Beijing, China.

Zhoukoudian, 2005, Termination of a strike-slip fault West Mountain, Beijing, China (Zuoxun Zeng)

Zhu, Ch. and Murphy, W. M., 2000, Radiocarbon Dating of Ground Water, Ground Water, Vol. **38** (6), pp 802-804, Reviewed Journal.

Zhuping, S., and Donald, C. H., 1995, Conceptual models for earth assuring in Las Vegas Valley, Nevada, USA: IAHS Pub. No. 234

Appendix A

File 1: Data files used in the FORTRAN programming – 3D modelling

Log file example - 3dj022b.log

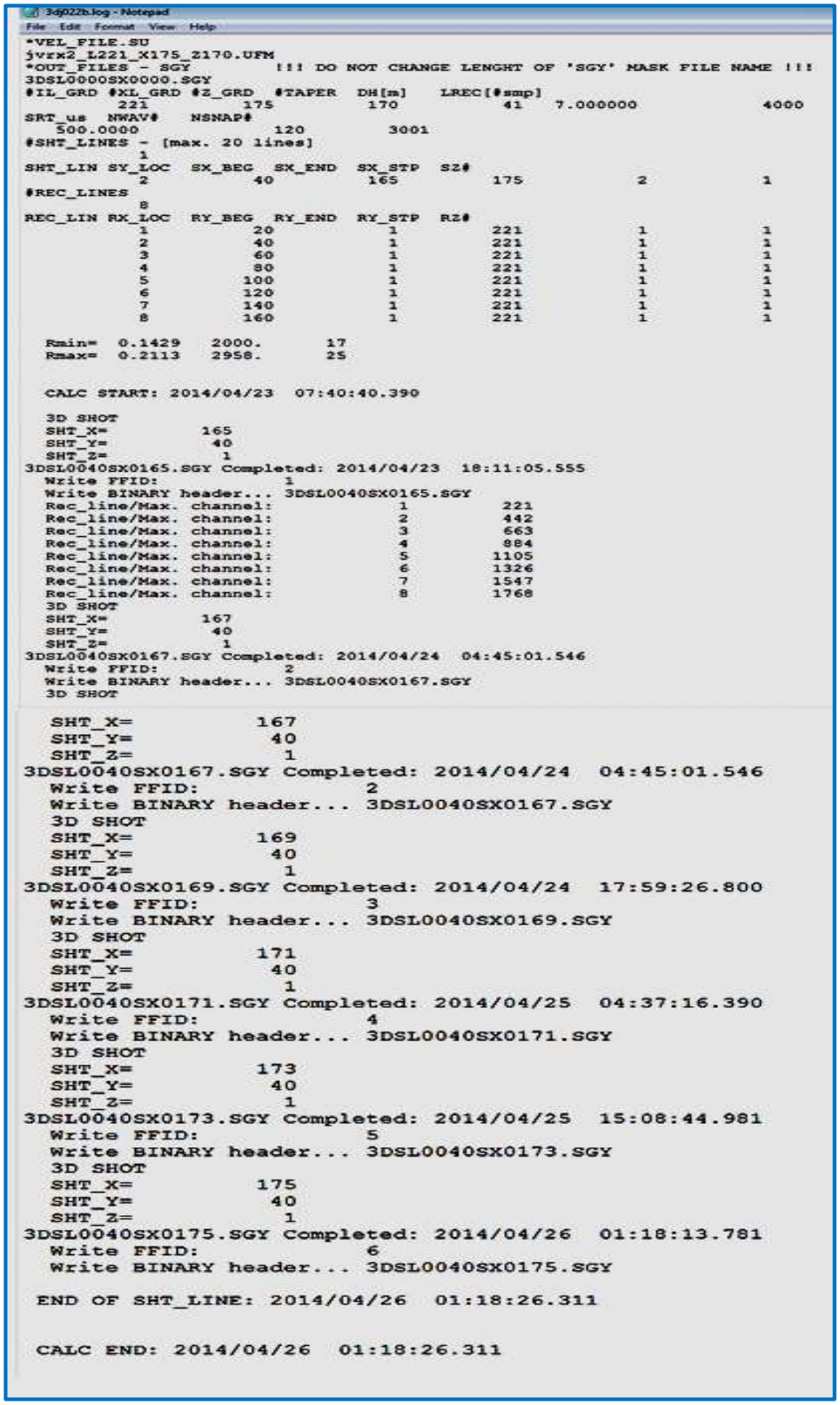

```
3dj022b.log - Notepad
File  Edit  Format  View  Help
*VEL_FILE.SU
jvrx2_L221_X175_Z170.UFM
*OUT_FILES - SGY          !!! DO NOT CHANGE LENGHT OF 'SGY' MASK FILE NAME !!!
3DSL0000SX0000.SGY
#IL_GRD #XL_GRD #Z_GRD  #TAPER  DH[m]    LREC[#smp]
          221          175          170           41    7.000000             4000
SRT_us   NWAV#    NSNAP#
   500.0000             120          3001
#SHT_LINES - [max. 20 lines]
           1
SHT_LIN SX_LOC  SX_BEG  SX_END  SX_STP  SZ#
           2           40          165          175            2            1
#REC_LINES
           8
REC_LIN RX_LOC  RY_BEG  RY_END  RY_STP  RZ#
           1           20            1          221            1            1
           2           40            1          221            1            1
           3           60            1          221            1            1
           4           80            1          221            1            1
           5          100            1          221            1            1
           6          120            1          221            1            1
           7          140            1          221            1            1
           8          160            1          221            1            1

  Rmin=  0.1429   2000.       17
  Rmax=  0.2113   2958.       25


  CALC START: 2014/04/23  07:40:40.390

  3D SHOT
  SHT_X=          165
  SHT_Y=           40
  SHT_Z=            1
3DSL0040SX0165.SGY Completed: 2014/04/23  18:11:05.555
  Write FFID:              1
  Write BINARY header... 3DSL0040SX0165.SGY
  Rec_line/Max. channel:             1          221
  Rec_line/Max. channel:             2          442
  Rec_line/Max. channel:             3          663
  Rec_line/Max. channel:             4          884
  Rec_line/Max. channel:             5         1105
  Rec_line/Max. channel:             6         1326
  Rec_line/Max. channel:             7         1547
  Rec_line/Max. channel:             8         1768
  3D SHOT
  SHT_X=          167
  SHT_Y=           40
  SHT_Z=            1
3DSL0040SX0167.SGY Completed: 2014/04/24  04:45:01.546
  Write FFID:              2
  Write BINARY header... 3DSL0040SX0167.SGY
  3D SHOT
  SHT_X=          167
  SHT_Y=           40
  SHT_Z=            1
3DSL0040SX0167.SGY Completed: 2014/04/24  04:45:01.546
  Write FFID:              2
  Write BINARY header... 3DSL0040SX0167.SGY
  3D SHOT
  SHT_X=          169
  SHT_Y=           40
  SHT_Z=            1
3DSL0040SX0169.SGY Completed: 2014/04/24  17:59:26.800
  Write FFID:              3
  Write BINARY header... 3DSL0040SX0169.SGY
  3D SHOT
  SHT_X=          171
  SHT_Y=           40
  SHT_Z=            1
3DSL0040SX0171.SGY Completed: 2014/04/25  04:37:16.390
  Write FFID:              4
  Write BINARY header... 3DSL0040SX0171.SGY
  3D SHOT
  SHT_X=          173
  SHT_Y=           40
  SHT_Z=            1
3DSL0040SX0173.SGY Completed: 2014/04/25  15:08:44.981
  Write FFID:              5
  Write BINARY header... 3DSL0040SX0173.SGY
  3D SHOT
  SHT_X=          175
  SHT_Y=           40
  SHT_Z=            1
3DSL0040SX0175.SGY Completed: 2014/04/26  01:18:13.781
  Write FFID:              6
  Write BINARY header... 3DSL0040SX0175.SGY

 END OF SHT_LINE: 2014/04/26  01:18:26.311


 CALC END: 2014/04/26  01:18:26.311
```

File 2: Parameter file for shot definition and execution - 3dj022x.prm

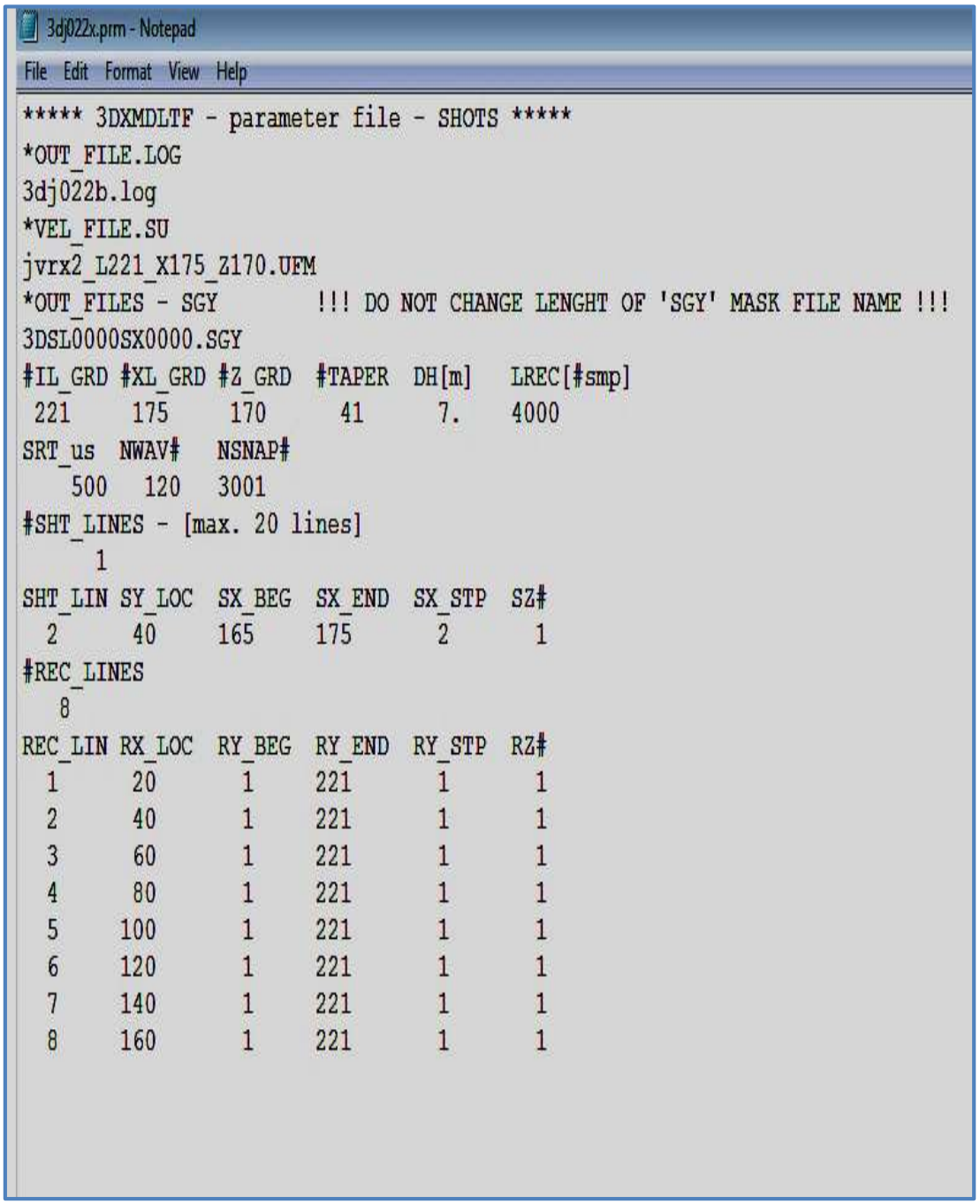

3dj022x.prm - Notepad

File Edit Format View Help

```
***** 3DXMDLTF - parameter file - SHOTS *****
*OUT_FILE.LOG
3dj022b.log
*VEL_FILE.SU
jvrx2_L221_X175_Z170.UFM
*OUT_FILES - SGY        !!! DO NOT CHANGE LENGHT OF 'SGY' MASK FILE NAME !!!
3DSL0000SX0000.SGY
#IL_GRD #XL_GRD #Z_GRD  #TAPER  DH[m]   LREC[#smp]
 221     175     170      41      7.    4000
SRT_us  NWAV#   NSNAP#
    500   120   3001
#SHT_LINES - [max. 20 lines]
      1
SHT_LIN SY_LOC  SX_BEG  SX_END  SX_STP  SZ#
  2      40     165     175       2       1
#REC_LINES
   8
REC_LIN RX_LOC  RY_BEG  RY_END  RY_STP  RZ#
  1      20       1     221       1       1
  2      40       1     221       1       1
  3      60       1     221       1       1
  4      80       1     221       1       1
  5     100       1     221       1       1
  6     120       1     221       1       1
  7     140       1     221       1       1
  8     160       1     221       1       1
```

File 3: Log file example - 3dj092b.log

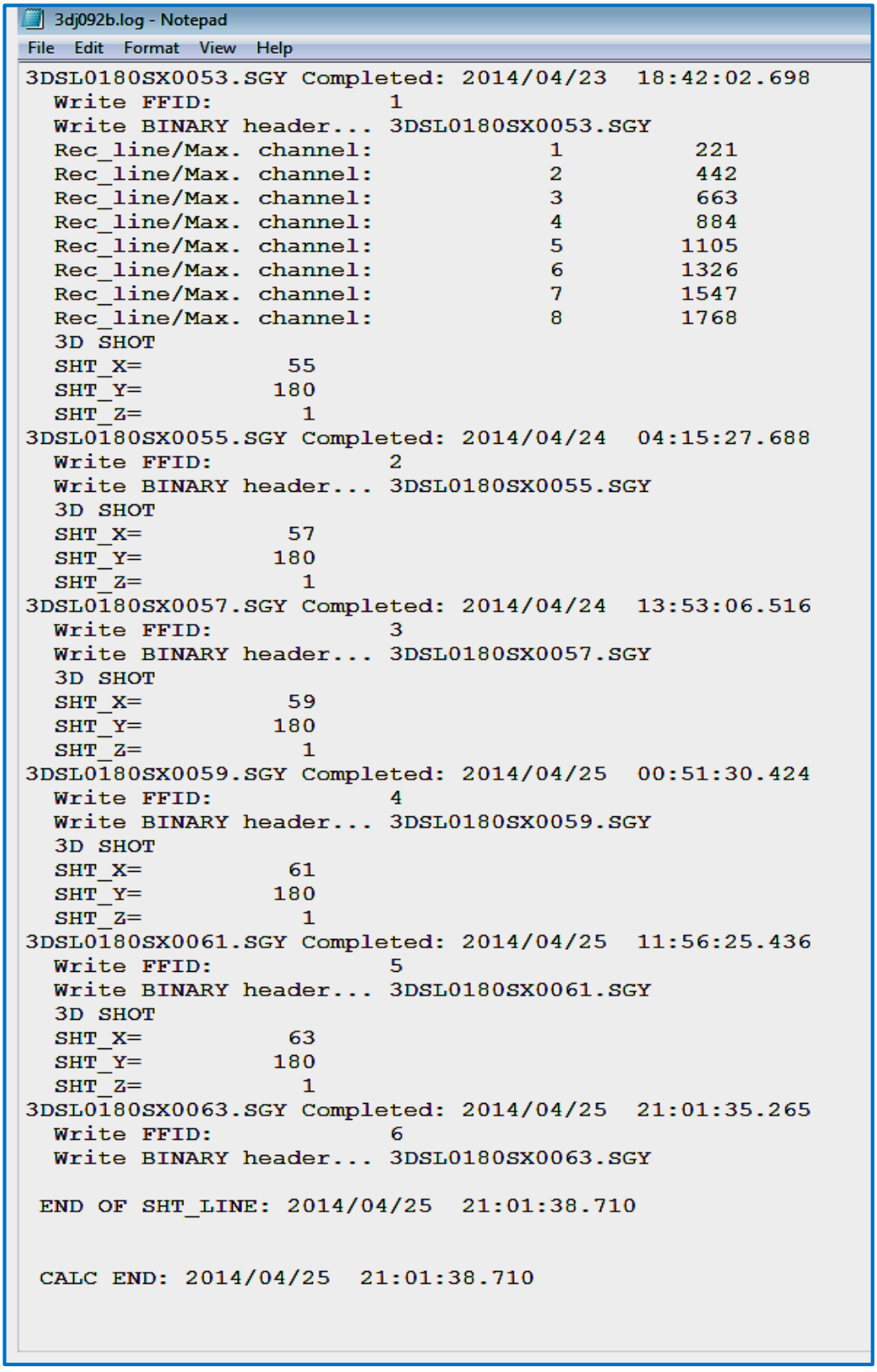

3dj092b.log - Notepad

File Edit Format View Help

```
3DSL0180SX0053.SGY Completed: 2014/04/23  18:42:02.698
  Write FFID:              1
  Write BINARY header... 3DSL0180SX0053.SGY
  Rec_line/Max. channel:              1          221
  Rec_line/Max. channel:              2          442
  Rec_line/Max. channel:              3          663
  Rec_line/Max. channel:              4          884
  Rec_line/Max. channel:              5         1105
  Rec_line/Max. channel:              6         1326
  Rec_line/Max. channel:              7         1547
  Rec_line/Max. channel:              8         1768
  3D SHOT
  SHT_X=           55
  SHT_Y=          180
  SHT_Z=            1
3DSL0180SX0055.SGY Completed: 2014/04/24  04:15:27.688
  Write FFID:              2
  Write BINARY header... 3DSL0180SX0055.SGY
  3D SHOT
  SHT_X=           57
  SHT_Y=          180
  SHT_Z=            1
3DSL0180SX0057.SGY Completed: 2014/04/24  13:53:06.516
  Write FFID:              3
  Write BINARY header... 3DSL0180SX0057.SGY
  3D SHOT
  SHT_X=           59
  SHT_Y=          180
  SHT_Z=            1
3DSL0180SX0059.SGY Completed: 2014/04/25  00:51:30.424
  Write FFID:              4
  Write BINARY header... 3DSL0180SX0059.SGY
  3D SHOT
  SHT_X=           61
  SHT_Y=          180
  SHT_Z=            1
3DSL0180SX0061.SGY Completed: 2014/04/25  11:56:25.436
  Write FFID:              5
  Write BINARY header... 3DSL0180SX0061.SGY
  3D SHOT
  SHT_X=           63
  SHT_Y=          180
  SHT_Z=            1
3DSL0180SX0063.SGY Completed: 2014/04/25  21:01:35.265
  Write FFID:              6
  Write BINARY header... 3DSL0180SX0063.SGY

 END OF SHT_LINE: 2014/04/25  21:01:38.710


 CALC END: 2014/04/25  21:01:38.710
```

File 4: Master parameter File – all shots: 3DJAMAL_master.prm

3DJAMAL_master - Copy.PRM - Notepad

File Edit Format View Help

```
***** 3DXMDLTF - parameter file - SHOTS *****
*OUT_FILE.LOG
3DJAMAL.LOG
*VEL_FILE.SU
jvrx2_L221_X175_Z170.UFM
*OUT_FILES - SGY        !!! DO NOT CHANGE LENGHT OF 'SGY' MASK FILE NAME !!!
3DSL0000SX0000.SGY
#IL_GRD #XL_GRD #Z_GRD  #TAPER  DH[m]   LREC[#smp]
221     175     170     41      7.      4000
SRT_us  NWAV#   NSNAP#
500     120     3001
#SHT_LINES - [max. 20 lines]
10
SHT_LIN SY_LOC  SX_BEG  SX_END  SX_STP  SZ#
1       20      1       175     2       1
2       40      1       175     2       1
3       60      1       175     2       1
4       80      1       175     2       1
5       100     1       175     2       1
6       120     1       175     2       1
7       140     1       175     2       1
8       160     1       175     2       1
9       180     1       175     2       1
10      200     1       175     2       1
#REC_LINES
8
REC_LIN RX_LOC  RY_BEG  RY_END  RY_STP  RZ#
1       20      1       221     1       1
2       40      1       221     1       1
3       60      1       221     1       1
4       80      1       221     1       1
5       100     1       221     1       1
6       120     1       221     1       1
7       140     1       221     1       1
8       160     1       221     1       1
```

File 5: Script file that submits jobs on the cluster node (1 of 4) - Nod00x.sh

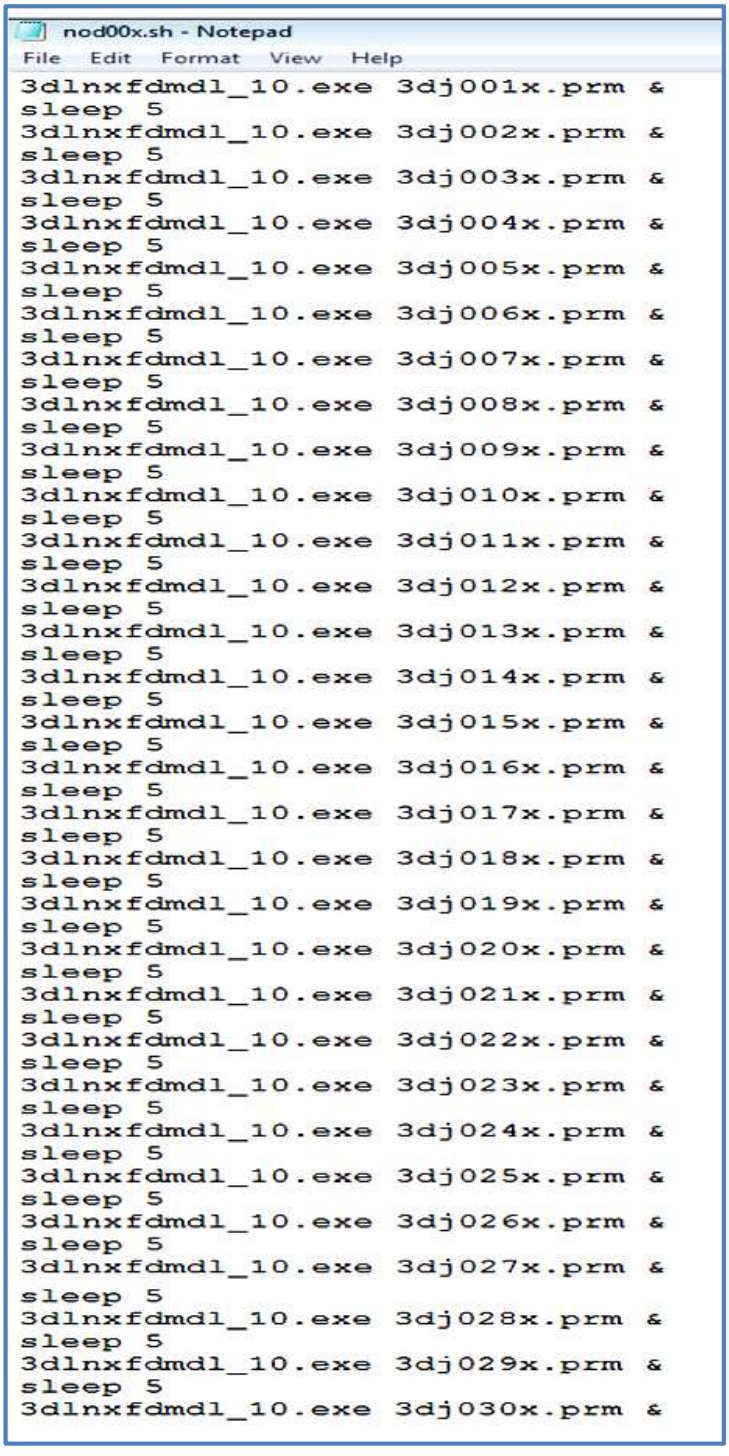
nod00x.sh - Notepad

File Edit Format View Help

```
3dlnxfdmdl_10.exe 3dj001x.prm &
sleep 5
3dlnxfdmdl_10.exe 3dj002x.prm &
sleep 5
3dlnxfdmdl_10.exe 3dj003x.prm &
sleep 5
3dlnxfdmdl_10.exe 3dj004x.prm &
sleep 5
3dlnxfdmdl_10.exe 3dj005x.prm &
sleep 5
3dlnxfdmdl_10.exe 3dj006x.prm &
sleep 5
3dlnxfdmdl_10.exe 3dj007x.prm &
sleep 5
3dlnxfdmdl_10.exe 3dj008x.prm &
sleep 5
3dlnxfdmdl_10.exe 3dj009x.prm &
sleep 5
3dlnxfdmdl_10.exe 3dj010x.prm &
sleep 5
3dlnxfdmdl_10.exe 3dj011x.prm &
sleep 5
3dlnxfdmdl_10.exe 3dj012x.prm &
sleep 5
3dlnxfdmdl_10.exe 3dj013x.prm &
sleep 5
3dlnxfdmdl_10.exe 3dj014x.prm &
sleep 5
3dlnxfdmdl_10.exe 3dj015x.prm &
sleep 5
3dlnxfdmdl_10.exe 3dj016x.prm &
sleep 5
3dlnxfdmdl_10.exe 3dj017x.prm &
sleep 5
3dlnxfdmdl_10.exe 3dj018x.prm &
sleep 5
3dlnxfdmdl_10.exe 3dj019x.prm &
sleep 5
3dlnxfdmdl_10.exe 3dj020x.prm &
sleep 5
3dlnxfdmdl_10.exe 3dj021x.prm &
sleep 5
3dlnxfdmdl_10.exe 3dj022x.prm &
sleep 5
3dlnxfdmdl_10.exe 3dj023x.prm &
sleep 5
3dlnxfdmdl_10.exe 3dj024x.prm &
sleep 5
3dlnxfdmdl_10.exe 3dj025x.prm &
sleep 5
3dlnxfdmdl_10.exe 3dj026x.prm &
sleep 5
3dlnxfdmdl_10.exe 3dj027x.prm &
sleep 5
3dlnxfdmdl_10.exe 3dj028x.prm &
sleep 5
3dlnxfdmdl_10.exe 3dj029x.prm &
sleep 5
3dlnxfdmdl_10.exe 3dj030x.prm &
```

File 6: How is Linux/GNU – FORTRAN connection executed?

Linux is an operating system: a series of programs that allows to interact with PC - computer and run other programs. The **GNU** operating system is a free software system, upward-compatible with UNIX. (It is a recursive acronym meaning "GNU's is not Unix)

This operating system consists of various fundamental programs which is needed by the PC computer so that can communicate and receive instructions from users; read and write data to hard disks, tapes, and printers; control on the use of memory; and run other software. The most important part of the operating system is the kernel. In a GNU/Linux system, Linux is the kernel component.

Since the made 'master program' for the 3D modelling - acoustic finite difference fourth order in space and second order in time works in the way using GNU – FORTRAN that runs for Linux, which was written and created in a way that it was supplied with the parameter file (Appendix D). This file is characterised by having basic parameters necessary for the program to run (i.e. size of the cube, name of the velocity file in specific format, etc. as well as how many lines of shooting). In addition, it has the definition of the receiver lines and the shot lines by their coordinates, and is defined shot by shot how to shoot, because there are almost 2000 shots. Running this single program with the master parameter file will probably take a very long time, months at least if it will be run on one core only because the code is not parallelised. Hence to enable parallelisation, a new program was made to operate the master parameter file with all receiver lines and shot lines. This program calculates how many shots have to be shot for this 3D modelling and it requests from user to declare how many nodes and how many cores processors per node will be used. It then calculates the data "farming" and produces the number of parameter files that are equal to the number of cores or processors on the cluster system.

Consequently, if there are; for instance 10 lines with 180 shots, and we have 128 cores, this number of shots is divided by the number of cores, and then we end up with a number of shots per core. Hence it could be selected to model 12 shots per core. With such studied case, it is requested creation of 128 parameter files, as much as there

are available cores on the computer of 4 nodes, subsequently all 128 parameter files are grouped into four files (Script files) to run on each of 4 nodes.

Data, sub-routines and main routines need to be managed in terms of their paths and connectivity. Constructed velocity and also the parameter file that contains all the detailed information with user explanations need to be managed in terms of space, size, input-output paths and the naming conventions (See Appendices A, B and E).

The format of the script files is as below:

- Name of the program
- Name of the parameter file (which is 001) then 002 … 003 up to 32.
- Then another script file from 33 to 64
- Another script file from 65 to 96
- And last script file from 97 to 128

Hence 33-128 is reserved for "nested" script files. This provides flexibility in programming.

The format of the Master file is geared towards very effective usage. It contains the name of the log file made by FORTRAN (Appendices A and C), while the actual velocity field is of a binary type. The name given here is: "Jamal_ Velocity _ Resampled _ extracted _ second version", using in this case lines 22, 21; X-line 175; depth 170 south.

The output file has data lines and also contains some warnings for the user for the input of certain critical parameters such as: "Do not change length…"

The nomenclature has certain number concatenated such is: 160 005, which in this example indicates that it is position 160 on a receiver line position with its shot being No. 5; also having a sample rate of 500 microsecond and the length of the wavelength which is 120.

Two "blocks" were available; a block that describes shot lines and a block that describes receiver lines. Each column represents first shot line followed by its position in the grid, for example 20 on the axis. The program execution was in this

way: shots 1 -175 with an increment of 2 are consecutively fired, depth step of 1 m. But, in the master file, it was also required to manage data farming across all nodes and cores.

For that purpose a program was made and added to the main Master program called “Parallelisation”. This program manages selection of all nodes and processors available on the cluster. User selects the total number of cores to be occupied by the program, having in mind the not to disturb other cluster users. Then it calculates the total number of shots (in the used case 880) and subsequently divides it by the number of cores (actually processors). In this studied case 128 processors were used, when 880 is divide by 128 then the result is 11 shots per processor. This is because shooting was carried on every odd, the program will make the calculations and then it will execute one shot line to optimise the use of processor time (see the file contains (Appendices A, B, C).

Step 2: Create and check other parameter files that are executing subsequent lines: for example line 20 … shot 1, Line 20 shot 3, Line 20, shot5, until shot 175. When shot 175 is modelled, the execution jumps to the Line 40, simulates all even shots, and so on that is in my case line 200.

Each script file is executed on each node in a time of no more than three minutes. Therefore, each core can execute one 3D shot in about 5 hours depending on data parameterisation (grid size, sampling period). We have 12 shots per one core; therefore we get 12 x 5= 60 hours, approximately 2.5 days. So this data management and full parallelisation enable us to model about 2000 shots in 3 days. This speed is approaching the computation time of commercial programs.

Appendix B
Glossary and list of definitions

Glossary

1. **Pixel** is the smallest two dimensional units controllable of an image of a picture represented on the screen, each pixel is a sample of an original image; more samples typically provide more accurate representations of the original. Pixels are generally arranged in rows and columns; a given combination among the pixels of various brightness and colour values forms an image.

2. **Voxel** is the smallest distinguishable box-shaped unit of a three-dimensional space. A particular voxel will be identified by the x, y and z coordinates of one of its eight corners. This term is used in three dimensional modelling.

3. **Vowelisation** is the process of adding depth to an image using a set of cross-sectional images known as a volumetric dataset. These cross-sectional images (or slices) are made up of pixels. The space between any two pixels in one slice is referred to as interpixel distance. The distance between any two slices is referred to as interstice distance. The dataset is processed when slices are stacked in computer memory based on interpixel and interslice distances to accurately reflect the actual sampled volume.

4. **Artefacts** are weed reflections that mask or obscure the genuine reflected signal or waves. They are caused by abrupt transitions between low- and high-density materials, which results in data values that exceed the dynamic range of the processing.

5. **Dispersion** Frequency-dependence of the wave propagation velocity. It causes a significant stretching of the length of the surface-wave record and the rather late arrival of its largest amplitudes from which the surface wave magnitude.

List of Definitions

Aquifer: a geological formation or group of formations able to receive, store and transmit significant quantities of water.

Bore: means a specific type of well accessing groundwater, generally a small diameter well.

Clastic rocks: are composed of fragments of pre-existing minerals and rock, where the term clastic refers to sedimentary rocks as well as to particles in sediment transport.

Confined aquifer: an aquifer, confined between an upper and lower layer of relatively impermeable material, of layers of low permeability.

CSIRO: Commonwealth Scientific and Industrial Research Organisation.

Groundwater: refers to underground water and includes water that percolates from the ground into a well or other works.

Groundwater resource: flow the movement of groundwater through an aquifer.

IWSS : Integrated Water Supply Scheme; is the system that delivers 279 billion litres of water each year to over 1.5 million people in Perth, , the Goldfields and Agricultural region and some parts of the South West; 31% surface water (mainly from dams, 46% groundwater, 23% desalinated seawater.

Recharge: the process of renewing underground water by infiltration of rainfall.

Sedimentary basin: is an area containing a thick and laterally extensive sequence of sedimentary rocks that have not been severely altered or deformed.

Supply well: a well or bore that draws water to the surface of the ground.

Unconfined aquifer: is an aquifer without an overlying layer of lower permeability which generally gets direct vertical water recharge from the surface.

Unconformity: is a geologic expression that indicates a buried erosional or non-depositional surface separating two rock masses or strata of different ages, indicating that sediment deposition was not continuous.

Water table: is the level to which water rises in a well tapping an unconfined aquifer. It refers to the surface of a body of unconfined groundwater at which the pressure is equal to that of the atmosphere.